USING COMPUTATIONAL MOLECULAR MODELING TO STUDY TRANSPORT PROCESSES OF INTEREST IN SEPARATIONS

BY

XIAOYU WANG

Submitted in partial fulfillment of the
requirements for the degree of
Doctor of Philosophy in Chemical Engineering
in the Graduate College of the
Illinois Institute of Technology

Approved s murad
Advisor

Chicago, Illinois
May 2020

ACKNOWLEDGMENT

Firstly, I would like to express my respect and sincere thanks to my supervisor Prof. Sohail Murad not only for his patience, guidance, support and immense knowledge which help me a lot in my research study, but for other life advice he gave me, especially for a foreigner with no experience in United States. I still remember the summer of 2015 when I met him and asked if he could accept me as his Ph.D. student. I feel so fortunate to work with him during my graduate study.

Besides my advisor, I want to thank Prof. Cynthia Jameson. I enjoyed all the discussions and I do learn a lot about how to become a cautious researcher. I wish I could be as energetic and optimistic as her when I become her age.

I also want to thank my lab members who help me when I first stepped into our research field but lacking of programming and coding skills : Dr. Kevin Hinkle and Dr. Priyanka Oroskar.

Thanks are also due to the (NSF) National Science Foundation (CBET 1545560) for the financial support, otherwise I would not find the interest of doing research and publish so many articles.

Last but not least, I would like to thank my parents who always stand back to support me and encourage me to overcome difficulties in life. Without their warm love, this dissertation would not have been accomplished.

Xiaoyu Wang

May 2020

TABLE OF CONTENTS

LIST OF TABLES

LIST OF FIGURES

LIST OF SYMBOLS

Symbol	Definition
N_A	Avogadro's number
k_B	Boltzmann constant
$\hbar$	Planck constant
T	Temperature
P	Pressure
V	Volume
E_{total}	Total pairwise interaction energy
K_b	Bond energy constant
b_{eq}	Equilibrium length of bond
b	Distance of two bonded atoms
K_θ	Angle energy constant
θ_{eq}	Equilibrium angle of bond
θ	Angle of two adjacent bonds
V_n	Torsion or dihedral energy constant
n	Periodicity of dihedral angle
γ	Phase angle of dihedral
ϕ	Dihedral angles
σ_{ij}	Depth of the potential well for atom i and j from van der Waals interaction
ε_{ij}	Distance where the van der Waals potential is exactly zero
q_i	Atomic charge of atom i

ϵ	Dielectric constant
r_{ij}	Distance between atom i and j
Φ, Ψ	Dihedral angle pairs in glucosidic unit joint of amylose tris(3,5-dimethylphenyl carbamate) polymer

ABSTRACT

Separation processes are widely used in chemical productions. The further development of membrane-based separation processes, compared with thermal separations, can lead to significant energy savings in chemical process industries. However, the main obstacle of experiments is that many separation processes are not well understood at the fundamental molecular level. In this dissertation, we use computational molecular modeling tools, mainly classical molecular dynamics (MD), to clarify molecular forces and provide detail at a molecular level, which can aid in the understanding of transport process and designing materials for a proposed application.

In the first study, we investigated separation of water/alcohol vapor using zeolite membranes. Experimentally, the separation of water/isopropanol (IPA) mixtures shows a dramatic decrease in selectivity due to increase of IPA flux as the feed water concentration decrease when using the sodium A zeolite membrane. We used molecular dynamics simulations to help our experimental collaborators understand these puzzling results. The MD results reveal that the water molecules gather around the defect pores on the zeolite membrane, which stops the IPA from going through the membrane and has a positive effect on separation.

Then, we studied the HPLC used to separate chiral drug mixtures. One popular chiral stationary phase, amylose tris(3,5-dimethylphenyl carbamate) (ADMPC), has been investigated using both experimental and computational methods ; however, the dynamic nature of the interaction between enantiomers and ADMPC, as well as the solvent effects on the ADMPC-enantiomer interaction, are currently absent from the chiral recognition mechanism. We used MD simulations to model the ADMPC in different solvents to elucidate the chiral recognition mechanism from a new dynamic perspective. The ADMPC is found to hold the left-handed helical structure in both methanol and heptane/IPA (90/10) ; however, the ADMPC has a more extended average structure in heptane/IPA. We developed a model where the ADMPC atoms were restricted in the MD simulation. To better understand the molecular dynamic chiral recognition that provides the retention factor and the elution order in HPLC, we examined hydrogen bonding lifetimes, and mapped out ring-ring interactions between the drugs and the ADMPC. We discover several MD metrics related to hydrogen-bonding lifetimes and correlate them with HPLC results. One metric provides a prediction of the correct elution order 90%, and the ratios of these quantities for the enantiomers provide linear correlation (0.85 coefficient) with experimental retention factors.

In the following study, we presented an improved model wherein multiple ADMPC polymer strands are coated on an amorphous silica slab. Using various MD techniques, we successfully coated ADMPCs onto the surface without losing the structural character of the backbone in the solvent. This model provides more opportunities for chiral molecules interacting with ADMPC, resulting in a better agreement compared with experiment when using the overall average metric. The new model also provides the possibility for drug molecules to interact with two polymer strands simultaneously, which is not possible in the previous single-strand model. For a better understanding of why some metrics are better predictors than others, we used charts of the distribution of hydrogen bonding lifetimes to display the information for various donor-acceptor pairs. The results are more consistent than the previous models and resolves the problematic cases of thalidomide and valsartan.

Besides the membrane-based separations, immiscible liquid-liquid equilibrium states were also studied. We successfully predicted results based on MD simulations and showed comparable accuracy with experimental data. This method has applications in liquid-liquid extraction which is widely used in industrial separation process.

CHAPTER 1

INTRODUCTION

1.1 Motivation for This Research

It is estimated that approximately 55% of all energy consumed in chemical processes is spent on separations, of which about 50% is consumed by distillation, 20% by evaporation and 10% by drying, and the remaining 20% by non-thermal separations, including membrane-based separations [1]. Thus, further development of membrane-based separation processes to enable their use in applications currently employing thermal separations can lead to significant energy savings in chemical process industries. However, one of the obstacles in the development of membranes for these otherwise energy-intensive separations is that many membrane-based separation processes are not well understood at the fundamental molecular level, thereby resulting in membrane synthesis becoming an art rather than a science [2] [3] [4] [5]. Computational molecular modeling tools such as molecular dynamics (MD) [6] can play a crucial role in clarifying the molecular level events that result in making a membrane effective for a proposed application.

With recent improvements in computational capacity which has made high performance computing an affordable option, molecular dynamics (MD) modeling described by classical Newtonian equations coupled with semi-empirical force fields can be used to investigate systems ranging from biomolecules, such as proteins and polymers, to small molecules, and provide statistically reliable results with spatial resolution at the sub-Angstrom scale, and temporal resolution at the femtosecond level. In addition, reliable force fields and potential models have been developed for a wide range of systems that closely replicate experiments. The Assisted Model Building with Energy Refinement (AMBER) force field introduced by Weiner et al. [7] [8] and further developed by Cornell et al. [9] is widely used for simulating proteins and studying their structures and interactions with other molecules. Using a computational methodology, Yang et al [10] developed a united-atom force field which has been found to be both realistic in representing a wide range of systems, while still being computationally efficient. General Amber Force Field (GAFF) is an extension of AMBER but optimized by Wang et al [11] and is suitable for simulating small molecules including many common solvents. Jorgensen et al. [12] [13] [14] [15] [16] focused on nonbonded parameterization and developed a family of potential force fields called as Optimized Potential for Liquid Simulations (OPLS), which has been found useful to study pure liquid hydrocarbons, water, amides and their solutions. Chemistry at HARvard Macromolecular Mechanics (CHARMM) is another widely used force field developed by MacKerell et al. [17], which has found applications in proteins, nucleic acids, lipids and carbohydrates. Other force fields, including COMPASS [18] and DREIDING [19] are also widely used in MD simulations. So, computational molecular modeling tools such as molecular dynamics are ideally suited to provide detail at a molecular level that can aid in the understanding of the transport process.

1.2 Objectives of This Research

The recent development of computational ability allows researchers to use the MD simulation to have a better understanding of factors that facilitate membrane-based separations. The MD can also contribute to making separations more efficient. Thus, simulations can be used for screening possible separation schemes, to determine the most promising possibilities. This can cut both the costs and time required to design new membrane-based separation systems.

1.2.1 Have the Ability to Screen for Potential Membranes for Specific Applications and Thus Reduce Costs. Membranes are widely used in different applications to facilitate separations and save energy compared to traditional processes such as distillation and evaporation. Membrane-based separations are also useful in the pharmaceutical industry because many drugs can lose their potency if subjected to higher temperatures usually encountered in distillation. It would be critically important to have the ability to screen possibilities when choosing proper membrane materials for the specific separation. One example of using MD to screen membrane materials is the application to metal-organic frameworks (MOFs). MOFs with different frameworks and metal ions inside the cavity will lead to different properties, such as pore size, surface area, and polarity. Snurr et al. [20] used a combined experimental and modeling approach to select potential candidates used to absorb carbon dioxide. Sholl et al. [21] use the MD method to screen MOFs for the separation of CH_4/CO_2 gas mixture. Similar application of separating ethene/ethane mixture was studied by Caro et al. [22]. Other crystalline materials with regular and repeatable structure can also be studied in this way. One of the most popular type of materials are the zeolite membranes because they have the advantage of low-cost and stability under extreme conditions over organic membranes such as MOFs. Similar to MOFs, zeolite membranes have different frameworks where MD can help to fast-screen possibilities before running experiments. Murad et al. [23] [24] have used MD to study zeolites in pervaporation processes and redox flux batteries. Separations of mixture systems of CO_2/CH_4, CO_2/N_2 and CH_4/N_2 in zeolites were studied by using comparative methodologies. [25] [26]

1.2.2 Provide Insights of Observations From Experiments and Related Phenomena That Are Not Well Understood.

The experimental results sometimes can be mysterious and puzzling because of insufficient understanding of the molecular level behaviors. The MD simulation is normally in the scale of nanometers and has a resolution of picoseconds. Thus, it could provide more details at a molecular level within an extremely short period of time. One example of the wide usage of MD simulations is its applications in bio-systems which consist of lipids, proteins and solvents. Protein molecules play key roles in the processes of transport and docking which usually happens on the lipid membrane surface. With the aid of reliable potential models, researchers can use MD simulations to predict the structure, transport, and free energies. These details can be vitally important and interesting for many aspects of biomolecular function [27]. For example, Karplus et al. [28] used MD to study the open and closed conformational transition of the bacterial chaperonin GroEL. Young et. al [29] studied the coupling and structures between the SH_2 and SH_3 of c-Src and hck. Tai et. al [30] found an unexpected opening and closing of the long channel from the acetylcholinesterase which buried the active site and induced selectivity for different molecules. Protein folding has been of interest to researchers for a long time because the misfolding can potentially lead to disease. Cavalli et al. [31] plotted free energies versus different folding conformations for β-sheet peptide under different temperatures and the structure was found to have a weak dependence on temperature.

1.3 Classical Molecular Dynamics Modeling

1.3.1 Introduction to Molecular Dynamics Simulations. Molecular dynamics is a broad methodology of using Newtonian equations to govern coordinates and motion of particles to trace the time evolution of the physical system. It is a modern implementation of old-fashioned mechanical laws of nature. In order to compute the behavior of a system with explicit particles, a set of initial conditions plus forces of interactions are needed [32]. Constitutive images and trajectories show visualized structural states of molecules, including solvent and protein, DNA, and other macromolecules, which could provide molecular-level understanding. Also, by time averaging over appropriate statistical mechanical expressions, quantities such as pressure, temperature, diffusion, enthalpy and free energy, can be obtained [6]. eqs. (1.1) to (1.4) describe the Newtonian equations used to update velocities and coordinates. By carefully choosing the time step and the length of the simulation, researchers will be able to repeat the procedures as long as needed, or at least, as long as feasible.

$$\vec{F_i}(t) = \vec{\nabla} E_i(\vec{r_i}(t)) \tag{1.1}$$

$$\vec{a_i}(t) = \vec{F_i}(t)/m_i \tag{1.2}$$

$$\vec{v_i}(t + \Delta t) = \vec{v_i}(t) + \vec{a_i}(t) * \Delta t \tag{1.3}$$

$$\vec{r_i}(t + \Delta t) = \vec{r_i}(t) + \vec{v_i}(t) * \Delta t + 1/2 * \vec{a_i}(t) * \Delta t^2 \tag{1.4}$$

1.3.2 Potential Model, Intermolecular Potentials and Intramolecular Potentials.

Although Newton's laws used to solve equations of motion are well-established, the issue of getting a reliable Hamiltonian to describe the system state still remains puzzling and challenging. The potentials developed for particular systems are semi-empirical and usually not transferable from case to case.

$$\begin{aligned} E_{total} = &\sum_{bonds} K_b(b - b_{eq})^2 + \sum_{angles} K_\theta(\theta - \theta_{eq})^2 + \sum_{dihedrals} V_n[1 + cos(n\phi - \gamma)] \\ &+ \sum_{i<j} \left\{ 4\varepsilon_{ij} \left[\left(\frac{r_{ij}}{\sigma_{ij}}\right)^{12} - \left(\frac{r_{ij}}{\sigma_{ij}}\right)^{6} \right] + \frac{q_i q_j}{\epsilon r_{ij}} \right\} \end{aligned} \tag{1.5}$$

Equation eq. (1.5) is an example of the total potential energy equation used in the AMBER [33] force field. Although other force fields will have equations with different formulas, the general idea is essentially similar. The first three terms are intramolecular potentials, including a harmonic bond formed of two joint atoms, a harmonic angle formed of two adjacent bonds and the dihedral angle formed of three adjacent bonds. The last term includes two parts : the one with square bracket describes the non-bonded van der Waals potential. For particular, the AMBER force field uses Lennard-Jones 12-6 (LJ 12-6) model which is also popular in many other force fields ; the last term describes the electrostatic potential and, here, a Coloumbic force model is used. There are other forms describing the nonbonded potential energy (2-body) such as Buckingham, Born-Mayer-Huggins, Morse, Lennard-Jones 9-6, etc., and even more sophisticated styles (3/more-body) such as, Tersoff [34], embedded-atom, etc. When using the Coulombic form of electrostatic force, we assume that there is a point charge in the center of an atom. When using these semi-empirical force fields, one should be careful to determine the partial charges on the atoms because the results have to agree with either experiments such as spectroscopy, dipole moment and electron beam diffraction, or high-level quantum calculations.

Normally, large constraints on bonds make the molecule rigid and does not allow bonds to be broken or rebuilt. Although this method is convenient in protein and macromolecule structure exploration, it disables the application of classical MD into processes (e.g. catalysis or batteries) associated with chemical reactions. The recent development of reactive force field (ReaxFF) [35] by training parameters against QM/MM calculations has broadened MD applications into chemical reactions without actually solving expensive Hartree-Fock or Density Functional Theory (DFT) equations for each system configuration.

1.4 Ab Initio Aided MD, Atomistic MD and Coarse-Grained MD

Ab initio MD (AIMD), atomistic MD and coarse-grained MD share a core concept that the motions are provided by solving Newtonian equations. But they are different in several aspects. Ab initio MD does not need any prescribed forces and potentials to calculate pairwise interactions. By assuming the Born-Oppenheimer approximation, nuclei are fixed to the instantaneous positions of the atoms and the electron clouds move with the nuclei. Time-dependent Schrodinger's equation is solved and energies are obtained as time evolves. Since the nuclear positions are evolving with time, energies are also changing with respect to their positions. With time step chosen carefully and small enough, the energy will be sensitive to the positions at different instances. Solving Schrodinger's equation is usually expensive so the size of the system is smaller than that can be handled with classical atomistic MD.

Coarse-grained MD originating back to the 1970s [36] is a branch and extended area of classical MD. Typically, a particle (more appropriately, an interaction site) in such a system represents a cluster of atoms that can be coupled together without losing important information. This method enables researchers to investigate larger systems and macromolecules, such as DNAs, proteins, and lipids. Since the computational costs are cheaper than atomistic MD, longer simulations at the microsecond time-scale can be achieved. An implicit model of solvent molecules can also be used by replacing the solvent molecule with a continuum, described by an empirical dielectric constant. However, implicit models of the solvent cannot be used to investigate structural changes of macromolecules in a solvent because the implicit model ignores explicit solvent effects on shaping the structure.

1.5 Equilibrium MD (EMD) and Non-equilibrium MD (NEMD)

Equilibrium MD uses statistical thermodynamics theories and relate the observable properties of materials to the variables that define their macroscopic state, which describes equilibrium or local equilibrium states of the system [37]. The development of Green-Kubo formalism related transport properties to equilibrium fluctuations and make it possible to use equilibrium MD to investigate non-equilibrium properties [38] [39]. However, this method has some constraints : the computation of time correlation makes it less accurate when the computational resources are limited ; the flux has to be linearly proportional to the driving force.

NEMD methodology developed by Hoover et al. [40] tried to do simulations that best describe the real physical system. This method has advantages where the relationship between the driving force and the natural response is unknown. Since it requires a tiny portion of the real system, there is a large thermal noise of such a small system and the perturbation has to be larger than the noise. The second method devised by Singer et. al [41] uses spatially periodic transverse perturbation served as the driving force, which no longer requires heat sinks or reservoirs. Other thermal properties will be examined from this continuous transversion. The third method applies additional forces in solving equations of motion, which drives the flux to a target state. This method is similar to the second one where the perturbations can be made explicit and heat reservoirs are not needed. All of these techniques enable the possibility to study non-equilibrium phenomena and properties such as shear flow, thermal conductivity, and thermal diffusion.

1.6 MD Method Used in This Study

In our studies, among these methods, we chose classical and atomistic MD method primarily. We built the systems from non-equilibrium states and ran the simulation until they came to equilibria. We then started sampling the data from the trajectory, which can reflect the systems' characters, properties and behaviors. Under most circumstances, we did not allow the molecules in the simulated systems to break and rebuild bonds, depite the very special case where we simulated the amorphous silica. We used ReaxFF in order to allow the dangling atoms inside the silica slab or on the surface to be capped properly. We shall describe details of every simulation method accordingly in each chapter.

CHAPTER 2

UNDERSTANDING THE SEPARATION PERFORMANCE OF ZEOLITE MEMBRANES

2.1 Introduction

Zeolite membranes have great potential for high separation selectivity because of its well-defined nano-pores and preferential adsorption properties. However, the separation performance is largely influenced by inter-crystalline defects due to the multi-crystalline structure of the membrane. NaA zeolite membranes with Linde Type A (LTA) structure are commonly used for dehydration of solvents because of their strong hydrophilicity and suitable pore size. [42] [43] [44] [45] [46] Even in the presence of nanometer-sized defects, a high pervaporation selectivity up to 10000 has been achieved using the NaA membranes. [47] [48] [49] [50]

Recently, our collaborators observed that the isopropanol (IPA) flux through NaA membranes increase rapidly with decrease in the concentration of water in the water/IPA mixture during vapor permeation (VP). However, such trend is not observed in the case of water/methanol or water/ethanol mixtures. They used capillary condensation to explain the phenomenon, where water molecules are adsorbed in the defects and block the flow of other (larger) molecules through them. [49] [50] Since the IPA molecule (kinetic diameter 0.48 nm) is larger than the LTA zeolite pore diameter (0.42 nm), it could only enter and subsequently diffuse through the defects. [51] However, both methanol (0.38 nm) and ethanol (0.43 nm) molecules can either enter the LTA zeolite cages or diffuse through the defects. Thus, The defect is a reasonable suspect to induce such inefficient separation of alcohol/water mixture. In Fig. 2.1 and Fig. 2.2, our experimental collaborators show the separation performances of two zeolite membranes synthesized by two methods : M2 possessing finer defects than M1. However, experiments are insufficient to provide molecular-level understanding and insights. So, in this study, we used MD simulations to correlate the defect effect with the inefficiency in separation, and to provide molecular-level explanation of the experimental results.

There have been previous reports on adsorption resulting in the change of LTA zeolite unit cell size. It is possible that the adsorbed water would cause either contraction or expansion of the LTA zeolite crystals. In the study reported by Sarakhov et al. [52], the NaA unit cell was able to contract as much as 0.3 vol% at 295 K at low loadings of water and expanded by 0.57 vol% when the cages are ssaturated with water molecules. Noack et al. [53] studied the change of the unit cell size for zeolites as a function of temperature and water content by in situ-heating XRD. They found difficulty in preparation of shape-selective LTA membranes for gas separations due to the extreme expansions/shrinkages of the unit cell when removing water. [53] Sorenson et al. [51] found that at a thermodynamic activity of 0.03 water caused contracting NaA zeolite by 0.22 vol%. At activities above 0.07, water made the NaA crystals expand and they also discovered decreases in the flow of helium, i-butane, and IPA through the NaA membrane.

All these previous studies have shown that zeolite membranes are flexible and the size of the inter-crystalline pores can change due to adsorption of suitable molecules. However, the effect of the adsorption-induced changes in zeolite crystals on membrane separation performance has not been widely studied. Since zeolite membranes are widely used to remove water in solvents in the bulk production, it would be valuable to get a better understanding of this phenomenon and improve these processes. On the other hand, the rapid progress in computer technology has enabled scientists to use molecular dynamics simulations to study chemical engineering processes. In this chapter, we used a flexible zeolite framework model to examine the contraction/expansion of NaA and MOR frameworks.

2.2 Simulation Methods

2.2.1 Potential Models. The framework structure for LTA zeolite was generated from the database IZASC (Structure Commission of the International Zeolite Association). [54] We used potential parameters for the zeolite based on our previous studies, which showed good agreement for water adsorbed in the zeolite framework [55]. In our model, [56] the framework atoms are self-tethered to their equilibrium site with a suitable harmonic constant. Thus, the zeolite framework is allowed to be flexible. The potential models for water and isopropanol alcohol (IPA) are from the AMBER force field [9], and have a functional form shown in eq. (1.5).

As previously mentioned, the potential model has both intramolecular and intermolecular contributions. The first three terms represent flexible bond lengths, bond angles and dihedral angles. The fourth term describes the intermolecular contributions using Lennard-Jones 12-6 potentials and classic Coulombic interactions. We used a 14 Å cut off for LJ interactions, while Ewald methodology was used for long-range electrostatic interactions. [57]

Potential parameters are shown in Table 2.2.1 in which the zeolite parameters were taken from our previous study [55] and Vujic et al. [58], which showed good agreement for water and other non-polar gases adsorbed in the zeolite framework. The potential model used for water molecules was the TIP3P model [59] and that for IPA was from united-atom AMBER. [10]

2.2.2 System Set-Up. The schematic diagram of the system simulated is shown in fig. 2.3 and the this kind of set-up is based on our previous studies for similar systems. [24] The central (middle) compartment of the simulation box contains the vapor phase being investigated. Two layers of NaA zeolite membranes separate this section from the two side compartments which are designed to be initially empty to

Table 2.1. Simulation parameters used to study zeolites, from ref [55] [58] [60]

Molecule	Element	σ (Å)	ε(kcal/mole)	$q(e)$
LTA zeolite	Si/Al	4.009	0.1275	0.0
	O	2.890	0.1550	-0.23
	Na^+	1.90	1.598	1.0
MOR zeolite	Si	2.970	0.0635	1.0720
	Al	3.140	0.0477	1.4130
	O	3.011	0.1550	-0.7476
	Na^+	3.230	0.4652	1.0
Water(TIP3P)	O	3.151	0.1521	-0.8340
	H	0.400	0.0460	0.4170
IPA	CH_3	3.667	0.1494	0.0
	CH	3.667	0.0994	0.2271
	O	3.188	0.1020	-0.6546
	H	0.000	0.0000	0.4275

provide the initial driving force to permit the vapor molecules to permeate through the zeolite membranes. Two systems were investigated for comparison. The first system contained only pure IPA as the vapor phase while the second system contained 5 wt% of water along with IPA. The system size was chosen to ensure that no vapor condensation would happen in the central compartment at the temperature of 423 K. A defect was created by removing some framework atoms around a chosen pore to make the defect size roughly 12 Å and simulate the effect of defects on separations.

Since we are concerned with structural behaviors, such as expansion or contraction, three-dimensional periodic condition is not appropriate in our case. So, in this study, we introduced a system with two periodic boundaries in the X and Y direction and left empty spaces (vacuum) on both side of the crystal structure in the Z direction, as shown in fig. 2.4. The empty space at the margins would allow expansion/contraction. The framework atoms were tethered to their perfect crystal sites with a suitable harmonic constant to allow for structural flexibility in the model. We count the number of water molecules inside the crystal region to represent the absorption of water. The contraction/expansion percentage is measured by comparing the distances between two surfaces in the Z direction. All results were generated by running averages of every 500,000 time steps of the last 40 million time steps to ensure that we were approaching equilibrium.

2.2.3 Simulation Details. All simulations were carried out under non-equilibrium conditions using the LAMMPS simulation package. [61] Energy minimization was performed using the Polak-Ribiere conjugate gradient method [62] and the Verlet algorithm [63] was used to carry out the time integration. The system volume was kept constant and a Nose-Hoover thermostat [64] [65] (with a damping constant of 100 fs) was applied to the solvent and membrane atoms throughout the simulation in order to maintain a constant temperature of 423 K. Following minimization, a timestep of 1.0 fs was used for production runs of 5,000,000 steps (5 ns).

2.2.4 More Details on Choosing Zeolite Models and System Set-Up. The choice of zeolite model is important for simulating the permeation process involved in separations. Many models previously validated in Monte Carlo (MC) simulations cannot be directly applied to MD simulations. For example, some earlier models claim no LJ energy term on aluminum atom but only the electrostatic term. [66] [67] Those models could run in an MC program without problems because there is usually a shortest distance cut-off which is able to prohibit any motions towards the nucleus. Such models may lead to crashing in MD programs. Morden MD software packages rely on soft-sphere models (including LJ, Buckingham, Born-Mayer-Huggins potentials, etc. [68] [69]) which make the close-to-core region full of repulsive forces, instead of the shortest distance cut-off in the MC simulation. But, meanwhile, this could create singularities when atoms accidentally run into the region too close to nucleus and eventually result in infinite energy and program crashing.

The partial charges on the zeolite framework atoms will determine the local polarity and, thus the preference for certain molecules, which serves as the driving force in the separation. A systematic way of deriving partial charges should include following steps : running QM/MM or DFT calculations at first ; then fitting the electrostatic potentials into a much simpler but more robust model by placing a partial point charge on each atomic centers. Although different procedures use this general concept, the partial charges may differ a lot from one method to another. First of all, the choice of basis set in QM/MM or DFT makes a difference. For small molecules, localized basis sets which describes 3D atomic orbitals, such as Slate-type orbital and Gaussian-type orbital basis sets (mainly in Gaussian software package [70]) are commonly used. When it comes to periodic and solid-state systems such as zeolites and crystals, plane-wave basis sets are more popular (e.g., in VASP software package [71]). However, localized basis sets can still be used in crystal or periodic systems by using a special trick. The crystal piece input into the QM calculation should be composed of more than one unit cell in each dimension. When taking the QM results, only the central part is considered. By this way, although the edge effect is still not resolved directly as in plane-wave basis sets, such edge effects are indeed minimized. The second factor is how to interpret electronic information provided by QM/MM or DFT calculations. Different fitting methods certainly will lead to different partial charge values, polarities and dipole moments. Density-Derived Electrostatic and Chemical (DDEC) charges for the atoms of zeolite frameworks developed by Sholl's group, [72] [73] reproduced the electrostatic potential for periodic materials. Woo's group presented Repeating Electrostatic Potential Extracted ATomic (REPEAT) [74] method by using the Ewald summation to include the long-range periodic effect for crystalline solids. In our previous studies, we have proved that our selection of partial charges used in MD simulations of separations of molecules, including methane, water and alcohols, showed good agreement with experiments. [55] The partial charges on zeolites were fitted to provide the correct minimum energy points on the potential energy surface, while the parameters of the sodium cation are fitted through the center-of-cage-to-Na and Na-O distances [60]. Thus, in this study, we continue using this model.

Another factor that may affect the separation is the flexibility of zeolite membrane frameworks. For some separations, the permeant has a smaller molecular size than the opening of the channel. So then even a completely rigid model can be used. However, for other separations when the opening size is smaller than the molecule size, a flexible model should be used to allow the framework to breathe. There have been a lot of studies focusing on developing flexible models for zeolites. [68] [75] [76] [77] Those models use traditional bond, angle, and dihedral terms to allow minor structural changes and can provide acceptable accuracy compared with experiments. However, those models are usually not transferrable into different types of zeolite framework, especially those in which some silicon sites have been substituted with other atom types. Using an inappropriate model will lead to the framework structure collapsing. Dubbeldam et. al [78] [79] developed a transferable force field through fitting on inflection points in isotherms. However, such a method limits itself by the requirement of experiment and has to be re-parameterized every time for a new adsorbent. Our previous work has shown an alternative way. We presented a reasonable way of interpreting vibrations in quantum realm by using a harmonic string to tether the atom to their equilibrium positions. [80] This comprehensive study also revealed that different pore shapes and tethering strength could affect the dynamic properties of the permeant. So, by carefully choosing the tethering strength [55], we will be able to maintain the zeolite structure and have the correct diffusion properties by self-tethering the framework atoms.

When packing the gas phase molecules into the simulation box, we chose a higher than normal density at fixed volume and particular temperature (NVT ensemble). We need to ensure that the intermolecular forces are taking effects, and the distance of two molecules is smaller than the cut-off distance we defined in the non-bonded van der Waal and electrostatic terms. This is also necessary to accelerate simulation and make the system come to equilibrium quickly from a non-equilibrium state.

2.3 Results and Discussions

2.3.1 Separation of Binary Mixture Using NaA Zeolite. In Fig. 2.1(a), we show the water flux and the separation factor of LTA-type zeolite membrane M1 as a function of feed water concentration in vaporized fluids of water/methanol, water/ethanol and water/IPA mixtures at 373 K. The water permeation fluxes in all above systems go down with decreasing water concentration, which is readily explained by the decreasing driving force. The ethanol and methanol fluxes are almost stable, and remain below 0.005 and 0.05 kg*m^{-2}*h^{-1}, respectively. The corresponding separation factors for the both solutions remain above 10000 and 200 at feed water compositions 0.5-5 wt% and 0.7-5 wt% respectively. However, the IPA flux increases significantly from 0.2 to 2.5 kg*m^{-2}*h^{-1} as water content decreases from 5 to 0.5 wt%, resulting in low separation performance at low water content as well as a loss of alcohol product. As shown in Fig. 2.1(b), the separation factor for water over IPA drops from 150 to 15 accordingly. The results indicate that the separation performance of NaA zeolite membrane is strongly related to feed compositions. Despite the larger molecular size of IPA, experiments are unable to obtain high separation selectivity (as compared with ethanol solution).

In a separate trial, the separation of water/alcohol mixtures was investigated by using zeolite membrane M2 (which has shown to be of higher quality with respect to defects). The VP separation results at 373 K are shown in Fig. 2.2. In general, the M2 membrane shows better VP separation performance for water/alcohol mixtures compared to M1. These results are consistent with pervaporation separation results, indicating that the M2 zeolite membrane is of a higher quality (fewer large defects). As the water content in feed mixture decreases, IPA flux increases gradually, while ethanol and methanol fluxes are relatively unchanged. However, the change of IPA flux through M2 is less than that through M1.

Then, we used molecular simulations to get a molecular-level understanding of the behavior observed experimentally. Our simulation results, as shown in Fig. 2.5, confirms the experimental observations discussed above. However, we also include a discussion below on how the simulations offer significant insight into why this unusual phenomenon occurred. Simulations were carried out for pure IPA, and 5% and 10% by weight water in the IPA. As can be seen in the figures, the IPA is able to permeate and diffuse through the defects readily in the absence of water. Once water is introduced, the IPA permeation is essentially stopped. Our simulations provide two primary explanations for why the IPA permeation is prevented when water is present in the mixture. First of all, the water molecules are adsorbed in zeolite pores and defects, thus essentially reducing the effective size of the defect openings. With water presenting at the defect sites, to enter the defects, IPA molecules have to pass through a high energy barrier which is introduced by water blockage. In addition, we also observe another interesting phenomenon from the simulations. In the bulk vapor phase, when water is present, the IPA molecules tend to form clusters with one another, which effectively increases their dynamic diameter making it more difficult for them to permeate the zeolite defects. This is clearly shown in Figs. 2.6 and 2.7. In addition, as can be seen from Fig. 2.7(c) and (d), the presence of water results in fewer IPA molecules at the surface of the zeolite, which further hinders the permeation of IPA into the zeolite. Our results also shows that, when water is present, no

IPA permeated the membrane.

2.3.2 Zeolite Unit Cell Size Changes With Water Loading. Results from molecular simulations shown in Fig. 2.8 reveal that at low water loading the zeolite framework tends to contract, but as the water loading increases the framework tends to expand. When water loading is low, water molecules tend to accumulate in the center of the zeolite cavity ; consequently framework site atoms are attracted towards the center because of the strongly polar nature of the water molecules. As the water loading increases, water molecules start occupying areas near the framework atoms, and repulsive forces then tend to push the framework atoms outward which leads to an expansion of the framework. We would like to point out that the changes in both experiments and simulations generally are in agreement. Although the changes in unit cell size are relatively small, the as-caused changes in defect size could be significant.

The results of molecular simulation are demonstrated in Fig.2.9, which shows that MOR zeolite framework is relative rigid at low water loadings, but with increasing amounts of water, the zeolite framework has a tendency to expand. When the amount of water is low, water molecules are inclined to accumulate in the zeolite cavity center before accumulating on the framework sites. This dynamic change is due to the strongly polar nature of the water molecules being attracted towards the center. But in MOR, there are two different cavity sites that can accommodate water molecules. They can also accumulate in the smaller cavities and the two effects essentially cancel out with some oscillatory behavior observed. This is somewhat different than the trends in our previous work of LTA zeolite frameworks which does not have the smaller cavities that are present in MOR. [81] With increasing of amount of water loading, water molecules start to occupy areas near the framework atoms nearby areas, and repulsive forces then tend to push the framework atoms outward, leading to the zeolite framework expansion. This expansion is also observed in other simulations [82] and demonstrate the suitability of the potential model and the simulation method.

2.4 Conclusion

In this report, the effect of adsorption-induced changes in zeolite crystal size on the separation performance of NaA zeolite membrane for dehydration of alcohols was investigated using molecular dynamics simulations to provide molecule-level insight to explain some of the experimental observations :

(a) MD shows that defects in the crystal do not attract enough adsorbed water molecules to block the defect pores, which leads to a higher resulting IPA flux and lower separation factors. Unlike methanol or ethanol, isopropanol cannot enter the NaA cages and is thus unable to mitigate the effects of low water loadings. Thus an increase of the isopropanol flux can be observed concomitant with a decrease of feed water concentration.

(b) Molecular simulations show that at low loading of water, NaA crystals contract slightly, while they expand similarly at higher loadings. This behavior is due to the interaction between zeolite framework atoms and water molecules.

(c) Different behaviors have been revealed for MOR zeolite at low water loading. The size oscillates instead, because the effects of two kinds of cavities cancel out with each other.

Our studies have enabled us to provide an improved understanding of changes in the sizes of zeolite crystals effects on NaA and MOR zeolite membrane permeation and separations, which will enable further development in the use of NaA zeolite membranes in industrial separations.

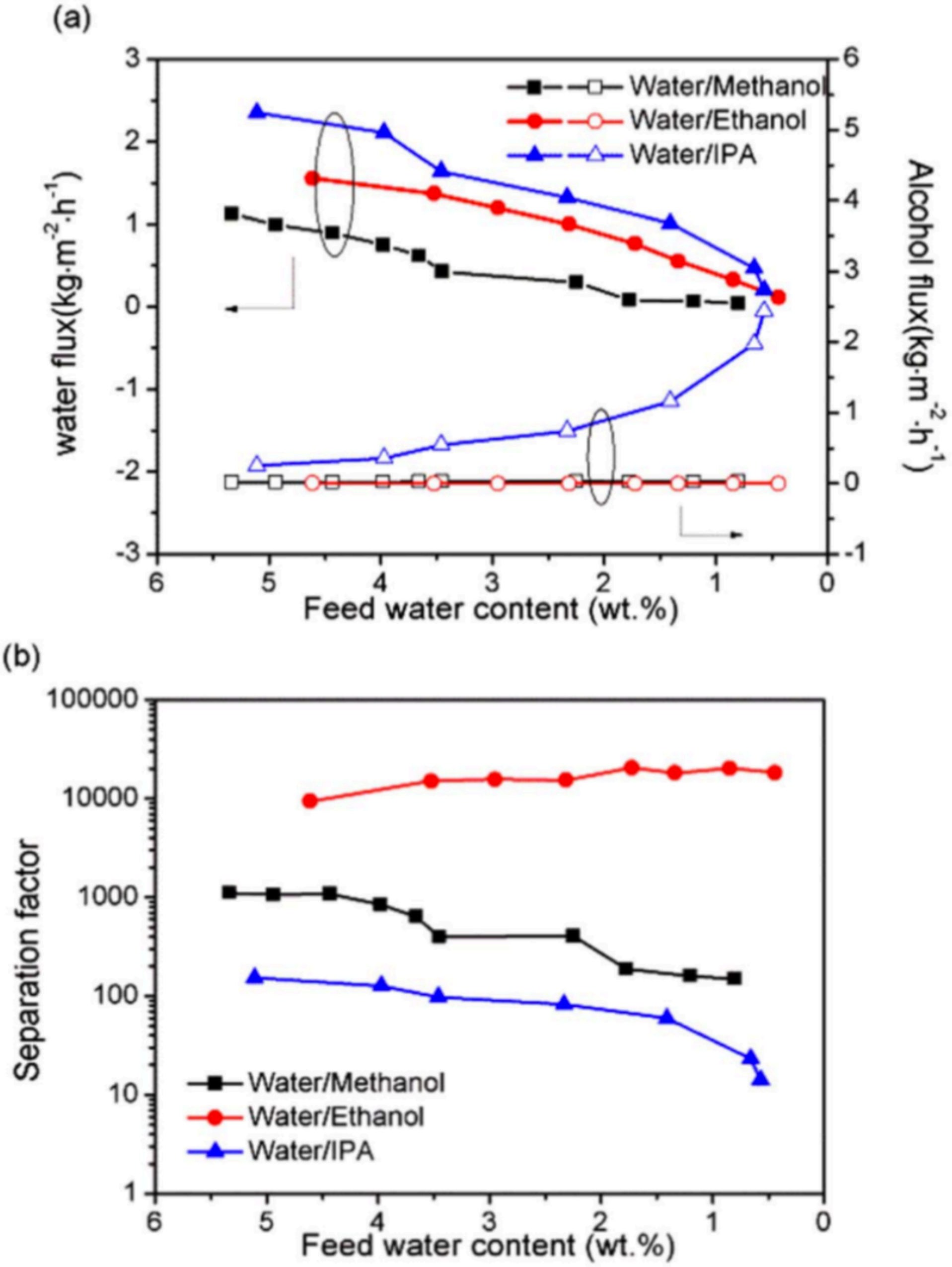

Figure 2.1. VP separation results of M1 for binary water/alcohol(methanol, ethanol and IPA) mixtures at 373K as a function of feed water content : (a) water and alcohol fluxes, (b) separation factor.

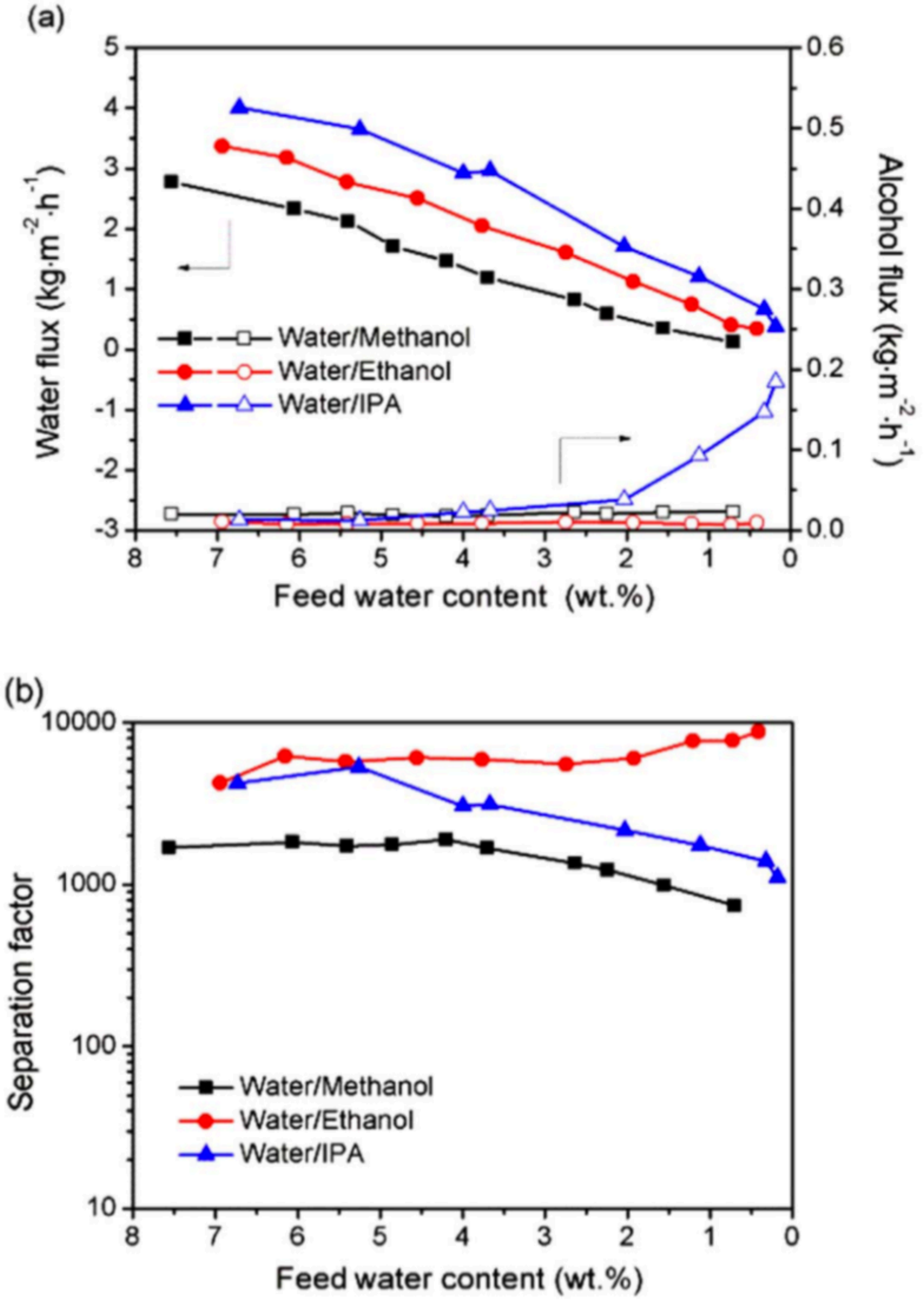

Figure 2.2. VP separation results of M2 for binary water/alcohol(methanol, ethanol and IPA) mixtures at 373K as a function of feed water content : (a) water and alcohol fluxes, (b) separation factor.

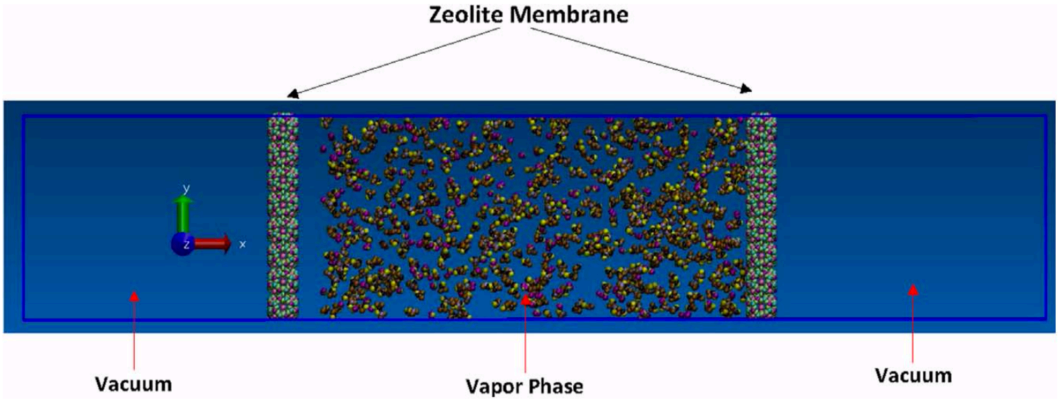

Figure 2.3. Schematic of the simulation system for VP through NaA zeolite membrane.

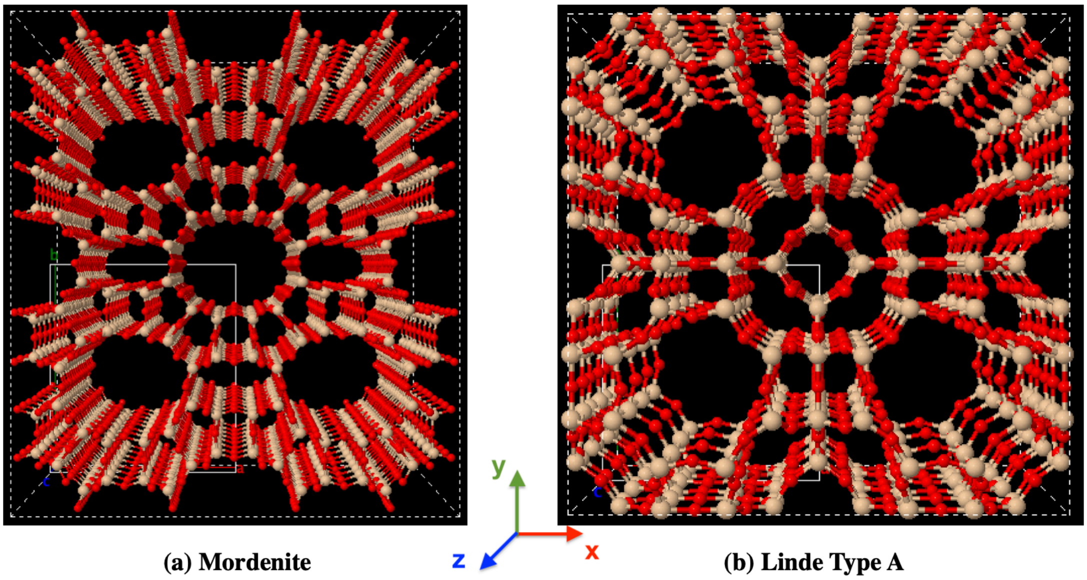

(a) Mordenite

(b) Linde Type A

Figure 2.4. Perspective view of Mordenite and Linde Type A zeolite frameworks (cation ions are not shown in the picture). Yellow balls stand for Si/Al atoms, while red balls stand for O atoms.

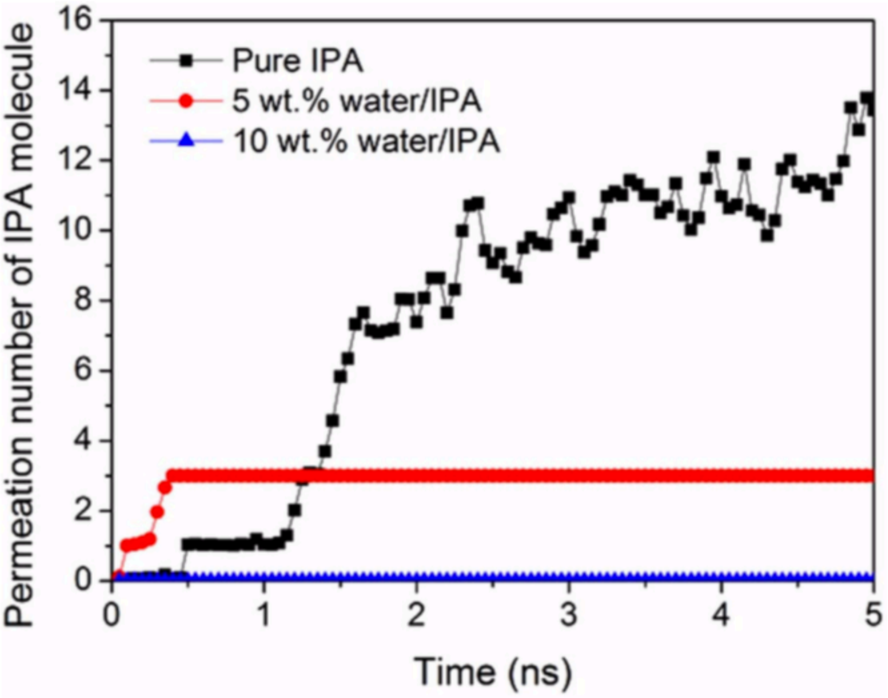

Figure 2.5. Permeation number of IPA molecule as a function of time under different feed water contents.

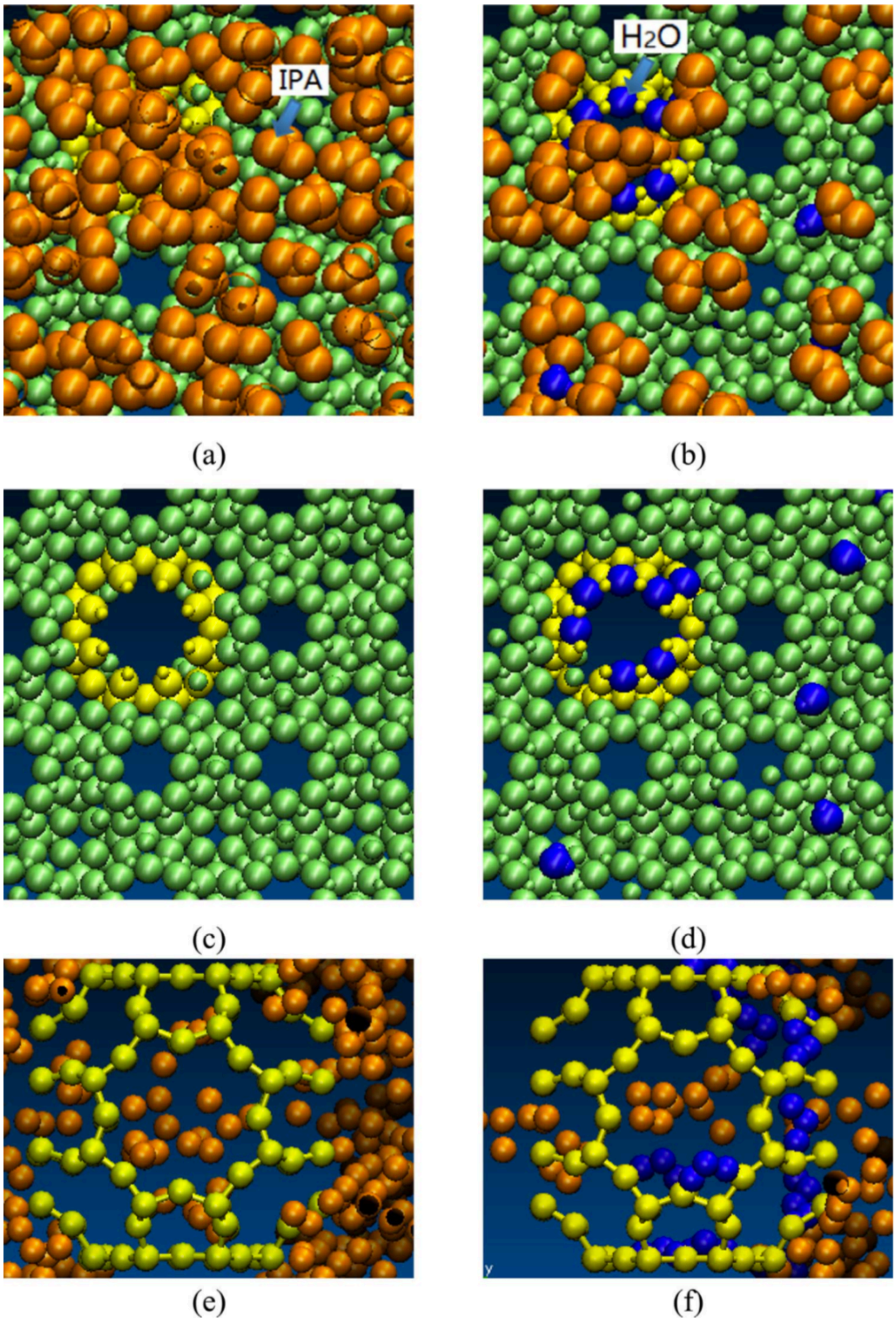

(a) (b)

(c) (d)

(e) (f)

Figure 2.6. Contrasting behavior with pure IPA (left side, a, c, and e) and with 5 wt% water (right side, b, d and f) : axial views of the defect showing (a) pure IPA molecules permeating the defect and (b) water and IPA molecules blocking the defect ; (c) as (a) above but IPA molecules not shown ; (d) as (b) above but IPA molecules not shown ; cross section views showing (e) pure IPA in cavity and (f) both water and IPA molecules in cavity. The spheres represent : green, zeolite framework sites ; yellow, defect sites ; orange, IPA sites ; blue, water. The spheres to ease viewing are not to scale.

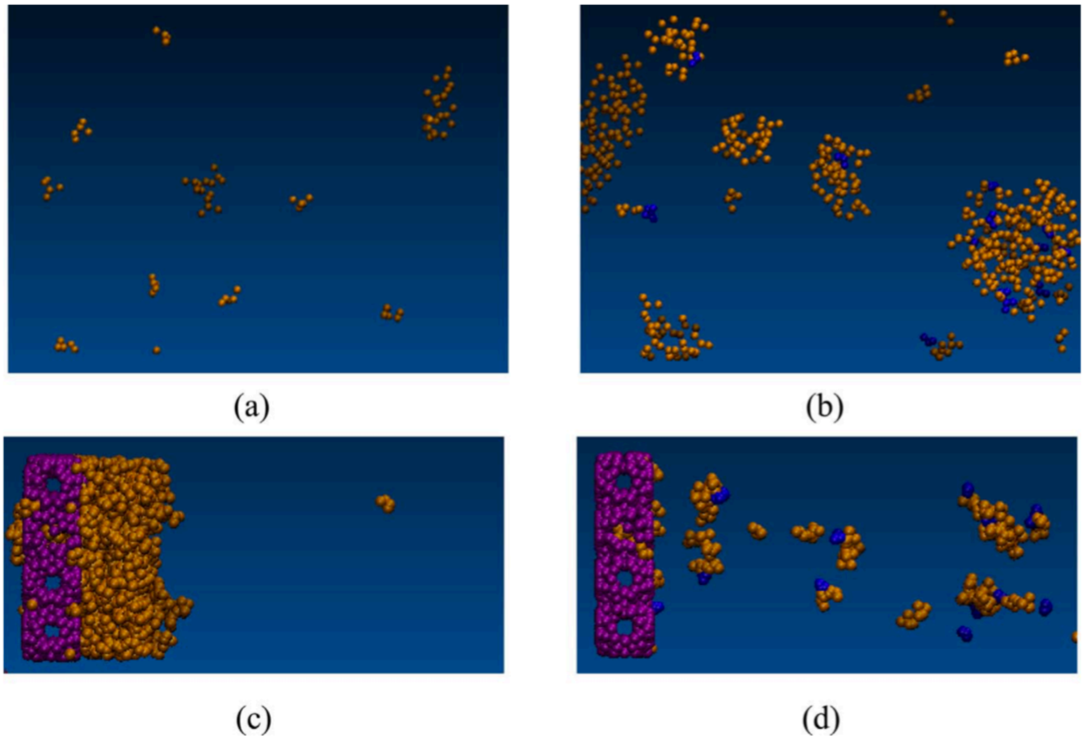

Figure 2.7. Change in phase behavior of vapor phase when water is present : (a) snapshot of the pure IPA vapor phase for a section of the simulation system (away from membrane) ; (b) snapshot with 5 wt% water in vapor phase (away from membrane) ; (c) snapshot of simulation system near the zeolite membrane for pure IPA ; (d) snapshot of simulation system near the zeolite membrane for 5 wt% water in vapor phase. Key : purple zeolite membrane ; orange IPA ; and blue water.

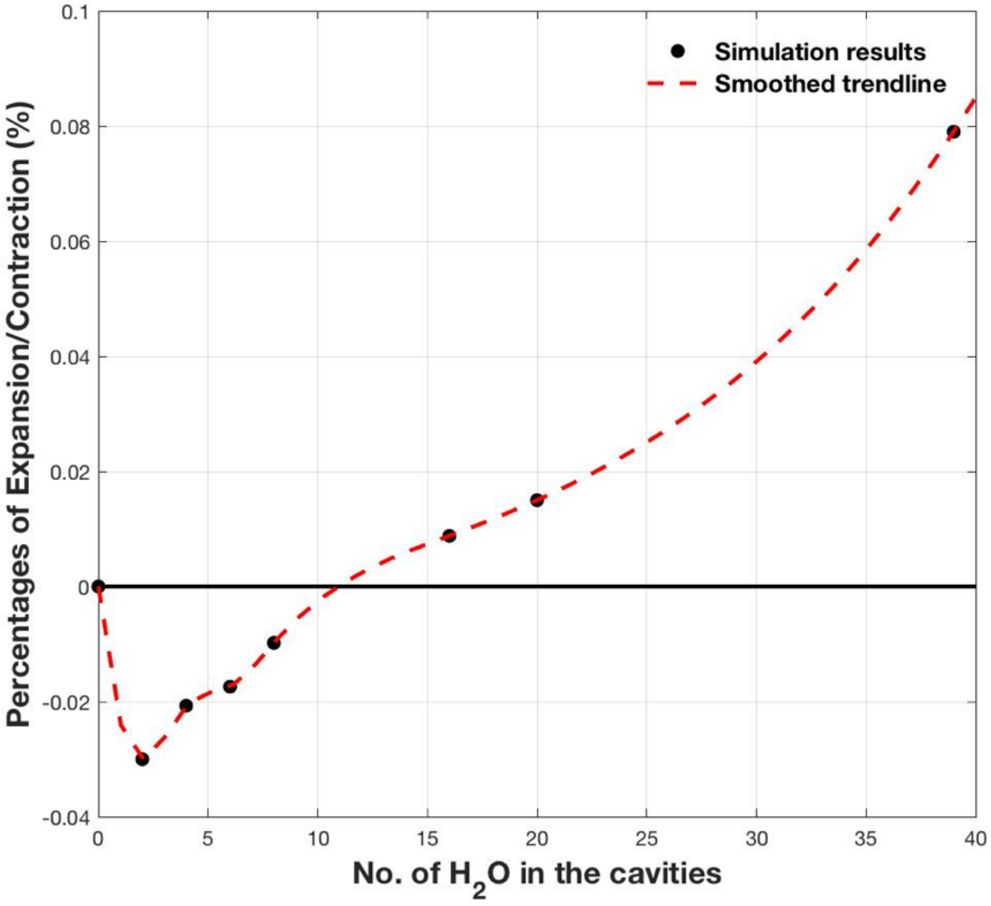

Figure 2.8. Changes of LTA zeolite cavity volume as a function of water loading.

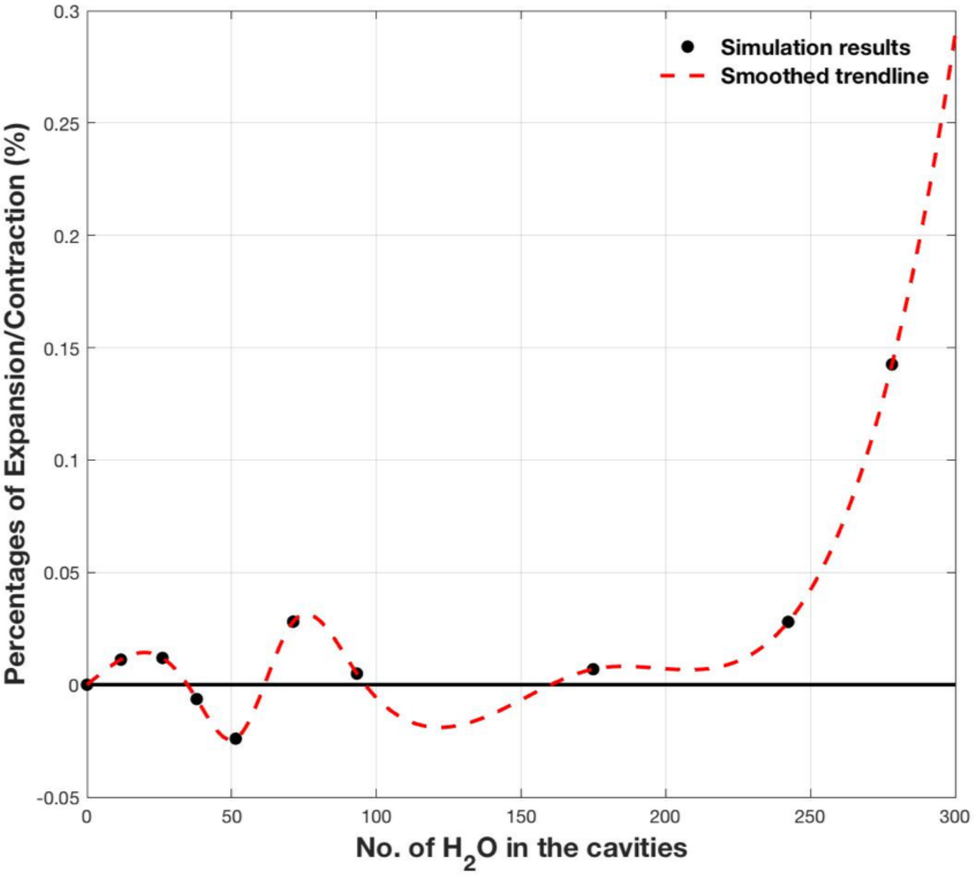

Figure 2.9. Changes of MOR zeolite cavity volume as a function of water loading.

CHAPTER 3

MOLECULAR DYNAMICS SIMULATIONS OF THE CHIRAL RECOGNITION MECHANISM FOR A POLYSACCHARIDE CHIRAL STATIONARY PHASE IN ENANTIOMERIC CHROMATOGRAPHIC SEPARATIONS

3.1 Introduction

3.1.1 Chiral Enantiomers. A molecule with a single chiral center has two enantiomers, often referred to as either S or R enantiomers, which have the same molecular composition but different three-dimensional structures. [83] Enantiomers of drugs could have very different pharmacological activities in living systems since the human body is a highly chiral environment. [84] One enantiomer could have a beneficial therapeutic value ; the other could either be inactive, have a distinctly different activity, or even have an undesirable activity. [85]

3.1.2 Modern Technologies to Separate Chiral Molecules. One of the most effective methods of separating chiral molecules is chromatography, such as gas chromatography (GC) and high performance liquid chromatography (HPLC). Chiral stationary phases (CSPs) are specially made for chromatographic separation of chiral substances. Many different types of CSPs have been synthesized and commercialized, such as Pirkle or brush types, [86] [87] [88] polysaccharide-based, [89] [90] ligand exchange, [91] [92] and so forth. The structure of the most widely used chiral stationary phases, polysaccharide-based CSPs, have been extensively investigated. [93] [94] Yamamoto et al. [95] reported that ADMPC possesses a left-handed 4/3 helical structure in chloroform. Ma et al. [96] used vibrational circular dichroism measurements and also suggested a left-handed helical structure of ADMPC. Besides the backbone helical structure, the structure of the side chain has also been studied ; Kasat et al. [97] reported that it has a planar conformation.

The most prevalent consensus on the interaction mechanism between the CSPs and enantiomers is that at least three sites of interaction must be available to effect chiral discrimination, often referred to as the Easson-Stedman "three-point interaction" model. [98] However, the limitations of the three-point model make it less useful when considering the chiral recognition mechanism of polysaccharide-based CSPs because of the additional hydrogen-bonding sites contributed by the derivatives on the polymer, and that the hydrogen-bonding sites in one derivative are on the same plane. Moreover, static configurational recognition models overlook the fact that chiral recognition is a dynamic process, in which the structure of CSPs and enantiomers change dynamically in the presence of the mobile phase.

The optimization of a chiral chromatography process needs to take many factors into consideration : the choice of CSPs, [99] mobile phases and any modifiers, [100] column temperature, [101] [102] and the pH conditions. [103] The usual empirical approaches to examine the various combinations is tedious and time-consuming. For example, there are many options even for just the polysaccharide-based CSPs, which can be categorized based on their derivatization and whether they are coated or covalently bound to the silica support. The selection of mobile phases is critical, in that the enantiomers should be soluble in the mobile phase, but the chiral phase solid support complex must be insoluble in the mobile phase, else the chiral selector will come off the silica support. The mobile phase should facilitate the interactions between the CSPs and enantiomers, yet be nonreactive with them. A number of suitable mobile phases have been used including aliphatic hydrocarbon-alcohol blends such as heptane and 2-propanol (IPA), polar phases such as alcohols (methanol, ethanol, etc.), alcohol blends, acetonitrile, alcohol-water blends, and water. Sometimes modifiers may need to be added to the mobile phase to reduce secondary interactions, which cause the dispersion (peak broadening) of the analyte. [104] Therefore, to separate a particular pair of enantiomers, there could be, for example, eight CSPs, five mobile phases, and three modifiers, or 120 combinations that must be tested experimentally.

3.1.3 Current Computational and Modeling Research on the Chiral Recognition Mechanism. Computational chemistry and molecular modeling provide a closer look at the detailed structure of the chiral selectors and their interaction with enantiomers, which help to elucidate the chiral recognition mechanism of ADMPC. In combination with NMR experiments, Ye et al. [105] used implicit-solvent molecular dynamics (MD) simulations to study the interaction between a 12-mer of ADMPC with a fixed backbone and the enantiomers. However, their simulation lasted for 2 ns, which might not be long enough to reach equilibrium, and the fixed backbone structure and the placement of the enantiomers in the groove might also have caused some artifacts that could affect the results of the simulation. Furthermore, implicit solvent simulations do not take into account possible local contributions of solvent molecules to changes in configuration of the selector. Similar MD simulations have been reported by Kasat et al. [93], which were also conducted on a system containing ADMPC with fixed backbone structure in the absence of solvent molecules. The composition of the mobile phase can have a crucial effect on chiral recognition because it can affect the structure of the chiral selector and the enantiomer. The effect of the solvent has not been considered in previous theoretical computational studies or in any proposed mechanisms for polysaccharide-based CSPs ; however, there are indications that the mobile phase could play a role in chiral separations. Several MD simulations studies have shown that the absence of explicit solvent in the simulation might induce significant errors in the results of the simulation of the binding of ligands to proteins. [106] Li et al. [107] conducted molecular docking simulations as well as MD simulations of the interactions between an ADMPC with a fixed backbone dihedral angle and metalaxyl/benalaxyl enantiomers, and they concluded that hydrogen bonding is a key factor controlling the chiral separation. Unfortunately, the docking simulations were based on static configurations of ADMPC and enantiomers, thus missing the dynamic nature of the chiral recognition process in their studies.

Density functional theory (DFT) calculations have also been employed to elucidate the binding mechanism between ADMPC and enantiomers. Tsui et al. [108] used DFT methods to study the interaction between the enantiomers and a single molecule of methyl N-methyl carbamate. They proposed a recognition mechanism with three-point interactions. However, in reality the ADMPC polymer has a large number of glucose units and three carbamate side chains on each unit, thus having numerous potential hydrogen-bonding sites. The lowest energy configurations they considered may not be consistent with the lowest energy configuration of one enantiomer with the polymer in the presence of solvent molecules.

3.1.4 Motivation for Molecular Dynamics (MD) Simulation as a Method of Describing the Dynamic Chromatographic Process. Since chromatographic separation is a dynamic process, with the interactions between the drug and the chiral stationary phase mediated by the solvent, no single interacting structure, such as could be found by minimizing the energy using quantum calculations, could possibly describe and account for the ratio of residence times in the chromatographic column for the enantiomeric pair.

Molecular dynamics simulations provide a dynamic atomistic representation of the interaction between the solute enantiomers and the chiral selector ; thus, a large variety of distribution information can be examined, and averages can be obtained over MD trajectories hundreds of ns long. Our aim was to find a set of MD average values that can be correlated with the experimental elution order and with the experimental separation factor. Only atomistic dynamic simulations can provide the dynamic molecular level mechanism for the chiral separation. A further advantage is that, with molecular dynamics simulations we can actually test, at will, whether particular chemical modifications to the CSP will enhance the differences in the chiral interactions of the enantiomers with the CSP. Only when we truly understand the mechanism, can we suggest a priori possible chemical modifications on the racemate or the chiral stationary phase that can improve separation factors for a particular S and R pair. No static model can provide this type of information for further development that can broaden the range of solvents, modifiers, and chiral stationary phases in use.

In this chapter, we applied explicit-solvent atomistic MD simulations to better understand experimentally observed solvent effects on the chiral recognition mechanism. At first, the particular example of flavanone arose from our experimental studies, in which we observed the large difference in separation factors upon changing only the mobile phase. Here, we focus on elucidating the solvent effect on the structural behavior of ADMPC. We demonstrate the left-handed helical structure of ADMPC in MD simulations in different solvents, in agreement with NMR studies, [95] without imposing any restraints on the backbone dihedral angles or the backbone atom positions. We report the different configurations that ADMPC adopts in methanol, acetonitrile and heptane/IPA (90/10), which is further explained by the distribution of solvent molecules along the backbone of ADMPC. We observe differences in configuration in different solvent conditions for the polymer alone in solution. We also find quantitatively significant differences in the interactions between ADMPC and the flavanone enantiomers in methanol or in heptane/IPA. These differences correlate with the experimental elution order of the two enantiomers for both solvent systems, as well as the experimental solvent effect on the separation factor. We present here the chiral recognition mechanism from a new and dynamic atomistic perspective.

Then, several other enantiomer pairs are used to examine the interactions and test the different MD quantities we produce to predict the experimental elution order and separation factor (the ratio of residence times in HPLC). We broaden the field of considered MD averages, to discover which of the dynamic averages from MD simulations provide better correlations with the experimental quantities across the board for the selected solutes of various structural types and can serve as a useful metric. The enantiomers we choose have pharmaceutical relevance and also their absolute orders of elution are known experimentally, so that we may fully test our metrics. We include cases in which the separation factor is relatively large as well as two cases where they were close to 1.0. We would be interested to find commonalities among this broad spectrum, although it is not to be expected that a universal chiral recognition mechanism is in play for the chosen prototypical chiral stationary phase ADMPC with every single one of the selected solutes in the various solvents.

3.2 Methodology

3.2.1 Generating Force Field Parameters for ADMPC and Chiral Enantiomers. Modern classical molecular dynamics models use certain functional forms to interpret quantum effects and electron potentials. Although they are useful to simulate conformational energies and non-bonded interactions for complex molecular systems, such as proteins, lipids, polymers, DNA chains, etc., they suffer from the fact that they do not have a firm physical underpinning as quantum-mechanically-based methods. In this sense, fitting experimental data into empirical parameters for a working force field is important.

Instead of using electron clouds and its distributions, the classical MD method often uses the partial point charge models. Specific force field is usually accompanied with its own systematic procedure to generate parameters such as partial charges, bond strengths, dihedral energy barriers. All those parameters are calibrated through fitting with experiments or quantum calculations and inserted into the functional form of the force field. In order to derive atomic charges of ADMPC and drug molecules, *ab inito* quantum mechanical calculations were performed using GAUSSIAN 09 [70] and DFT-B3LYP/6-31G(d) Method/Basis set combination. The choice of DFT-B3LYP/6-

31G(d) is aligned with the GAFF force field [11] which we used in this study. Apart from that, Becke-3-Lee-Yang-Parr (a.k.a. B3LYP) [109] [110] is a widely used and standard DFT exchange-correlation functional. Compared with Hartree-Fock (HF) or post-HF methods, it provides better dynamic electron correlation and is generally much cheaper than HF methods. [111]

After that, restrained electrostatic potential (RESP) [112] fit was used to find a set of partial point charges. The RESP (Restrained ElectroStatic Potential) program fits the quantum mechanically calculated molecular electrostatic potential (MEP) at molecular surfaces used a multi-parameter set of atom-centered point charges. This method was developed primarily by Bayly. [112] A quantum mechanical program such as Gaussian, [70] Jaguar, [113] GAMESS, [114] or Firefly [115] is used to generate the MEP input for RESP.

The structure of ADMPC shown in Fig. 3.1 was obtained from Okamoto et al. [95], which is already an optimized structure. Methyl groups were used to cap each end of the monomer when generating the partial charges. This is to ensure that the system is neutral because the polymer should have many more repeated monomer units than the 12-mer we used in the study. To facilitate the QM calculations on ADMPC, the partial charges were calculated for only one monomer and later applied to each monomer along the polymer chain. Force field parameters such as bond, angle, dihedral, and nonbonded energy terms were generated based on the AMBER GAFF [11] library.

3.2.2 Equilibrating ADMPC in Different Solvents. One 12-mer ADMPC chain was placed into the solvent box (containing methanol, acetonitrile or heptane/IPA (90/10 v/v)) to generate the average structure using clustering analysis. [116] The average structures in the two solvent systems were later used as the starting points when both ADMPC polymer and chiral enantiomer are in the same simulation system. We used a 70×70×70 $\mathring{A}^3$ box, large enough to ensure that the 12-mer ADMPC does not interact with its periodic mirror image. These types of simulations were performed : one contained one 12-mer ADMPC chain and 4826 methanol molecules; the second contained one 12-mer ADMPC polymer, 1159 heptane molecules, and 215 IPA molecules; the third contained one 12-mer ADMPC and 4826 acetonitrile molecules, to mimic the exact concentrations of the experimental conditions (based on the density of the solution, the molar mass of the solvent molecules, the composition of the mixture, and the size of the simulation box).

Each simulation was conducted using the AMBER simulation package [33] at 298K for 100 ns to permit the ADMPC polymer to approach equilibrium. First, a solvent minimization was performed for 10000 steps using the steepest descent method with the ADMPC chain restrained with a force of 10.0 kcal/mol. Then the system was gradually heated in 100 ps to reach the target temperature of 298K with the ADMPC polymer restrained via a force of 10.0 kcal/mol. After that, an NPT ensemble MD run was performed for 20 ps with ADMPC still restrained with the same force. Subsequently, another round of minimization for 10000 steps with a restraint of 5.0 kcal/mol on the ADMPC polymer was conducted, which is followed by another 20 ps NPT ensemble MD run with ADMPC restrained. Then, the system was further minimized without any restraint for another 10000 steps, followed by a reheating to the target temperature (298K) in 40 ps. Eventually, a production NPT ensemble MD run was conducted for 100 ns. The temperature of the system was maintained by the Berendsen thermostat. [117] Long-range electrostatic interactions were calculated by Partial mesh Ewald (PME) summation [57] with a 9Å cutoff radius. A 1×10^{-5} tolerance for the Ewald convergence was used to calculate the nonbonded interactions. Bonds involving hydrogen atoms were constrained via the SHAKE algorithm. [118] Each simulation was carried out for at least 100 ns. Statistical analysis is based on the last 40-60 ns of the trajectories using Ambertools [33], VMD [119], and in-house scripts.

3.2.3 Clustering Analysis. Clustering analysis in molecular modeling is a method to generate a structure that has the largest population over other possible structure appearing in the MD trajectory. [116] Throughout the MD trajectory, there are many ADMPC structures appearing, but the structure we are going to use initially to sample the interactions between ADMPC and chiral molecules is important. We prefer the most representative structure, which occurs most frequently in the equilibration in solvents. This selection would facilitate reaching the equilibrium in the next step when the enantiomers will be introduced. Generally, the cluster analysis is a task to group the possible structures in such way that all the structures in a subgroup is more similar to each other from the same group than ones from other groups. To be more specific, the cluster analysis can be achieved by various algorithms. The one we used here is called centroid-based clustering. For each subgroup, if we pick two structures and superimpose one on the other, the summation of the Root Mean Square Displacement (RMSD) for selected atomic sites (eg. backbone, side chains, phenyl groups, etc.) has to be smaller than a specified criterion. So, a smaller value of criterion means that the structures in the same subgroup is more like each other, and we may have more subgroups after clustering. In the same subgroup, the centroid structure should have the lowest RMSD if superimposed with any other members. Thus, the centroid structure can serve as the most representative one of its group.

In our study, only backbone atoms were taken into consideration in clustering analysis, because the sole purpose of this analysis is to see if our model is able to maintain the helical structure observed in NMR experiments. [95] The hierarchical agglomerative approach was used in the clustering analysis. The minimum distance between clusters was set as 3Å. A cluster was generated from the analysis based on the distance between frames calculated via best-fit coordinate RMSD using atoms in the backbone of ADMPC. A single representative structure of ADMPC was then generated in methanol and in heptane/IPA (90/10) solvent conditions from the last 20 ns of the simulations. This was used as the starting configuration in the simulations containing both ADMPC and chiral enantiomers in the solvents. A similar procedure was carried out for ADMPC in acetonitrile solvent.

3.2.4 Simulating the Interaction of ADMPC and Chiral Enantiomers. A single ADMPC polymer in one starting configuration, and one molecule of the enantiomer (either R or S) along with solvent molecules are included in the system. The number of drug molecules and solvents was chosen to reproduce the concentration conditions of the experiment. In the HPLC experiment, the concentration of the drug sample is 1 mg/mL ; the volume of injection is 0.2 μL in each experiment ; the column size is 3 mm I.D. × 50 mm long ; the amount of silica gel in the column is around 0.2 g. In addition, the loading level of the ADMPC polymers on the silica gel (i.e., the weight of ADMPC polymer to the weight of the silica gel) must also be controlled. Based on the experimental conditions mentioned above, we calculated the number of drug molecules corresponding to one 12-mer ADMPC chain and found that there is approximately only 1 drug molecule per 12-mer chain in the experiment. The enantiomer, either R or S configuration, is then randomly placed in the $70 \times 70 \times 70$ Å^3 box with the 12-mer ADMPC polymer, followed by the addition of solvent molecules using the PACKMOL program. [120] The number of solvent molecules in the simulation box is the same as that mentioned in the previous section of each system, since the addition of only one small drug molecule would not have a significant effect on the density of the solution. The simulation procedure is the same as mentioned in the previous section. Each simulation was performed for at least 100 ns at 298 K.

First, we developed a fully flexible model (Model 1) where the ADMPC polymer can freely float in the solvent and interact with drug molecules. Then, we carried out an equivalent study in which the drugs interact with a polymer which is restrained with a weak harmonic potential (5 kcal/mol-Å) for each atom of the polymer after equilibration in the solvent, which we call Model 2, to discover the extent to which the free movement of all atoms of the short polymer in solution permit greater sampling by donor-acceptor groups. For the restrained polymer, all atoms are still dynamic, but the cavities for "docking" are very regular and consistent in free volume available to the enantiomers ; and this situation may be more typical of very long polymers laid down on the silica support. The purpose of Model 2 comes from the point that, in real HPLC column, the functional chiral stationary phase (normally polymer strands) is coated on the silica surface and their motions are restrained, but is not like the Model 1 where the polymer is free floating in the solvent.

3.3 Results and discussion

3.3.1 The Left-Handed Helical Backbone of ADMPC Differs in Heptane/IPA compared to in Methanol solvent. Representative structures of ADMPC in methanol and heptane/IPA (90/10) (Fig. 3.3) were generated by using the clustering analysis discussed above. From our MD simulations, we observed that that the most representative structure of the ADMPC strand in heptane/IPA (90/10) is somewhat longer than that in methanol. End-to-end distances used to quantify the length of ADMPC polymer strands are shown in Table 3.1. It is clear to see from the table that the ADMPC in heptane/IPA (90/10) is more extended than in methanol by 4.6Å.

3.3.2 The Ramanchandran Distribution Plots of ADMPC Amylose Backbone Differ in Solvents. Fig. 3.4 (left) shows definitions of Φ (angle formed by $C_{(-1)}$-N-Cα-C) and Ψ (angle formed by N-Cα-C-$N_{(+1)}$) in a typical Ramachandran plot, which represents the secondary structure of a peptide chain. The plot was developed in 1963 by G. N. Ramachandran, et. al. [121] by plotting the Φ values on

Table 3.1. End-to-end distances of the average structures of ADMPC in different solvents.

Solvent systems	Average of last 20 ns (Å)
Methanol	35.25 ± 0.70
Heptane/IPA (90/10) (v/v)	39.88 ± 0.96

the x-axis and the Ψ values on the y-axis. Plotting in this way graphically shows the possibility of a combination of torsion angles. The torsional angles of each residue in a peptide define the geometry of its attachment to its two adjacent residues by positioning its planar peptide bond relative to the two adjacent planar peptide bonds, thereby the torsional angles determine the conformation of the residues and the peptide. By making a Ramachandran plot, biophysicists can determine which torsional angles are permitted and can obtain insight into the structure of peptides. For example, if most points are confined within the region where $\Phi < 0$ and $\Psi < 0$, that means the peptide has a α-helix structure. If most points are confined within the region where $\Phi < 0$ and $\Psi > 0$, that means the peptide has a twisted β-sheet structure.

To further investigate the helical structure of the ADMPC and its backbone, the dihedral angles, Φ (angle formed by H1-C1-O-C2) and Ψ (angle formed by C1-O-C2-H2), were examined. Those two angles are involved in the glycoside bond and they are illustrated in Fig. 3.4 (right). Since a 12-mer ADMPC polymer is investigated in this study, we excluded the glycoside bonds involved in end monomers, namely the one between 1^{st} and 2^{nd} monomer, and the one between 11^{st} and 12^{st} monomer. Those bonds that connect the terminal monomers are relatively more flexible and do not represent the central backbone structure of ADMPC polymer. The Φ and Ψ angles are then used to draw a probability map of the dihedral angles as shown in Fig. 3.5, which is analogous to the Ramachandran plot [121] used in describing the secondary structure of polypeptides in Fig. 3.4 (left). The ADMPC polymer is composed of a amylose backbone which has a helical structure. So, most points should stay inside the region where $\Phi < 0$ and $\Psi < 0$. The colors go from blue to red representing the density of points from low to high in various (Φ, Ψ) regions. For example, if a point is colored by red, that means this point posits in an area with a higher local density of points and the possibility of finding a nearby point is high.

We note from the figures that the ADMPC polymer is dynamic and the (Φ, Ψ) angle distribution sweeps over a wide range at 298 K in the solutions, for both Model 1 (Fig. 3.6) and Model 2 (Fig. 3.5). However, Model 1 and 2 have a similar most probable (Φ, Ψ) angles at $(-60°, -65°)$ for all solvents; thus, the most probable configuration of the ADMPC backbone (shown in red) is very nearly the same in all cases considered here. The less probable dihedral angle distributions (shown in dark blue) are more spread out for Model 1 than for Model 2. This is readily understood because in Model 2 ADMPC atoms are weakly restrained. In these figures, we also find that the dynamic nature of the chiral separation process results partially from the dynamic behavior of the glycoside joints lying in the backbone of ADMPC; this dynamic behavior clearly offers a time-evolving distribution of the molecular electronic surface it presents to the approaching solute. In contrast, in a static picture of molecular recognition, one might choose only the one structure corresponding to the single most probable set of (Φ, Ψ) values, for instance $(-60°, -65°)$, and attempt to dock the enantiomers onto that specific polymer structure. However, this will give rise to a clearly incorrect representation of what goes on in the molecular recognition and chiral separation. All configurations of the ADMPC backbone, not only $(\Phi, \Psi) = (-60°, -65°)$, contribute to the separation process. The differences in the less probable dihedral angles in ADMPC from one solvent to another likely contribute to the differences in magnitudes of separation factors, and sometimes even the differences in elution order of the same racemate in various solvent systems.

It is interesting to note that the hierarchy of solvent hydrogen-bonding strengths methanol, isopropanol, acetonitrile correlates with the changes in the glycosidic dihedral angles ; in the weaker H-bonding solvents, acetonitrile and isopropanol, the glycosidic angles have a wider spread of distribution around the most probable value for both Models 1 and 2. The maps (Fig. 3.5 & 3.6) show that the ADMPC average configuration in each of the different solvent systems provides a different landscape for the chiral solute to interact with, since the carbamate side-chains assume different distributions of orientations about the backbone when the glycosidic angles change their values. This leads us to believe that one may, by studying the structure of ADMPC in many more solvents, find a systematic order in solvents' abilities to promote greater or lesser differentiating/discriminating landscapes for enantiomeric pairs. To some extent, the observed differences in the (Φ, Ψ) maps form a basis for finding modified separation characteristics of a CSP when choosing different solvent systems for a given racemate.

3.3.3 Solvent Molecules Are Involved in the Interaction Between the Chiral Drug and ADMPC. Solvent molecules are found to play a critical role in the interaction between chiral drugs and ADMPC, which is revealed by the correlation between the drug-ADMPC electrostatic interaction energy and the number of solvent molecules within 5Å of the flavanone enantiomers. As can be seen from Fig. 3.7 A,C,E,G, the electrostatic energy between flavanone and ADMPC has various clusters along the time series, indicating multiple times of interactions between flavanone and ADMPC. For the times when flavanone and ADMPC have strongly attractive electrostatic interactions, a decrease in the number of solvent molecules around the drug is also observed. This correlation can be found in the systems with flavanone enantiomers and methanol. A similar correlation can be found between the number of heptane molecules and the electrostatic energy between flavanone and ADMPC in the system with heptane/ IPA (90/10) molecules.

The rationale for choosing to investigate the properties noted above are as follows : Only the electrostatic interaction energy between flavanone and ADMPC is considered because the mechanism of chiral recognition strongly depends on the hydrogen bonding interaction, which is included in the electrostatic interaction. Another reason is that the VdW interaction energy has not been found to have any correlation with the selectivity in this system. We only present the number of heptane molecules versus the time in the system with heptane/IPA (90/10) because the correlations between the number of IPA molecules and the electrostatic energy between the drug and ADMPC are hard to see, given that the number of IPA molecules is much lower than that of the heptane molecules. Note that in the case of the heptane/IPA solvent systems, we have seen that the IPA molecules have a much higher probability of being found close to the ADMPC backbone than the heptane molecules. However, this does not mean that heptane molecules play no role in the interaction between flavanone and ADMPC. This is because flavanone enantiomers will have a much higher probability of being solvated by heptane molecules than IPA molecules before it interacts with the ADMPC. At the same time that flavanone enantiomers interact with ADMPC, a significant drop in the number of heptane molecules, within the solvation distance occurs, but not in the IPA molecules, which also explains why we are not able to see a correlation between the number of IPA molecules close to flavanone enantiomers and the electrostatic ADMPC-flavanone interactions.

3.3.4 The Dynamic Nature of the Molecular Recognition Process. During an MD simulation run, the enantiomer molecule encounter the ADMPC polymer frequently, so they form, break and re-form hydrogen bonds (between donors on the solute with acceptors on the polymer, between acceptors on the solute with donors on the polymer). With the repulsive or attractive interactions between bulky groups such as rings on drug and polymer, the hydrogen-bonds are influenced by the space available to the donor-acceptor sites to get close to each other. Since the R and S enantiomers of the drug have their own spatially distinct shapes relative to the chiral polymer, such interactions between bulky groups will be distinctly different, leading to different hydrogen-bonding opportunities that in turn lead to discrimination between enantiomers. In this work, we examine various characteristics (averages and distributions of hydrogen-bonding lifetimes) of dynamic encounters that can reveal the nature of the differential interactions between the solute enantiomers with the chiral stationary phase in the solvent, in terms of (a) hydrogen-bonding characteristics and (b) ring-ring orientations.

3.3.5 Detailed Analysis of Hydrogen Bonding Between Drug and ADMPC.

The ADMPC has a C=O and a NH group in each carbamate side chain (of which there are three such in every monomer of ADMPC). The drug molecule can have any number of acceptors and donors. A structural schematic of ADMPC and several chiral drugs are shown in Fig. 3.8. A strong/weak hydrogen bond may be formed between a donor on the drug and the C=O of the polymer, or a strong/weak hydrogen bond may be formed between an acceptor on the drug and the NH of the polymer. Also, a donor on the drug can form a hydrogen bond with the –NH group of the ADMPC. Any one or more of these hydrogen bonds may be longer-lived for one enantiomer than the other.

Clearly, hydrogen bonding has a significant impact on the attractive interactions between the drug molecule and the ADMPC polymers ; long-lived hydrogen-bonding interactions between an enantiomer and the chiral stationary phase will defer the drug molecule passing through the column, thus resulting in later elution than its other-handed counterpart. Therefore, we considered various characteristics to describe the dynamic properties of hydrogen-bonding interactions between enantiomers of the drug and the ADMPC. A hydrogen bond is defined in a conventional way in our method : the donor and acceptor distance is less than or equal to 0.35 nm ; the donor-H-acceptor angle deviates from 180° by no more than 30°. Since all solvent and drug molecules are free to move throughout the simulation, a hydrogen bond may stay and remain the above-defined structure for some number of time frames in one MD trajectory that has a length of hundreds of nanoseconds. So we can easily get a hydrogen-bond "lifetime" when a hydrogen bond is on and stays on continuously for a time span. In one entire trajectory, the drug molecule moves in and out so that different hydrogen-bonding pairs of donor and acceptor can break, form and break again. In those cases where more than one donor or acceptor is present on the drug molecule, this happens to each and every donor-acceptor pair between the drug and the polymer. Note that, for a single 12-mer, excluding the end units, there are 27 equivalent (on average) –NH donor groups and 27 C=O acceptors. Thus, there is a multitude of such hydrogen-bonding lifetimes to consider. For each enantiomer/solvent system, in order to obtain statistically valid results, we carried out multiple MD trajectories with varying initial orientations/positions of the drug relative to the polymer. In the final analysis, the results from these trajectories are treated together, equivalent to a trajectory that is a concatenation of all MD runs. Interactions of the drug enantiomers with the end units of the 12-mer were ignored.

We shall state our metrics as follow :

For a particular donor and accepter pair, namely i here, throughout the MD simulation, they form N_i long-lived lifetime fragments and each of them would have a length of consecutive snapshots denoted as :

$$L_{1i},\ L_{2i},\ L_{3i},\ L_{4i},\ \ldots\ , L_{Ni}$$

Then the accumulated number of consecutive frames (F_i) in which a particular donor-acceptor pair i is described as :

$$F_i = \sum_{j=1}^{N} L_{ji} \tag{3.1}$$

The average lifetime ($AvgLT_i$) for a particular donor-acceptor pair i is :

$$AvgLT_i = \frac{F_i}{N_i} \tag{3.2}$$

The largest lifetime ($MaxLT_i$) for a particular donor-acceptor pair i is :

$$MaxLT_i = max(L_{1i},\ L_{2i},\ L_{3i},\ L_{4i},\ ...\ , L_{Ni}) \tag{3.3}$$

For each particular donor-acceptor pair, we defined a weight factor w_i. The factor stands for the fraction of accumulated frames of such pair over the whole accumulated frames of all pairs :

$$w_i = \frac{F_i}{\sum_i F_i} \tag{3.4}$$

Then we defined such 6 metrics we used to describe the hydrogen bonding strength :

maximum of averaged lifetime ($Max\text{-}AvgLT$) for all pairs :

$$Max\text{-}AvgLT = max(AvgLT_1, AvgLT_2, ..., AvgLT_i, ...) \tag{3.5}$$

maximum of largest lifetime ($Max\text{-}MaxLT$) for all pairs :

$$Max\text{-}MaxLT = max(MaxLT_1, MaxLT_2, ..., MaxLT_i, ...) \tag{3.6}$$

maximum of largest accumulated frames ($Max\text{-}F$) for all pairs :

$$Max\text{-}F = max(F_1, F_2, ..., F_i, ...) \tag{3.7}$$

weighted average of averaged lifetime ($Avg\text{-}AvgLT$) throughout all pairs :

$$Avg\text{-}AvgLT = \sum_i w_i * AvgLT_i \tag{3.8}$$

weighted average of largest lifetime ($Avg\text{-}MaxLT$) throughout all pairs :

$$Avg\text{-}MaxLT = \sum_i w_i * MaxLT_i \tag{3.9}$$

weighted average of accumulated frames ($Avg\text{-}F$) throughout all pairs :

$$Avg\text{-}F = \sum_i w_i * F_i \tag{3.10}$$

Thus, for a particular donor and acceptor partner, independent metrics that we can use from the MD simulations are F_i, $MaxLT_i$ and $AvgLT_i$. We consider these quantities for each donor-acceptor pair, including all equivalent interactions with all monomers on the ADMPC excluding the end ones. For most donor-acceptor pairs, the relative order (S >R or vice versa) of the magnitudes of each of these three criteria give results that are consistent with each other, so that any of the three criteria usually leads to the same relative order. However, this is not always the case. For convenience, we have compared lifetimes qualitatively for each donor-acceptor pair and summarize the results in Table 3.2 for Model 1 and Table 3.3 for Model 2.

3.3.6 Prediction of Elution Order and Identification of the Enantiomer That Elutes First. In the following discussions, we will focus on the Model 2 (weakly restrained polymer model). Model 2 depicts a more realistic situation than Model 1 (polymer-free-floating model), and gives better results and accuracy on predicting elution. In reality, in the HPLC column, the polymers are pinned down by attractive forces provided by the silica support surface. Thus, the motions of the ADMPC polymers are restricted. This also provides us the instinct to develop a more realistic model (Model 4) in the following chapter. However, we shall only focus on results from Model 1 and 2, especially Model 2, in the following discussions.

In the case of trans stilbene oxide, only the S enantiomer has long-lived hydrogen bonds with the donor NH of the ADMPC. All three metrics F, MaxLT and

Table 3.2. Dominant hydrogen-bonding interactions for enantiomers with the ADMPC polymer (Model 1).

Drug	R	S	Long lived for	Expt. elutes last
trans-stilbene oxide	O_{drug}-HN_{csp}	O_{drug}-HN_{csp}	R	S
benzoin	$O(H)_{drug}$-HN_{csp} OH_{drug}-$O{=}C_{csp}$ $C{=}O_{drug}$-HN_{csp}	$O(H)_{drug}$-HN_{csp} OH_{drug}-$O{=}C_{csp}$ $C{=}O_{drug}$-HN_{csp}	R R S	S
flavanone(methnaol)	$C{=}O_{drug}$-HN_{csp}	$C{=}O_{drug}$-HN_{csp}	S	S
flavanone(hep/IPA)	$C{=}O_{drug}$-HN_{csp}	$C{=}O_{drug}$-HN_{csp}	S	S slightly favored
tetramisole	$N(amine)_{drug}$-HN_{csp}	$N(amine)_{drug}$-HN_{csp}	mixed	S
binaphthol	OH_{drug}-$O{=}C_{csp}$ $O(H)_{drug}$-HN_{csp}	OH_{drug}-$O{=}C_{csp}$ $O(H)_{drug}$-HN_{csp}	S S	S slightly favored
ambucetamide	$C{=}O_{drug}$-HN_{csp} $NH2_{drug}$-$O{=}C_{csp}$ $N(tert)_{drug}$-HN_{csp}	$C{=}O_{drug}$-HN_{csp} $NH2_{drug}$-$O{=}C_{csp}$	R R mixed	No expt available
etozoline	$OC{=}O_{drug}$-HN_{csp} $>O_{drug}$-HN_{csp} $(5ring){=}O_{drug}$-HN_{csp}	$OC{=}O_{drug}$-HN_{csp} $>O_{drug}$-HN_{csp} $5ring){=}O_{drug}$-HN_{csp}	S S S	No expt available
naringenin[a]	$O2H_{drug}$-$O{=}C_{csp}$ $>O_{drug}$-HN_{csp} $C{=}O_{drug}$-HN_{csp} $O1H_{drug}$-$O{=}C_{csp}$ $O3(H)_{drug}$-$O{=}C_{csp}$ $O2(H)_{drug}$-$O{=}C_{csp}$ $O1(H)_{drug}$-$O{=}C_{csp}$	$O2H_{drug}$-$O{=}C_{csp}$ $>O_{drug}$-HN_{csp} $C{=}O_{drug}$-HN_{csp} $O1H_{drug}$-$O{=}C_{csp}$ $O3(H)_{drug}$-$O{=}C_{csp}$ $O2(H)_{drug}$-$O{=}C_{csp}$ $O1(H)_{drug}$-$O{=}C_{csp}$	S R R mixed mixed R S	R
thalidomide[b]	NH_{drug}-$O{=}C_{csp}$ $C{=}O1_{drug}$-HN_{csp} $C{=}O2_{drug}$-HN_{csp} $C{=}O4_{drug}$-HN_{csp} $C{=}O3_{drug}$-HN_{csp}	NH_{drug}-$O{=}C_{csp}$ $C{=}O1_{drug}$-HN_{csp} $C{=}O2_{drug}$-HN_{csp} $C{=}O4_{drug}$-HN_{csp} $C{=}O3_{drug}$-HN_{csp}	S R S mixed mixed	R
valsartan[c]	$OC{=}O_{drug}$-HN_{csp} OH_{drug}-$O{=}C_{csp}$ $NC{=}O_{drug}$-HN_{csp} $N6_{drug}$-HN_{csp} NH_{drug}-$O{=}C_{csp}$ $N8_{drug}$-HN_{csp} OH_{drug}-HN_{csp} $N5_{drug}$-HN_{csp}	$OC{=}O_{drug}$-HN_{csp} OH_{drug}-$O{=}C_{csp}$ $NC{=}O_{drug}$-HN_{csp} $N6_{drug}$-HN_{csp} NH_{drug}-$O{=}C_{csp}$ $N8_{drug}$-HN_{csp} OH_{drug}-HN_{csp} $N5_{drug}$-HN_{csp}	S R R S mixed mixed mixed R	S

[a] In naringenin O3H is in the 5 position of 5,7-dihydroxy-2-(4-hydroxyphenyl)chroman-4-one, O2H is in the 7 position, and O1H is hydroxyphenyl.

[b] In thalidomide O1 and O4 are the C=O in the dioxopiperidine portion of the molecule, O4 being the one para to the chiral center. O3 and O2 are the C=O in the isoindoline 1,3 dione part of the molecule; O3 is on the less crowded side.

[c] In valsartan, N6 = N8 are on the exposed side of the tetrazol portion of the molecule; N8 is the one bonded to the NH, and N5 is the 3rd unprotonated nitrogen in the tetrazol part.

Table 3.3. Dominant hydrogen-bonding interactions for enantiomers with the ADMPC polymer (Model 2).

Drug	R	S	Long lived for	Expt. elutes last
trans-stilbene oxide	$\mathrm{O_{drug}}$-$\mathrm{HN_{csp}}$	$\mathrm{O_{drug}}$-$\mathrm{HN_{csp}}$	S all metrics	S
benzoin	$\mathrm{C{=}O_{drug}}$-$\mathrm{HN_{csp}}$	$\mathrm{C{=}O_{drug}}$-$\mathrm{HN_{csp}}$	S	S
	$\mathrm{O(H)_{drug}}$-$\mathrm{HN_{csp}}$	$\mathrm{O(H)_{drug}}$-$\mathrm{HN_{csp}}$	R slightly favored	
	$\mathrm{OH_{drug}}$-$\mathrm{O{=}C_{csp}}$	$\mathrm{OH_{drug}}$-$\mathrm{O{=}C_{csp}}$	S	
flavanone(methnaol)	$\mathrm{C{=}O_{drug}}$-$\mathrm{HN_{csp}}$	$\mathrm{C{=}O_{drug}}$-$\mathrm{HN_{csp}}$	S	S
flavanone(hep/IPA)	$\mathrm{C{=}O_{drug}}$-$\mathrm{HN_{csp}}$	$\mathrm{C{=}O_{drug}}$-$\mathrm{HN_{csp}}$	S	S slightly favored
tetramisole	$\mathrm{N(amine)_{drug}}$-$\mathrm{HN_{csp}}$	$\mathrm{N(amine)_{drug}}$-$\mathrm{HN_{csp}}$	S	S
binaphthol	$\mathrm{OH_{drug}}$-$\mathrm{O{=}C_{csp}}$	$\mathrm{OH_{drug}}$-$\mathrm{O{=}C_{csp}}$	S	S slightly favored
	$\mathrm{O(H)_{drug}}$-$\mathrm{HN_{csp}}$	$\mathrm{O(H)_{drug}}$-$\mathrm{HN_{csp}}$	R	
	$\mathrm{OH_{drug}}$-$\mathrm{N_{csp}}$	$\mathrm{OH_{drug}}$-$\mathrm{N_{csp}}$	S	
ambucetamide	$\mathrm{C{=}O_{drug}}$-$\mathrm{HN_{csp}}$		R	No expt available
	$\mathrm{NH2_{drug}}$-$\mathrm{O{=}C_{csp}}$	$\mathrm{NH2_{drug}}$-$\mathrm{O{=}C_{csp}}$	R	
etozoline		$\mathrm{OC{=}O_{drug}}$-$\mathrm{HN_{csp}}$	S	No expt available
		$\mathrm{{>}O_{drug}}$-$\mathrm{HN_{csp}}$	S	
	$\mathrm{(5ring){=}O_{drug}}$-$\mathrm{HN_{csp}}$		R	
naringenin[a]	$\mathrm{O1(H)_{drug}}$-$\mathrm{HN_{csp}}$	$\mathrm{O1(H)_{drug}}$-$\mathrm{HN_{csp}}$	R	R
		$\mathrm{O2H_{drug}}$-$\mathrm{O{=}C_{csp}}$	S	
	$\mathrm{O1H_{drug}}$-$\mathrm{O{=}C_{csp}}$	$\mathrm{O1H_{drug}}$-$\mathrm{O{=}C_{csp}}$	S	
thalidomide[b]		$\mathrm{C{=}O1_{drug}}$-$\mathrm{HN_{csp}}$	S	R
		$\mathrm{NH_{drug}}$-$\mathrm{O{=}C_{csp}}$	S	
	$\mathrm{C{=}O4_{drug}}$-$\mathrm{HN_{csp}}$	$\mathrm{C{=}O4_{drug}}$-$\mathrm{HN_{csp}}$	R	
	$\mathrm{C{=}O3_{drug}}$-$\mathrm{HN_{csp}}$		R	
valsartan[c]	$\mathrm{NH_{drug}}$-$\mathrm{O{=}C_{csp}}$	$\mathrm{NH_{drug}}$-$\mathrm{O{=}C_{csp}}$	S	S
		$\mathrm{N8_{drug}}$-$\mathrm{HN_{csp}}$	S	
		$\mathrm{OH_{drug}}$-$\mathrm{O{=}C_{csp}}$	S	
		$\mathrm{N6_{drug}}$-$\mathrm{HN_{csp}}$	S	
		$\mathrm{NC{=}O_{drug}}$-$\mathrm{HN_{csp}}$	S	

[a] In naringenin O2H is in the 7 position of 5,7-dihydroxy-2-(4-hydroxyphenyl)chroman-4-one, and O1H is hydroxyphenyl.

[b] In thalidomide O1 and O4 are the C=O in the dioxopiperidine portion of the molecule, O4 being the one para to the chiral center. O3 and O2 are the C=O in the isoindoline 1,3 dione part of the molecule; O3 is on the less crowded side.

[c] In valsartan, N6 = N8 are on the exposed side of the tetrazol portion of the molecule; N8 is the one bonded to the NH.

AvgLT for this hydrogen bonding pair are consistent in this prediction. Therefore, the R enantiomer should elute first, in agreement with experiments by Okamoto et al. [122] and also by Castillo-Gonzalez et al. [123]

In the case of benzoin, the acceptor C=O on the benzoin with the donor NH on the ADMPC form the longest-lived hydrogen bonds for both enantiomers, more so for the S enantiomer compared to the R, consistent with two ($MaxLT$ and $AvgLT$) out of the 3 metrics. Second in significance is the O(H) acceptor on the benzoin with the NH donor on the ADMPC, comparable lifetimes for R and S, consistently slightly favoring R. The donor OH on the benzoin with the acceptor C=O on the ADMPC form the third most significant hydrogen bonds for the S enantiomer, dominating over the R in $MaxLT$ and $AvgLT$. It would appear that R should elute first, which is in agreement with our experiment.

In the case of flavanone (2-phenylchroman-4-one), the differences between R and S hydrogen-bonding lifetimes are more pronounced in methanol solvent. The hydrogen bonding of the drug C=O acceptor with the NH of the ADMPC, consistently for all 3 metrics, is more strongly favorable for the S enantiomer than the R, thus R should elute first, in agreement with experiments in methanol by Cirilli et al. [124] The heptane/IPA simulations favoring the S enantiomer, but not as strongly as in methanol, also predict that R should elute first, consistent with the experiments using a similar solvent system, hexane/IPA, by Okamoto et al. [122]

In the case of tetramisole enantiomers, only the tertiary amine nitrogen acceptor forms long-lived hydrogen bonds with the NH donor of the ADMPC for both enantiomers, more so for S than for R, consistently for all three metrics. Thus, MD results indicate that the R enantiomer of tetramisole should elute first, in agreement with our experiment.

In the case of 1,1'-bi-2-naphthol, for the S enantiomer, the dominant hydrogen bonding partners are $\mathrm{OH_{drug}}$–$\mathrm{O{=}C_{csp}}$ followed by $\mathrm{O(H)_{drug}}$–$\mathrm{HN_{csp}}$. For the R enantiomer, $\mathrm{OH_{drug}}$–$\mathrm{N_{csp}}$ followed by $\mathrm{O(H)_{drug}}$–$\mathrm{HN_{csp}}$. With the $\mathrm{OH_{drug}}$–$\mathrm{O{=}C_{csp}}$ dominating the interaction of the S enantiomer with the ADMPC, it appears that S is slightly favored, thus, R should elute first, in agreement with our experiment.

In the case of ambucetamide, the acceptor C=O on the ambucetamide forms the longest-lived hydrogen bonds with the NH of the ADMPC, but only for the R enantiomer, and consistently in all 3 metrics. The S does not form this hydrogen bond for the restrained polymer. The donor NH2 on the ambucetamide with the acceptor C=O on the ADMPC forms the next longest-lived hydrogen bonds for both enantiomers, much more so for the R enantiomer compared to the S, again consistently in all 3 metrics. Thus, it would appear from our simulations that S should elute first. There is, as yet, no experimental absolute assignment of the enantiomer that elutes first. Our ultimate goal is to be predictive in suggesting the elution order. We have therefore carried out some studies where no experimental data on elution order is currently available.

In the case of etozoline the enantiomers have different dominant hydrogen bonds with the ADMPC ; only the S enantiomer forms the $\mathrm{>OC{=}O_{drug}}$–$\mathrm{HN_{csp}}$ and N(5ring)drug–$\mathrm{C{=}O_{drug}}$–$\mathrm{HN_{csp}}$ hydrogen bonds, whereas only the R enantiomer forms the $\mathrm{>O_{drug}}$–$\mathrm{HN_{csp}}$ hydrogen bond. The metrics indicate that the S enantiomer has longer-lived hydrogen bonds, consistently for all 3 metrics ; thus, R should elute first. There is, as yet, no experimental information to confirm this.

The other drug molecules (naringenin, thalidomide, and valsartan) have significantly larger numbers of donor and acceptor sites, so a large number of pairs contribute to the hydrogen bonding lifetimes as the drug makes its way in the vicinity of the ADMPC.

In the case of thalidomide the results for individual donor-acceptor pairs do not have the same strong preference, the $C{=}O1_{drug}$–HN_{csp} and the NH_{drug}–$O{=}C_{csp}$ favor S ; the $C{=}O4_{drug}$–HN_{csp} are comparable for R and S, while the $C{=}O3_{drug}$–HN_{csp} hydrogen bonding is only occurring for R ; thus, the elution order prediction is not unequivocal at this stage. In experiments by Sembongi et al. [125] for thalidomide in methanol, the S enantiomer elutes first, but the experiment was not in pure methanol solvent.

In the case of naringenin, the dominant hydrogen-bonding pair is the hydroxyphenyl O acceptor with the NH of the ADMPC for both R and S enantiomers, with R heavily favored over S for all 3 metrics. Next most important for the S enantiomer is the OH in the 7 position of 5,7-dihydroxy-2-(4-hydroxyphenyl) chroman-4-one as donor to the C=O of the ADMPC. This pair has essentially no contribution for the R enantiomer. The next most important contribution comes from the OH in the hydroxyphenyl as donor to the C=O acceptor in the ADMPC, for both R and S. Thus, R appears more strongly hydrogen bonded overall and S should elute first. This agrees with the experiment by Gaggeri et al. [126]

The S enantiomer of valsartan forms seven types of donor-acceptor pairs with the restrained ADMPC, of which the R forms only a few types and these are short-lived. Thus, it appears that valsartan overwhelmingly favors S (perhaps too much), thus R should elute first, in agreement with our experiment.

Thus, we find, for the weakly restrained ADMPC polymer, that examination of the MD metrics for individual types of donor-acceptor pairs provide fairly consistent predictions of elution order. When all pairs favor the S enantiomer, for example, this would indicate that a prediction that R elutes first is fairly safe to make. And those elution order predictions are found to be fairly consistent with experimental results.

The simulation results are not nearly as consistent for the unrestrained polymer (Model 1), with the three MD metrics giving inconsistent predictions for some donor-acceptor pairs, and with various acceptor-donor pairs providing inconsistent preferences based on the individual metrics, resulting in a lack of predictivity. There is no clearly dominant donor-acceptor pair for most drugs, and for tetramisole, ambucetamide, naringenin, thalidomide, and valsartan, most results are mixed, that is, the 3 metrics provide inconsistent results for the same donor-acceptor pair. Also, there are many more donor-acceptor pairs that participate in the unrestrained polymer, compared to the restrained case, with no dominant contributions. Since not all donor-acceptor pairs favor the same enantiomer, an elution order prediction is not possible at this stage for these racemates interacting with a Model 1 ADMPC. These results indicate that the unrestrained short polymer in solution may be far too flexible in presenting a consistent model for the enantiomers.

3.3.7 Correlation of MD Metrics With Separation Factors.

In the above discussion, we looked at individual donor-acceptor pairs and considered the information that is available from the MD metrics for each pair. Since the drugs have one or more donor sites, and/or one or more acceptor sites, in order to find a quantitative metric that we can use to correlate with experimental separation factors, we need to choose a parameter that combines all donor-acceptor partners in the system. If more than one donor-acceptor pair is available, the maximum values of $MaxLT_i$, $AvgLT_i$ and F_i are 3 possible metrics that could be correlated with the retention times of the enantiomers ; this makes some sense in that the longest-lived hydrogen bond may control the elution order. On the other hand, the properly weighted average of each of these quantities over also can provide 3 possible metrics. These weighted averages, together with the maximum value of $MaxLT_i$, $AvgLT_i$ and F_i among all donor-acceptor partners, thus constitute the six MD metrics in our study.

In the typical HPLC experiment, the separation factor α is defined as the ratio between the retention times, that is,

$$\alpha = \frac{(t_2 - t_0)/t_0}{(t_1 - t_0)/t_0} \tag{3.11}$$

where t_2 is the retention time of the second eluted peak, t_0 is the hold-up time, and t_1 is the retention time of the first eluted peak. We should note that, by this definition, the experimentally αs are always larger than 1. Then the reported α could be the retention time ratio of S/R or R/S, depending on which one is larger than 1. The use of α is experimentally practical and in common use because it does not require the independent knowledge of the identity of the enantiomer that elutes first. In this study, we use a ratio S/R, rather than the value α. Our ratio, S/R of MD metrics, comes out as greater than 1 if R elutes first, and less than 1 if S elutes first.

The ratios S/R for each of the 6 possible MD metrics defined above, are shown in Table 3.4 for each enantiomeric pair studied in this work, using Model 2. These values are to be compared with the experimental ratio of the retention times (S/R) for the enantiomers of the drug in the given solvent system with ADMPC as the chiral selector. For ambucetamide and etozoline, where only the value α has been reported, we display the experimental α value and its reciprocal as possible values for the experimental ratio S/R. Each of these possible metrics has been plotted against the experimental separation factor to discover which provides the best correlation coefficient. The correlation coefficients found are listed as the last row in Table 3.4. In carrying out the least squares fit that correlate the S/R MD metrics with experimental values, we excluded valsartan, where we did obtain the correct elution order but separation metrics ratios are extremely large, for reasons we have not yet determined. Also, for the purpose of finding the correlation coefficients, we assigned the elution order to be that which we found from the MD analysis for the two drugs (ambucetamide and etozoline) for which the absolute configuration of the first eluted

Table 3.4. Comparison of various possible metrics (MD quantities) for Model 2 that may be correlated with experimental ratios of residence times for the enantiomers with ADMPC in the solvent system. S/R ratios, for each metric are given ; each metric is defined in the text. Values less than 1.00 (corresponding to S elutes first) are in red.

Compounds	Solvent	S/R ratio of various quantities						Expt S/R	Expt elutes first	Predict order ?
		Max-F	Max-MaxLT	Max-AvgLT	Avg-F	Avg-MaxLT	Avg-AvgLT			
trans-stilbene oxide	Hep/IPA	1.26	5.56	1.69	1.45	7.68	2.23	2.88 [a], 3.04 [b]	R [b,c]	okay
benzoin	Hep/IPA	0.53	1.35	2.00	0.44	0.94	1.41	1.25 [a]	R [a]	mixed
flavanone	Hep/IPA	5.3	2.3	1.8	2.7	1.1	1.0	1.06 [a]	R [b]	okay
flavanone	Methanol	8.8	4.1	2.7	10.8	3.3	2.1	2.52 [a]	R [d]	okay
tetramisole	Hep/IPA	2.21	1.45	1.44	2.13	1.41	1.40	1.20 [a]	R [a]	okay
binaphthol	Hep/IPA	0.84	1.35	1.19	0.59	1.00	1.05	1.08 [a]	R [a]	okay
ambucetamide	acetonitrile	0.010	0.18	0.38	0.012	0.38	0.51	1.30 or 0.77 [e], 1.44 or 0.69 [f]		maybe okay
etozoline	acetonitrile	1.71	3.78	2.62	1.71	3.79	2.64	1.33 or 0.75 [e], 1.40 or 0.71 [f]		maybe okay
naringenin	Hep/IPA	0.48	0.25	0.81	0.44	0.28	0.57	0.75 [a], 0.68 [g]	S [g]	okay
thalidomide	Methanol	0.56	2.64	2.74	0.48	1.54	2.16	0.47 [e], 0.35 [f], 0.77 [h]	S [h]	mixed, mostly wrong
valsartan	Hep/IPA	4626	101	26.4	5744	79.6	13.6	1.29 [a]	R [a]	ok but poor ratio
Cooreln. Coeff. S/R [i]		0.502	0.863	0.404	0.619	0.876	0.623			

[a] David House, Orochem Technologies, Inc.

[b] α=3.04 for trans stilbene in hexane/isopropanol, with the (1R,2R)-(+) enantiomer eluted as the first peak ; α=1.12 for flavanone in hexane/isopropanol, with the (R)-(+) enantiomer eluted as the first peak ; from [122].

[c] Resolution was R_S = 10.6 for trans stilbene oxide in n-hexane/isopropanol (90 :10, v/v), with the (1R,2R)-(+) enantiomer eluted as the first peak, from [123].

[d] α=2.17 for flavanone in methanol, with the (R)-(+) enantiomer eluted as the first peak, from [124].

[e] Ref [127].

[f] α=1.44 for ambucetamide in acetonitrile, α=1.40 for etozoline in acetonitrile, α=2.89 for thalidomide in methanol, from [128].

[g] α=1.48 for naringenin in n-heptane/isopropanol (90 :10, v/v), with the (S)-enantiomer eluted as the first peak, from [126].

[h] α=1.30 for thalidomide in methanol, with the (S)-(-) enantiomer eluted as the first peak, from [125].

[i] Excluding valsartan in the correlation plot.

enantiomers are still unknown experimentally [128]. As seen in Table 3.3 and 3.4, our MD results provide the same prediction across the board for all metrics for these two drugs ; therefore, we believe that we very likely have the correct MD prediction of elution order in these two cases. The best correlation coefficients for the restrained polymer are for metrics based on the maximum lifetimes ; that is, both the average of the individual maximum lifetimes for each donor-acceptor partner and the overall maximum value. At the present stage of this work, the best correlation provides separation factors with a correlation coefficient of 0.876, although the next best correlation has a very similar correlation coefficient of 0.863 ; both metrics are based on maximum lifetimes of donor-acceptor partners. The elution order is predicted correctly for all but thalidomide. Our thalidomide prediction is not necessarily incorrect since the independent determination of absolute configuration was not 100% methanol as in our simulations, but 70% methanol, 10% acetonitrile, and 20% citrate buffer with a pH of 3.0. [125] We summarize the two best correlations with experiments in Fig. 3.9, data taken from Table 3.4. We note that these metrics capture a high percentage of the elution orders observed in experiments.

As already discovered in considering individual donor-acceptor pairs in Tables 3.2, it would be unsurprising that, in Table 3.5, we find the wrong elution order predicted by the Model 1 (unrestrained polymer model) and poor correlation coefficients. This shows that Model 1 is not an acceptable model for simulating enantiomeric separations using ADMPC coated on a solid support in HPLC chiral separations.

3.3.8 Analyses of the Ring-Ring Interactions Between Drug and ADMPC.

Ring-ring interactions are expected to play an important role in molecular recognition, although the classical MD simulation we use in this study cannot necessarily depict the attractive π-π interactions. The planar bulky rings on the ADMPC side-chian control the space and orientation that can be accessible to the drug. The drug molecule

Table 3.5. Comparison of various possible metrics (MD quantities) for Model 1 that may be correlated with experimental ratios of residence times for the enantiomers with ADMPC in the solvent system. S/R ratios, for each metric are given; each metric is defined in the text. Values less than 1.00 (corresponding to S elutes first) are in red.

Compounds	Solvent	S/R ratio of various quantities						Expt S/R	Expt elutes first	Predict order?
		Max-F	Max-MaxLT	Max-AvgLT	Avg-F	Avg-MaxLT	Avg-AvgLT			
trans-stilbene oxide	Hep/IPA	0.36	0.08	0.33	0.05	0.12	0.04	2.88 [a], 3.04 [b]	R [b,c]	Wrong
benzoin	Hep/IPA	0.99	0.63	0.81	0.40	0.89	0.46	1.25 [a]	R [a]	Wrong
flavanone	Hep/IPA	5.3	2.3	1.8	2.7	1.1	1.0	1.06 [a]	R [b]	okay
flavanone	Methanol	8.8	4.1	2.7	10.8	3.3	2.1	2.52 [a]	R [d]	okay
tetramisole	Hep/IPA	0.94	1.07	0.93	0.95	1.10	0.87	1.20 [a]	R [a]	mixed
binaphthol	Hep/IPA	4.41	1.09	2.18	1.52	2.08	1.52	1.08 [a]	R [a]	okay
ambucetamide	acetonitrile	0.81	0.33	0.75	0.06	0.43	0.06	1.30 or 0.77 [e], 1.44 or 0.69 [f]		maybe okay
etozoline	acetonitrile	28.3	27.0	10.1	90.6	99.5	99.5	1.33 or 0.75 [e], 1.40 or 0.71 [f]		maybe okay
naringenin	Hep/IPA	1.81	1.08	1.28	2.14	1.28	2.45	0.75 [a], 0.68 [g]	S [g]	Wrong
thalidomide	Methanol	1.24	1.30	1.65	1.38	1.05	1.41	0.47 [e], 0.35 [f], 0.77 [h]	S [h]	Wrong
valsartan	Hep/IPA	0.51	0.18	0.38	0.15	0.27	0.17	1.29 [a]	R [a]	Wrong
Cooreln. Coeff. S/R [i]		0.368	0.274	0.002	0.391	0.122	-0.215			

[a] David House, Orochem Technologies, Inc.

[b] α=3.04 for trans stilbene in hexane/isopropanol, with the (1R,2R)-(+) enantiomer eluted as the first peak; α=1.12 for flavanone in hexane/isopropanol, with the (R)-(+) enantiomer eluted as the first peak; from [122].

[c] Resolution was R_S = 10.6 for trans stilbene oxide in n-hexane/isopropanol (90 :10, v/v), with the (1R,2R)-(+) enantiomer eluted as the first peak, from [123].

[d] α=2.17 for flavanone in methanol, with the (R)-(+) enantiomer eluted as the first peak, from [124].

[e] Ref [127].

[f] α=1.44 for ambucetamide in acetonitrile, α=1.40 for etozoline in acetonitrile, α=2.89 for thalidomide in methanol, from [128].

[g] α=1.48 for naringenin in n-heptane/isopropanol (90 :10, v/v), with the (S)-enantiomer eluted as the first peak, from [126].

[h] α=1.30 for thalidomide in methanol, with the (S)-(-) enantiomer eluted as the first peak, from [125].

[i] Excluding valsartan in the correlation plot.

itself also has rings and, indeed, only chiral enantiomers with a ring system can be separated by a chiral stationary phase. We mentioned earlier that the hydrogen bonding interactions are buried inside the cavities and are flanked by rigid and bulky phenyl groups which are located at the surface ; therefore, the latter are expected to control access to the hydrogen-bonding sites via steric factors. Repulsive interactions dictate where the rings of the drug molecule can and cannot be absorbed on the polymer surface. Since the enantiomers are mirror images of each other, occupiable spaces are different for the two enantiomers ; the permitted proximity of the hydrogen bonding acceptors or donors on the drug to the donors and acceptors on the ADMPC is thereby limited for the two enantiomers. Effectively, this permitted proximity is what each enantiomer has to work with, and it can optimize the forming/breaking hydrogen-bonding with the ADMPC. It is therefore of interest to characterize and examine the ring-ring interactions between drug and ADMPC. Using only distances between ring centers provides is less informative. Instead, we map out the distribution of angles between the ring normals of drug and ADMPC, in order to quantify the distribution of parallel stacking as opposed to other arrangements. It can also be used to determine how the π-π stacking structure may increase or diminish the ability of the donor and acceptor sites to get close to each other.

For benzene dimer, CCSD(T) calculations reveal that the interaction is attractive in nature for three canonical structures : parallel displaced, T-shaped edge-to-face, and eclipsed face-to-face, with a preference for the parallel displaced and T-shaped edge-to-face geometries [129] (Fig. 3.10). The canonical structure called eclipsed face-to-face corresponds to angles $\gamma = 0°$ and $\theta = 0°$, $\mathrm{R}_{\mathrm{cen}} = 3.8$ Å, whereas the canonical edge-to-face structure corresponds to angles $\gamma = 90°$ and $\theta = 0°$, $\mathrm{R}_{\mathrm{cen}} = 5$ Å ; and the parallel displaced structure corresponds to angles $\gamma = 0°$ and $\theta = 63°$, $\mathrm{R}_{\mathrm{cen}} = 4$ Å.

However, heteroatoms on the ring or substitution of H by other functional groups, even CH_3, make a significant difference [130]. Thus, the example of benzene dimer is not sufficient to represent the π-π interaction since polarization or enlargement of the π system changes the preferred intermolecular arrangement dramatically ; so do the presence of polar or non-polar solvents.

As a widely accepted concept, a chiral recognition rationale which entails attractive face-to-face or parallel displaced π-π interaction in conjunction with hydrogen bonding has often been used to explain separation performance. [131] In this work, we try to find an applicable metric for a wide variety of chiral drug molecules interacting with the ADMPC chiral stationary phase in various solvent systems. The dynamic nature of the separation process indicates that using specific static arrangements as outcomes is not sufficient ; therefore, we consider the distribution map of different arrangements involving aromatic ring(s) of both the chiral molecules and ADMPC's side-chains. Angles and distances which define the relative coordinates of the two rings are shown in Fig. 3.11.

The theoretical calculations indicate that the interaction between two aromatic rings is attractive over a range of distances, still significant at 5 Å for the eclipsed face-to-face and parallel displaced, for which the minimum occurs at 4 Å, while the edge-to-face is still significantly attractive up to 6.5 Å, for which the minimum occurs at 5 Å. Note that we are using the ring on the drug molecule as our reference point to define the angle θ. Thus, the configuration $\theta = 90°$, $\gamma = 90°$ is also an edge-to-face structure. [129]

Before scattering the angles on the distribution map, we first calculate the R_{cen}-R_{cen} the distance. We only show the angles for ring-ring interactions when R_{cen} does not exceed the distance threshold. For center-to-center distances R_{cen} ranging from <4.4 Å up to <5.4 Å between a specific ring on the enantiomer and the shortest ring on the ADMPC, we plot the map of the angles γ, θ and the vector R_{cen} which have been illustrated in Fig. 3.11. Here, we show only the results where R_{cen} is less than 4.4 Å. The colors from blue to red represent the density of the data points going from low to high. The ring-ring configurations are found to be very dynamic in all MD simulations. However, ring-ring interactions may retard or facilitate the formation of hydrogen-bonds, despite their broadly varying configurations. We then look into the distribution of orientations between the drug ring and the closest ring in the ADMPC. In Fig. 3.12, we give the results for each of the two phenyl rings of benzoin (solvents : heptane/isopropanol 90 :10) as our example. The illustration of how we number the phenyl groups of benzoin is shown in Fig. 3.8.

(a) Both the phenyl groups of the benzoin molecule behave very dynamically when they are interacting with phenyl groups on the ADMPC's side-chains.

(b) The classical MD has its limitation on interpreting molecular and atomistic electron states. So as its drawback on π cloud in the aromatic system. So, the canonical structures calculated by CCSD(T) rarely show up here. We see that $\gamma = 0°$, $\theta \approx 0°$s (eclipsed face-to-face), $\gamma = 0°$, $\theta \approx 60°$ (parallel displaced) and the edge-to-face structure ($\gamma = 90°$, $\theta = 0°$) are not represented at all, for ring #1 or for ring #2. Recall that the angle θ is referenced relative to the ring of the drug molecule, so this edge-to-face configuration corresponds to the drug phenyl ring with its edge to the center of an ADMPC ring. Another edge-to-face structure ($\gamma = 90°$, $\theta = 90°$) is not populated either ; this corresponds to the ADMPC phenyl ring with its edge to the center of the drug phenyl ring. Thus, neither aromatic ring on benzoin appears to have long-time involvement in supportive $\gamma - \theta$ interactions with the chiral stationary phase.

(c) At these close distances there is an observed preference for average angles in the vicinity of $\gamma = 15 \pm 10°$, $\theta = 30 \pm 10°$ for both rings in benzoin and the ADMPC rings.

(d) For both R and S enantiomers, the phenyl group attached to OH (ring #1), in the top figures, has a larger number of short-range interactions with the rings of the polymer compared to the phenyl group attached to C=O (ring #2), in the bottom figures. This has a more physical meaning because the hydroxyl group is known to have stronger hydrogen-bonding ability than carboxyl group.

(e) The angle distribution maps for R benzoin differ from that of S benzoin ; that is, Model 2 ADMPC discriminates between the two enantiomers in terms of the ring-ring interactions.

In order to have a better understanding on the role of ring-ring interactions in chiral recognition, we investigate the distribution of angles (γ, θ) for each of the rings in benzoin with the rings on the ADMPC polymer, only for the time frames where a hydrogen-bond between the drug and the ADMPC is maintained in the trajectory (Fig. 3.13). There are fewer points, but the highly probable angles (the bright regions in the angle distribution maps) are the same as in Fig. 3.12. The paucity of the canonical structures of the type eclipsed face-to-face, parallel-displaced, etc. that we have seen in Fig. 3.12 is likewise found here. The angle distributions are more sharply distinct between S and R benzoin in Fig. 3.13 where at least one hydrogen-bond between the drug and the ADMPC forms. This indicates that formation of a hydrogen bond between the drug molecule and the ADMPC is often accompanied by preferential distribution of ring-ring angles, telling us that persistent hydrogen bonds are often assisted by ring-ring interactions, and that the hydrogen-bonding and ring-ring orientations are coordinated. For the hydrogen-bonded benzoin there is an observed preference for average angles in the vicinity of $\gamma = 10°$, $\theta = 30°$ for both rings in benzoin and the ADMPC rings. In comparison to Fig. 3.12, Fig. 3.13 have more points, but the highly probable angles shown by the bright regions are unchanged, and no population at all corresponding to the canonical structures, except for occasional observations close to $\gamma = 90°$, $\theta = 90°$ for ring #1.

The number of incidences of ring-ring distances $R_{cen} < 4.4$ Å is greater for ADMPC Model 1. The general trends (a)-(b) of ring-ring orientations are the same for both unrestrained (Model 1) and restrained (Model 2) ADMPC polymer. However, there are some other important differences. For Model 1, the angle distribution maps are barely distinguishable for R and S, with most probable angles around $\gamma = 15°$, $\theta = 30°$ for both rings in benzoin and the ADMPC rings. Furthermore, when only those time frames that have a hydrogen-bond between the drug and the ADMPC in a 100 ns trajectory are collected, the angle distribution maps are again nearly indistinguishable for R compared to S, with most probable angles in the vicinity of $\gamma = 15°$, $\theta = 30°$ for both rings in benzoin and the ADMPC rings. Therefore, Model 1 is much less discriminating than Model 2, not only in hydrogen-bond interactions but also in ring-ring interactions.

Apart from the dynamic properties we have found in the distribution plot, we also examine one of the snapshots corresponding to a long-lived hydrogen-bonded configuration. We look at the orientation of the drug molecule, particularly the arrangement of the drug rings relative to the ADMPC rings. This is only one example of the great multitude of "docked" positions for the S versus the R chiral drug. We show these two snapshots, one for S enantiomer and the other for the R enantiomer hydrogen-bonded to ADMPC in Fig. 3.14.

To guide the eye, the hydrogen bond in these snapshots is illustrated by an arrow from donor to acceptor. In both S and R cases, the hydrogen-bonds form as the NH of the carbamate toward the carbonyl of the benzoin, $C{=}O_{drug}$ - HN_{csp}. We also use dashed lines to join the ring centers to indicate the ring-ring interactions between the ADMPC and the benzoin. The distance R_{cen} is shorter than 4.4 Å as we have discussed above. We see that for the S enantiomer (left Fig. 3.14), the assistance of rings from ADMPC polymer appear to keep the benzoin ring #1 in place and thus facilitate the orientation of the whole benzoin molecule. This special arrangement is helping to stabilize the C=O group on benzoin to form the hydrogen-bond with the carbamate group on the ADMPC. The benzoin ring #2 is also involved in an interaction with the carbamate group of the ADMPC. These two correspond to the following geometries : R_{cen} = 4.4 Å and angles $\gamma = 23.5°$, $\theta = 37.1°$, and R_{cen} = 4.8 Å, $\gamma = 40.9°$, $\theta = 27.0°$. For the ring #2 next to the acceptor C=O group : R_{cen} = 4.6 Å to the closest ring of the ADMPC and ring-ring orientation angles are $\gamma = 8.8°$, $\theta = 32.7°$. Although such ring-ring arrangement facilitates and stabilizes the acceptor C=O group towards forming the hydrogen bond, none of these ring geometries is close to the attractive canonical structures.

On the other hand, in the R benzoin (right Fig. 3.14), ring #1 (the ring next to the OH in benzoin) is stabilized by two ring-ring interactions, like the S benzoin. Those geometries are as follows : R_{cen} = 4.5 Å and angles $\gamma = 59.6°$, $\theta = 39.6°$, and R_{cen} = 4.4 Å, $\gamma = 11.3°$, $\theta = 41.0°$. Still the same, none of such geometries is close to the canonical structures. For the R benzoin, no ring-ring interactions are involved for the ring #2 next to the acceptor C=O. So it cannot be stabilized to form the hydrogen-bond between the C=O on the drug and the H-N on the ADMPC.

The structures in Fig. 3.14 are consistent with proposed standard models of 3 contacts for chiral recognition. However, each of the individual snapshots in Fig. 3.14 corresponds to only one specific long-lived hydrogen bonded configuration, chosen from the 300 ns of simulations individually for R and S. So, each of the two structures in Fig. 3.14 is only one of a multitude of structures formed during the MD runs ; the dynamic nature of the drug-ADMPC interactions, as clearly demonstrated in the distribution of γ and θ angles, or even the distribution of γ and θ angles for the selected set of hydrogen bonded structures, do not permit a metric for HPLC separation factors to be developed from using only static pictures like these structures in Fig. 3.14.

3.4 Conclusion

By using atomistic and classical MD with GAFF, we found the solvent effects on the ADMPC polymer structure. This finding is supported by the changes in the helical structure of the ADMPC in different solvents, and we have characterized these changes in terms of the distribution of the dihedral angles of the glycoside bond between adjacent monomers of the ADMPC. We find in the present work, that in the three systems we studied, (acetonitrile , heptane/2-propanol and methanol) the ADMPC has different distribution of dihedral angles of the glycoside bonds. Therefore, we believe we have a general explanation for differences in separation factors in different solvent systems for the same drug and the same CSP. Any changes in the average backbone structure that is characterized by the glycosidic dihedral angle maps translate to concomitant changes in dynamic structure for the side chains, of course. The MD simulations include all of that, as well as any dynamic changes accompanying the formation of the transient diastereomers between enantiomer and CSP in different solvent systems.

Then, by using a weakly restrained polymer to consider the actual experimental condition of polymers being coated on a solid support rather than floating in solution, we have developed a predictive molecular model for the experimental elution order of enantiomers and for the experimental value of the separation factor. The criteria that we have considered are the number of time frames in which a hydrogen bond is found between the drug molecule and the ADMPC, the maximum lifetime of hydrogen bonds, and the average lifetime of hydrogen bonds. At the present stage of this work, the best correlation provides separation factors with a correlation coefficient of better than 0.85 and the elution order is predicted correctly for all but thalidomide in the 11 cases. Both the longest of the maximum lifetimes of hydrogen bonds between specific donor acceptor pairs, as well as the weighted average of the maximum lifetimes, including all donor-acceptor pairs between the drug and the ADMPC, provide good correlations between the S/R ratios of the metric with the S/R separation factor from experiments. Our model predicts which of the enantiomers elutes first and this becomes very clear when we examine the 3 mentioned MD criteria for each donor-acceptor pair in turn. The preference for R or S is found, in many cases, to be the same for each donor-acceptor pair in the system, thereby providing a consistent prediction of which enantiomer elutes first.

By considering both an unrestrained ADMPC polymer in solution and we have found that the individual donor-acceptor hydrogen bonding partners between enantiomer and restrained polymer present a more consistent prediction of which enantiomer elutes first, whereas the results are mixed and less consistent in the unrestrained case, making the predictions less reliable. The relative success of our present weakly restrained polymer and the observations that the unrestrained polymer provides a too loose, less defined chiral landscape than is necessary for chiral discrimination, favor the weakly restrained model.

The molecular dynamics simulations provide a picture of ring-ring interactions between drug and ADMPC that is very dynamic and has a very broad distribution of ring-ring orientations at close range ; none of the highly probable orientation angles are found to correspond to the canonical attractive structures for benzene dimer. No ring-ring orientations are long-lived, that is, none persist for several sequential time frames, unlike the hydrogen bonds. Not observed are any eclipsed face-to-face, parallel displaced structures, nor any structures in which the drug phenyl ring edge is oriented towards the face of an ADMPC ring. Another edge-to-face structure does appear to be populated ; this corresponds to the ADMPC phenyl ring with its edge to the center of the drug phenyl ring. Orientation angles found are largely between

40 and 80 degrees for the angle between the normal to the drug ring and the vector that points to the center of the closest ring, also for the angle between the two ring normals.

Nevertheless, when we further examined ring-ring orientation angles for only those time frames where an instantaneous hydrogen bond exists between drug and ADMPC, we find that the preferred orientations under these conditions are more constrained than those that are generally observed throughout the trajectory, indicating that while the encounters are highly dynamic, hydrogen bonding and ring-ring interactions are coordinated. However, even for the time frames in which at least one hydrogen bond exists between the drug enantiomer and the ADMPC, none of the observed ring-ring angles comes from the canonical structures often used to explain which enantiomer elutes first or last.

Finally, we examined one particular snapshot involving a long-lived hydrogen-bonding interaction ; and we looked at the orientation of the S and R enantiomers relative to the ADMPC, paying particular attention to the orientations of the drug rings relative to the closest ADMPC rings. This is only one example of the great multitude of "docked" positions for the S versus the R enantiomer formed during the MD run, only one snapshot out of the entire MD trajectory, altogether 300 ns long ; the dynamic nature of the drug-ADMPC interactions does not permit a metric for HPLC separation factors to be developed from using only static pictures such as an individual snapshot extracted from an MD run.

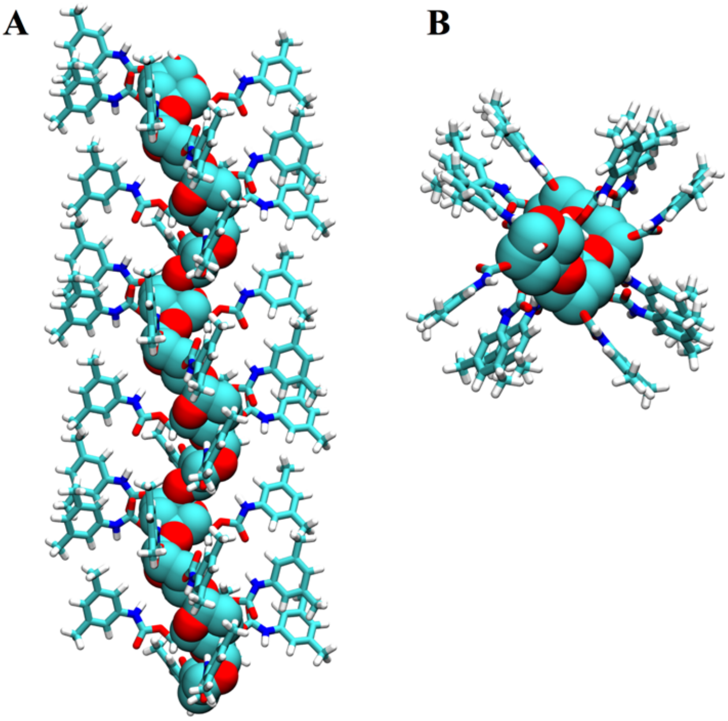

Figure 3.1. Structure of the initial configuration of ADMPC including a side view (A) and a top view (B). The backbone atoms are represented with VdW spheres and the derivatives are represented with sticks. Hydrogen atoms are in white, carbon atoms are in cyan, nitrogen atoms are in blue, and oxygen atoms are in red.

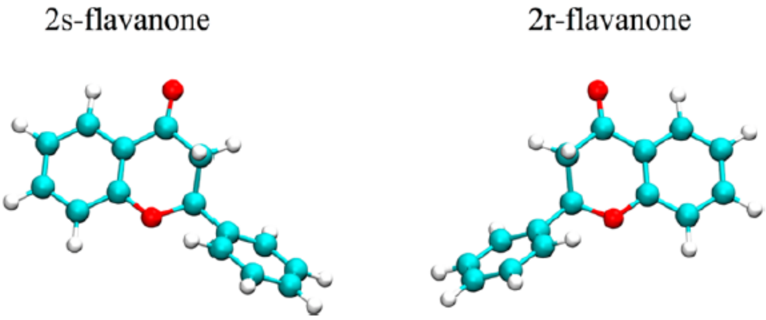

Figure 3.2. Molecular structure of flavanone enantiomers, 2s-flavanone (left) and 2r-flavanone (right). The molecules are depicted with ball-and-stick models with cyan beads representing carbon atoms, red beads representing oxygen atoms, and white beads for hydrogen atoms.

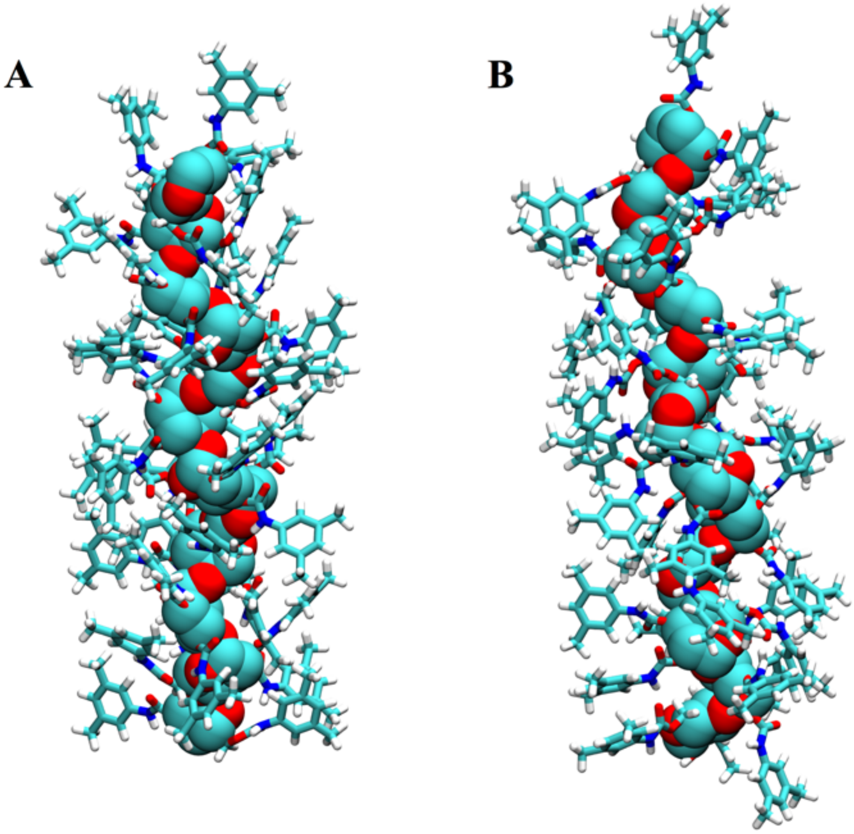

Figure 3.3. Average structures of ADMPC in methanol (A) and 90/10 Hep/IPA (B). The backbone atoms are represented with VdW spheres and the derivatives are represented with sticks. Hydrogen atoms are in white, carbon atoms are in cyan, nitrogen atoms are in blue, and oxygen atoms are in red.

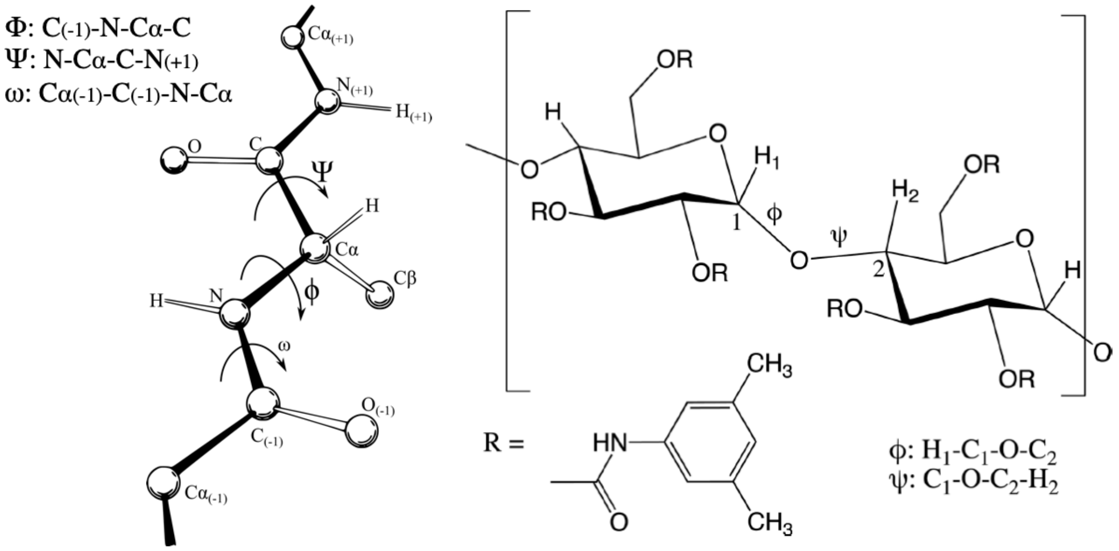

Figure 3.4. Representation of the dihedral angles of : two adjacent peptide bonds (left), represented by Φ : $C_{(-1)}$-N-Cα-C and Ψ : N-Cα-C-$N_{(+1)}$; the glycoside bond between two adjacent monomers in ADMPC (right), represented by Φ(H1-C1-O-C2) and Ψ(C1-O-C2-H2).

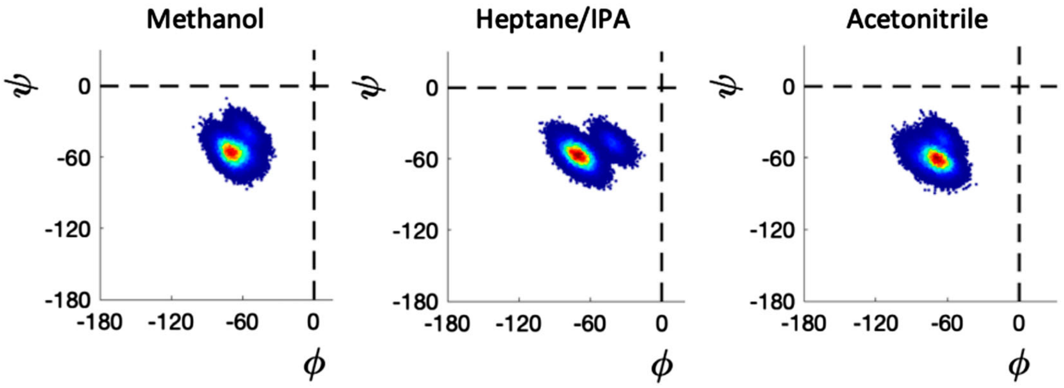

Figure 3.5. Maps of dihedral angles of the glycoside bond between adjacent monomers of the 12-mer of ADMPC in methanol, heptane/IPA and acetonitrile, using Model 2. The colors from blue to red represent the density of the data points going from low to high. Of the four quadrants (Φ, Ψ) = -180 to +180, we only show the populated quadrant. The colors go from blue to red representing the density of points from low to high in various (Φ, Ψ) regions.

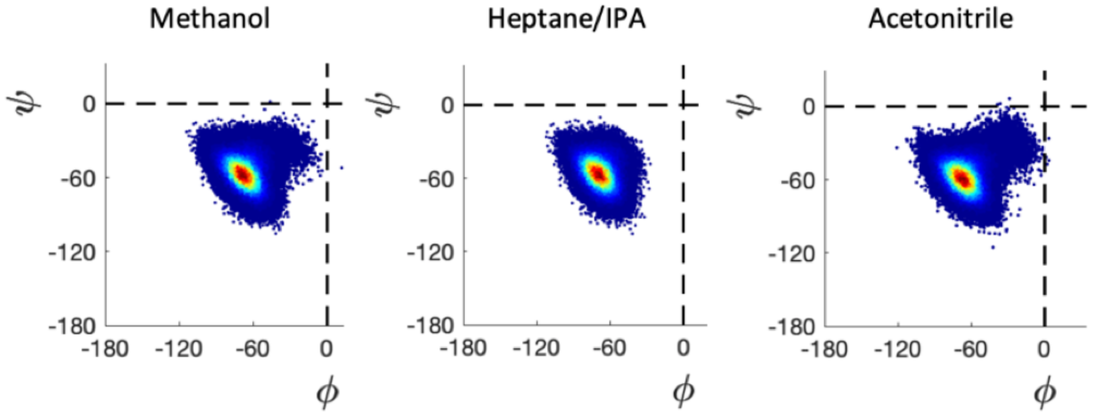

Figure 3.6. Maps of dihedral angles of the glycoside bond between adjacent monomers of the 12-mer of ADMPC in methanol, heptane/IPA and acetonitrile, using Model 1. The colors from blue to red represent the density of the data points going from low to high. Of the four quadrants (Φ, Ψ) = -180 to +180, we only show the populated quadrant. The colors go from blue to red representing the density of points from low to high in various (Φ, Ψ) regions.

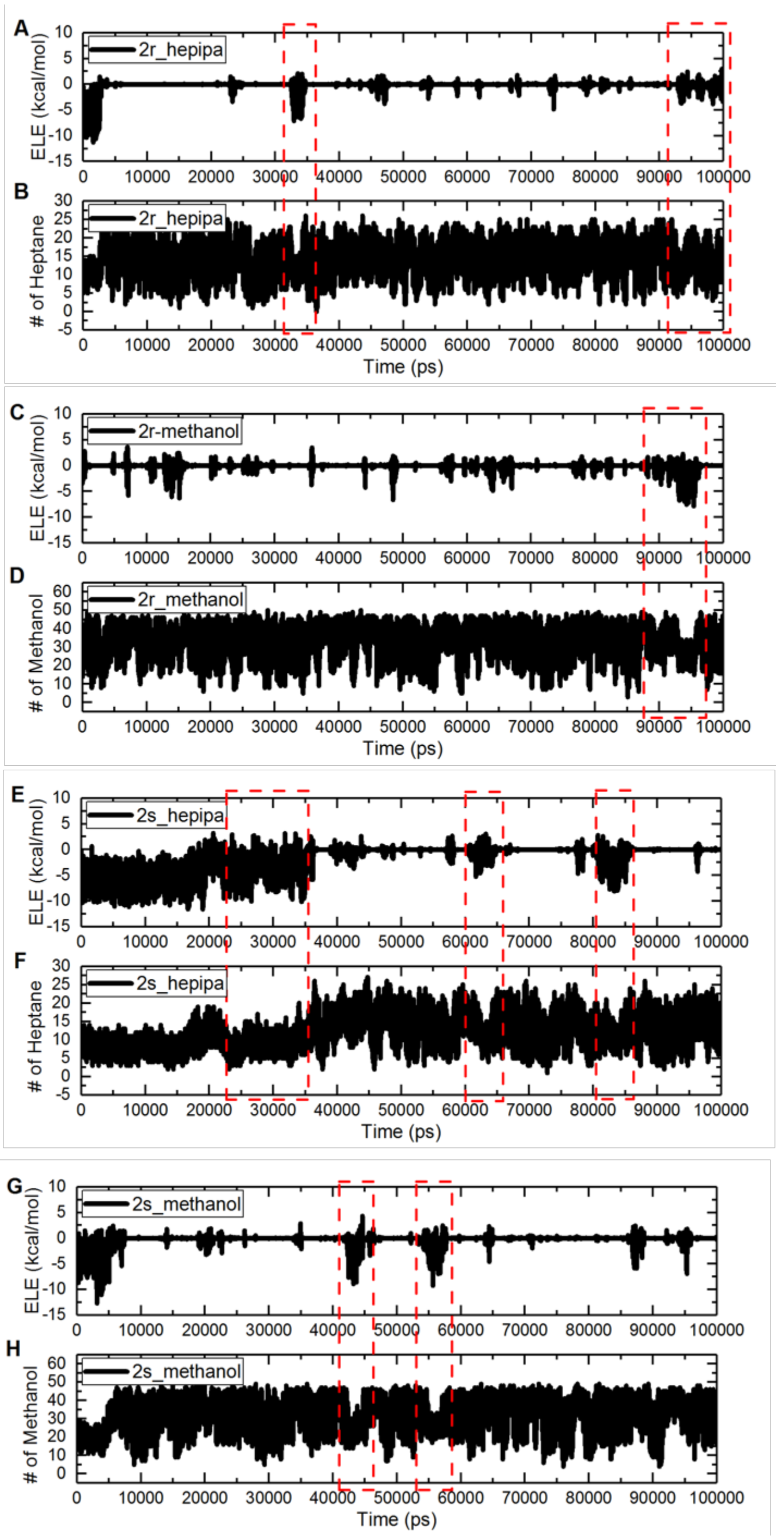

Figure 3.7. Electrostatic energies between flavanone isomers and ADMPC (A, C, E, G) and the number of solvent molecules in the first solvation layer of the drug over simulation time (B, D, F, H). The time frames where there is a correlation between electrostatic energy and the number of solvent molecules are enclosed in red dashed rectangles. Note the difference in scale between (B, F) and (D, H).

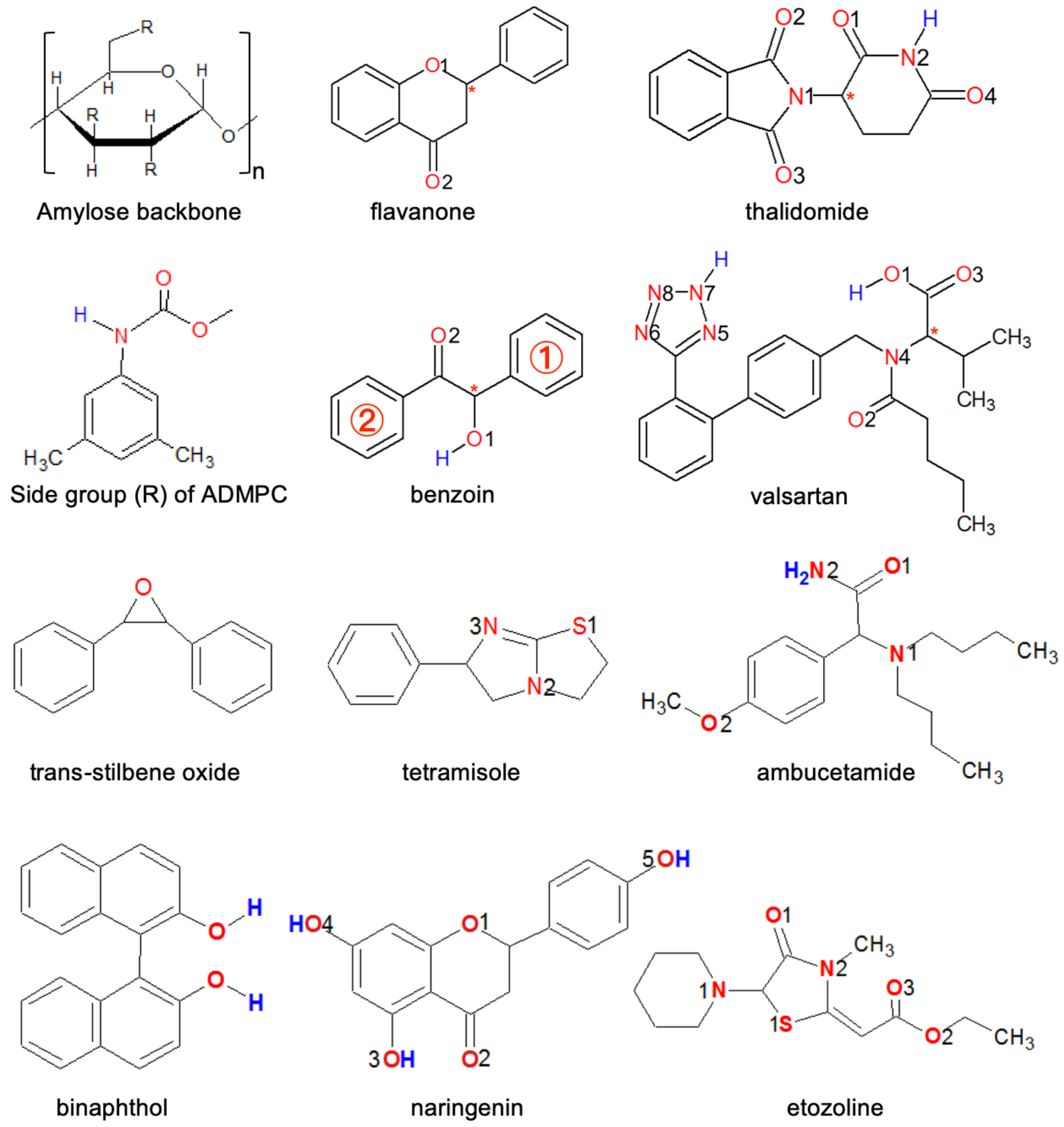

Figure 3.8. The molecules in this study can form donor-acceptor pairs with the amylose tris(3,5-dimethylphenyl carbamate) (ADMPC) polymer strands, one side chain of which is shown here. The hydrogen bonding donor and acceptor sites in the molecules and the ADMPC are indicated : red O or N for acceptors, an attached blue H denotes donors.

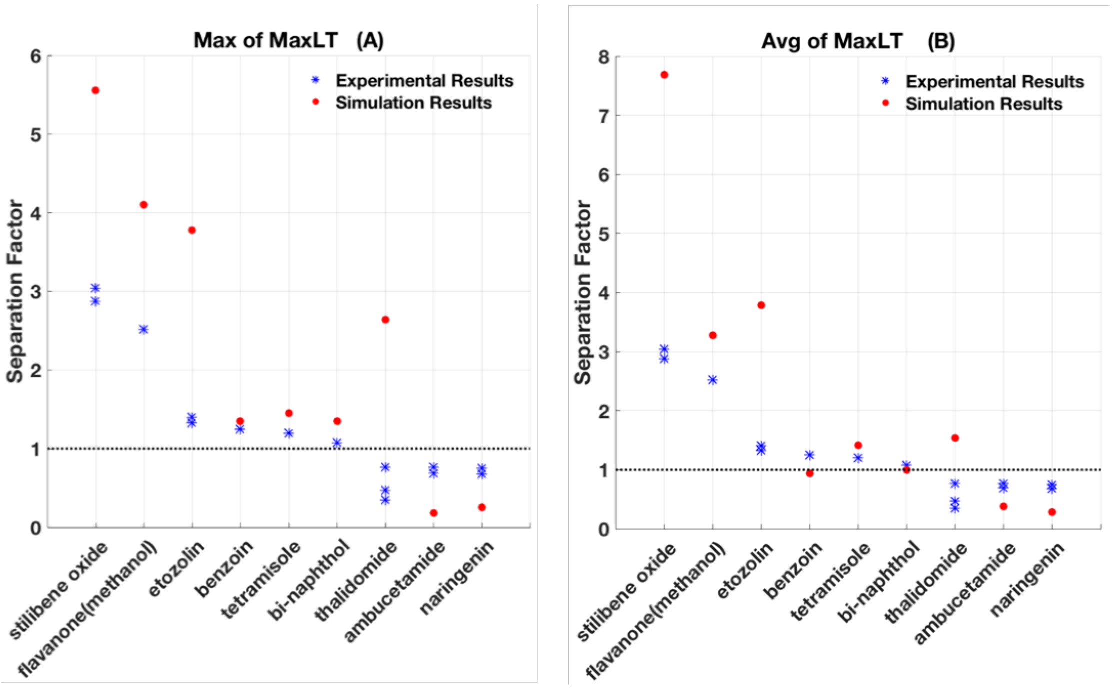

Figure 3.9. A summary of the prediction of separation factors. Plotted along the Y axis, the ratio of the metric (in blue) is calculated for S/R, as is the ratio of experimental retention times (in red). The MD results used for this plot are from Table 3.4.

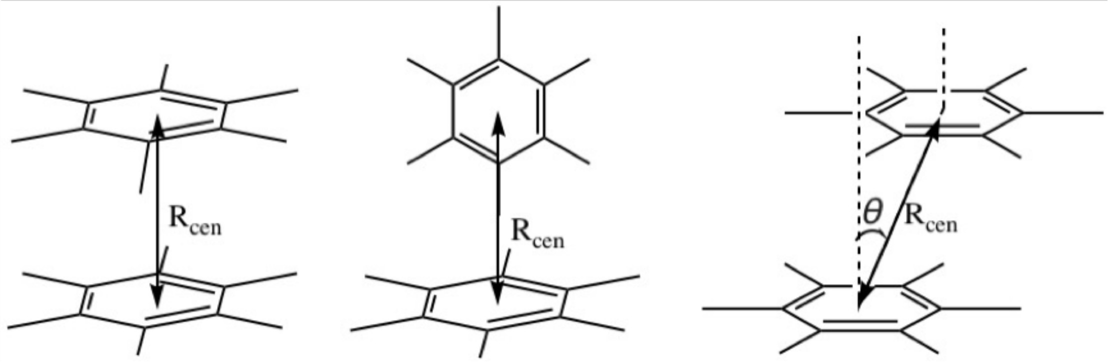

Figure 3.10. Canonical structures for benzene dimer : eclipsed face-to-face, edge-to-face, and parallel displaced, respectively, from left to right.

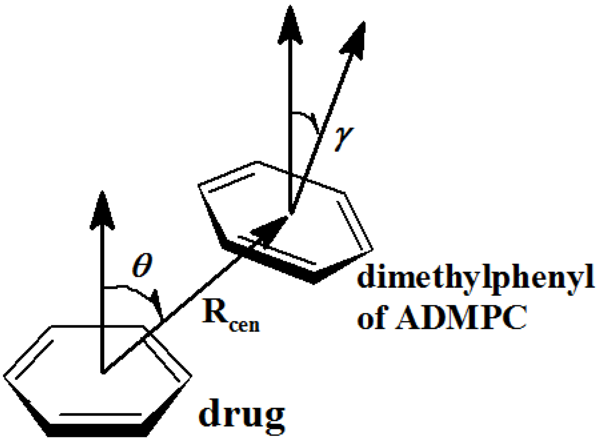

Figure 3.11. Definition of distances and angles in the interaction between a ring on the drug molecule and a ring on the ADMPC polymer.

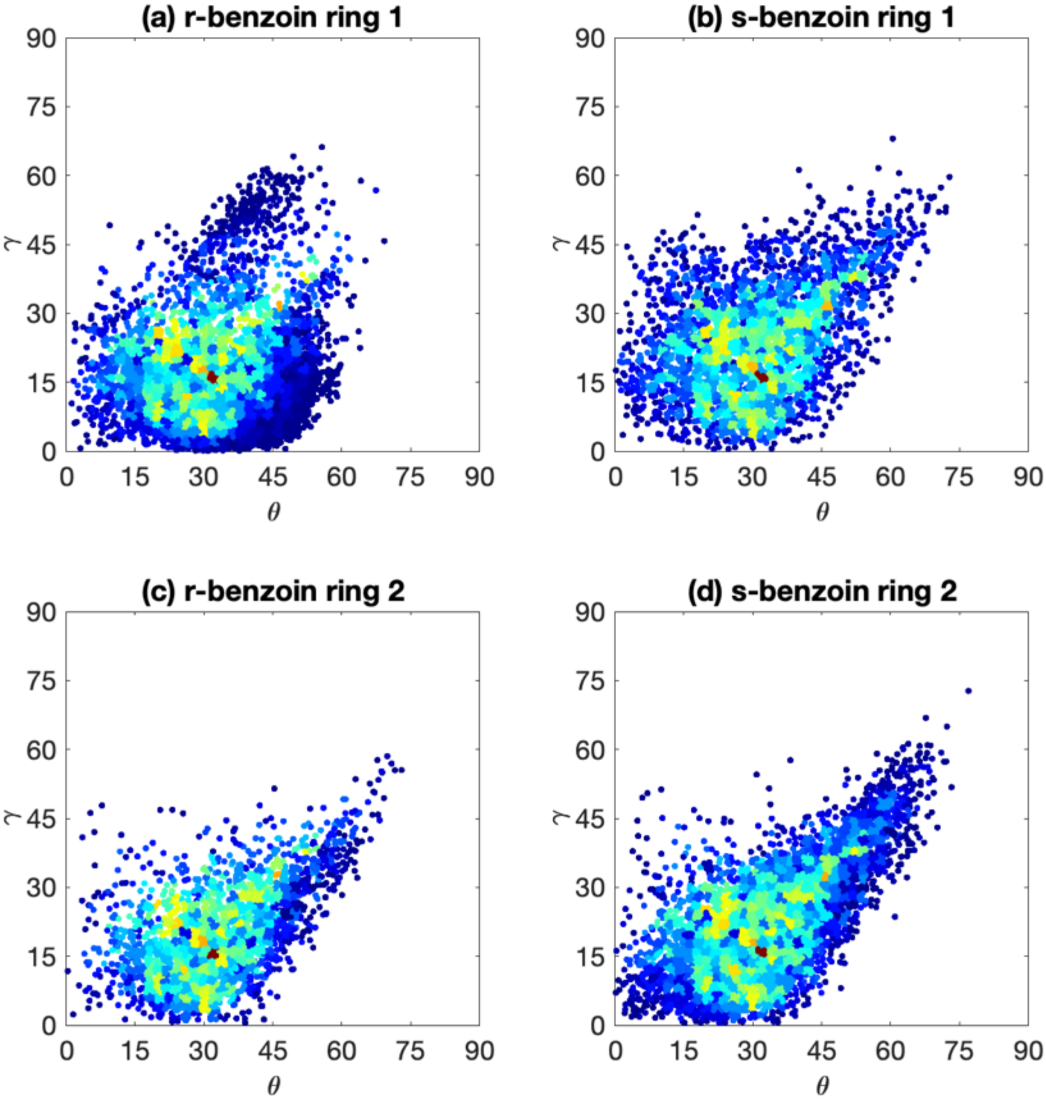

Figure 3.12. Map of the angles describing the distribution of relative orientations of the phenyl rings (γ = vertical axis, θ = horizontal axis), found for distances less than 4.4 Å between the center of the phenyl ring #1 (next to the OH group) and ring #2 (next to the C=O group) of the benzoin molecule and the closest ADMPC phenyl ring. The colors from blue to red represent the density of the data points going from low to high. The results are based on snapshots uniformly taken from a 100 ns trajectory, (a) for the R enantiomer (b) for the S enantiomer for ring #1, (c) for the R enantiomer (d) for the S enantiomer for ring #2, using Model 2.

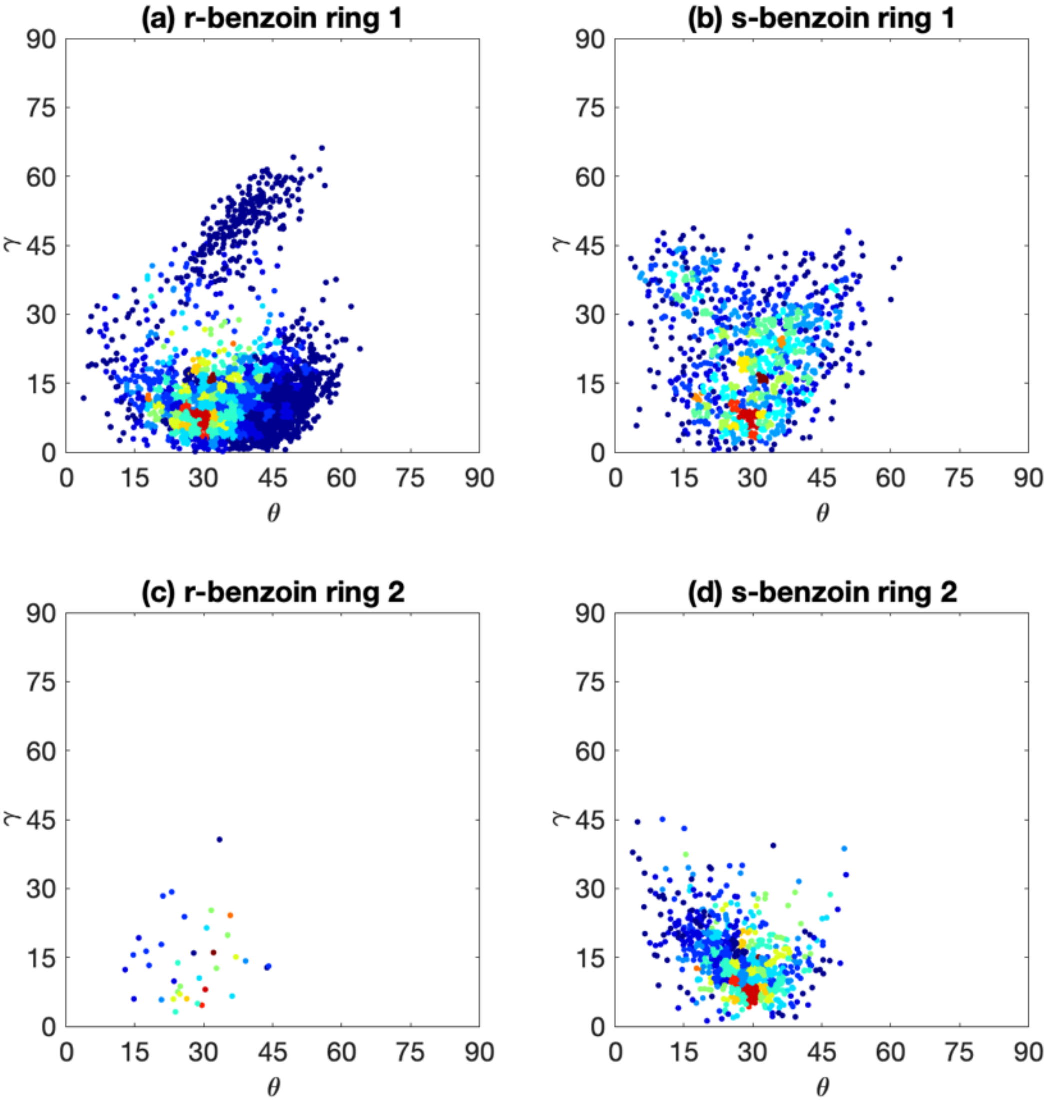

Figure 3.13. Map of the angles describing the distribution of relative orientations of the phenyl rings (γ = vertical axis, θ = horizontal axis), found for distances less than 4.4 Å between the center of the phenyl ring #1 (next to the OH group) and ring #2 (next to the C=O group) of the benzoin molecule and the closest ADMPC phenyl ring collected from only those snapshots where a hydrogen bond exists between the enantiomer and the ADMPC, taken from the same 100 ns trajectory as Fig. 3.12, (a) for the R enantiomer (b) for the S enantiomer for ring #1, (c) for the R enantiomer (d) for the S enantiomer for ring #2, using Model 2. The colors from blue to red represent the density of the data points going from low to high.

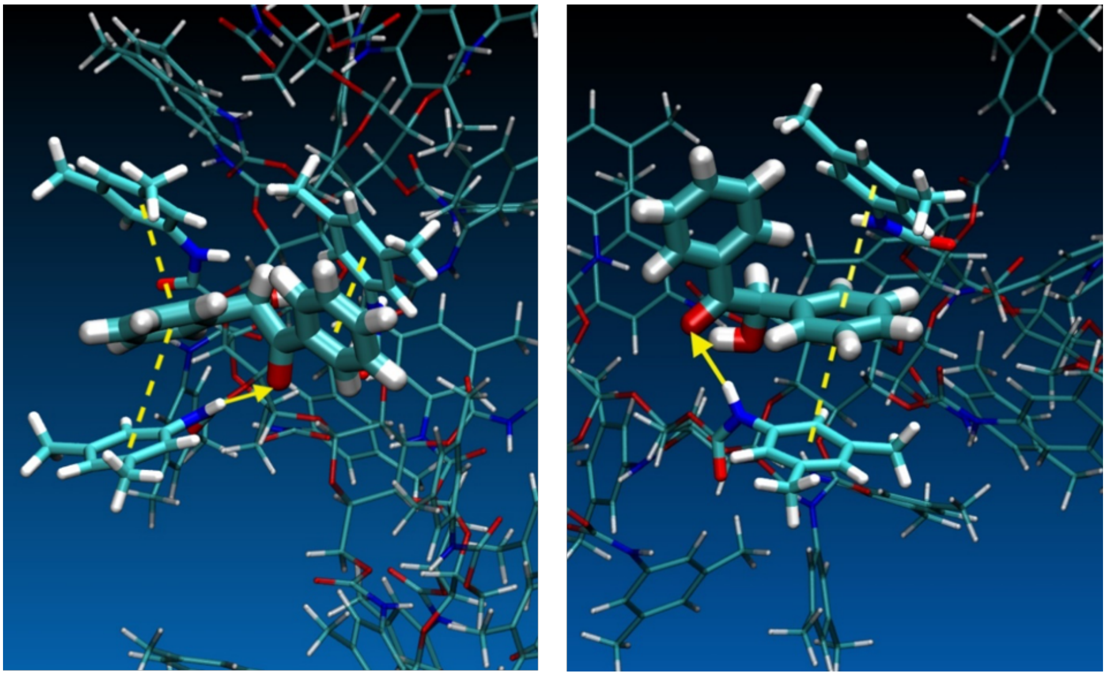

Figure 3.14. One of a multitude of possible structures formed during a 100 ns MD run, for the S (left image) and the R (right image) enantiomers of benzoin, in a time frame where a long-lived hydrogen bond is formed. In each case, the ring-ring interactions between benzoin and the ADMPC are indicated with dashed lines connecting the centers of the rings that have R_{cen} close to 4.4 Å, and the donor to acceptor hydrogen bonding is indicated by the arrow. Oxygen is red and nitrogen is blue.

CHAPTER 4

MODELING ENANTIOMERIC SEPARATIONS AS AN INTERFACIAL PROCESS USING AMYLOSE TRIS (3,5- DIMETHYLPHENYL CARBAMATE) (ADMPC) POLYMERS COATED ON AMORPHOUS SILICA

4.1 Introduction

In the previous chapter [132] [133], we have used explicit-solvent fully atomistic molecular dynamics (MD) simulations (permitting all the interactions between the atoms constituting the polymeric chiral stationary phase (CSP), the solvent molecules and the drug molecule) to better understand the chiral recognition mechanism that makes the separation possible. Using amylose tris(3,5-dimethylphenyl carbamate) (ADMPC) as our prototype, along with three different solvent systems and ten different enantiomers, we found several molecular dynamics average quantities related to hydrogen-bonding lifetimes are found to correlate with the ratio of retention times for the enantiomers. One of these quantities provides a prediction of the correct elution order 90% of the time, and the ratios of these quantities for the enantiomers provides a correlation (0.85 coefficient) with the experimental separation factor (the ratio of retention times). Nevertheless, this work needs to be improved further for general use, as discussed below.

A single 12-mer strand of the chiral stationary phase may be an insufficient model. We carried out equivalent studies : one in which the drugs interact with a 12-mer of ADMPC which is freely floating in explicit solvent (Model 1) and another in which the 12-mer is restrained with a weak harmonic potential for each atom of the polymer after equilibration in the solvent (Model 2). The purpose of this restrained polymer study is to discover the extent to which the free movement of all atoms of the short polymer in solution permit greater sampling by donor-acceptor groups. In the case of the restrained polymer, all atoms are still dynamic, but the cavities for "docking" are very regular and consistent in the free volume available to the enantiomers ; and this situation may be more typical of very long polymers laid down on the silica support. From the previous work [132] [133], using Model 2, a restrained 12-mer pre-equilibrated in the solvent system appears to be a reasonable model for MD simulations of drug-CSP interactions that form the basis for enantiomeric separation in HPLC where the polymer is coated on the solid support. The prediction is not perfect, for 10 drugs, we failed to predict which of S or R elutes first in at least one case, with mixed predictions coming from different metrics in three cases. In one case, while the simulation predicted the correct enantiomer to elute first, there was too great a preference of the polymer for the other enantiomer compared to experiment. Furthermore, with the restrained model, even though the correlation coefficients are close to 0.8, we observe the correlation plots are far from a slope of unity, as they would be in an ideal prediction. Thus the need for improved models is obvious.

In order to allow the flexibility of ADMPC, we introduced a third model in which only the backbone atoms of the ADMPC 12-mer are restrained, with the atoms of the side chains free to move. In a separate study, we considered this model (we will call it Model 3) using the same set of 10 drugs with the ADMPC in their respective solvent systems to find out whether Model 3 could give results that may or may not be improved over previous Models 1 and 2. However, Model 3 turned out to be as poor as Model 1 ; after finishing the simulations for four drugs, benzoin, flavanone, naringenin and valsartan in heptane/isopropyl alcohol (90/10) solvent system, in which all results gave the wrong prediction for the elution order, we abandoned this model. The reason underlying this bad performance is that this model still allows too much freedom for the side chains, which leads to no discrimination of the handedness of the enantiomers.

In this chapter, we consider a much more realistic Model 4 which consists of polymer chains on an amorphous silica surface. This model has a more realistic representation when taking the experimental conditions into consideration. (a) The presence of multiple ADMPC strands is included, thus permitting polymer chain-chain interactions, and also allowing an enantiomer to interact with more than one AMDPC strands simultaneous. (b) There is no ad hoc restraint on the atomic motions as what we applied in Models 2 and 3. (c) The atomistic effects of the silica on the structure and dynamics of the polymer are also considered. (d) The interaction regions presented by the ADMPC to an enantiomer is somehow limited : only the approach from the polymer surface is allowed, while in Model 1-3, all radial directions towards the single chain are possible. (e) Another improvement is the usage of four 18-mer ADMPC strands instead of a single 12-mer one. We seek an understanding of the role played by the solid support, and we seek to discover whether Model 4 leads to consistent predictions for which of S or R elutes first, and whether the MD metrics that we have previously developed with the earlier simpler models correlate well enough with experimental separation factors to be used for predicting the magnitudes of the separation factors a priori. We test the Model 4 with 4 sets of enantiomers : benzoin and valsartan in hep/IPA (90/10), and flavanone and thalidomide in methanol ; their structures have been shown in Fig. 3.8.

4.2 Methods

4.2.1 Building the Model for the Amorphous Silica. First of all, we need a silica slab. Our model of the surface of the solid support is based on a model of an amorphous silica interface [134] that captures the essential experimentally known properties. The amorphous silica interface consists of two types of groups, silanol and siloxane groups. The siloxane groups are hydrophobic in general, while the silanols are hydrophilic. The typical density of silanol groups is 4.6 OH/nm^2 [135] [136] which is confirmed by experiments provided by Zhuravlev et. al. However, the type of silanols, not only their density, determines the hydrophilicity of the silica surface. Silanol groups are classified as three types : isolated (single silanols), geminal (2 OH groups per Si) and vicinal (bridged OH groups) [136]. Experimentally, according to the Zhuravlev model, they are present in the following surface densities : 1.2, 2.80, and 0.60 OH/nm^2 for isolated, vicinal, and geminal, respectively.

4.2.2 Preparation of a Starting Configuration for the Amorphous Silica Slab. Different methods using different force fields have been documented to generate amorphous silica. The GLASSFF force field provided in Cerius2 [137] had been used to generate a starting structure in the paper that developed the CWCA force field by Schulten et al. [138] A Morse-style potential developed by Demiralp et al. [139] was parameterized to predict phase transitions in ceramics including silica. A well-trained ReaxFF, the ReaxFF-Si/SiO/SiN by Fogarty et al., [140] optimized from the original ReaxFF-Si/O/H of van Duin et al., [141] showed good agreement with both experiment and quantum mechanical calculations.

In our study, a fresh-cut structure of amorphous silica slab [138] was used as initial starting configuration and its dimension is 78 × 78 × 15 Å. Then we applied ReaxFF-Si/SiO/SiN [140] in the annealing and quenching processes, which can cap the dangling atoms introduced by the fresh-cutting. LAMMPS [61] software package was used as the MD engine to simulate annealing ; a time step of 0.25 fs was used throughout this part. A short timestep was used because we are simulating condensed matter where atoms are packed tightly. Longer time steps may lead to program crashing. First, an NVE ensemble coupled with a Berendsen thermostat [117] at 300 K was deployed for 50 ps to eliminate initial overlapping atoms and minimize the energy of the system. For the first annealing process, we used Nose-Hoover style non-Hamiltonian NVT ensemble [64] [65]. The system was heated up to 4000 K and gradually cooled down to 300 K at the rate of 25 K/ps. After that, in the second annealing process, the system is heated to 4000 K again using an NPT ensemble, keeping a constant pressure of 1 atm for 75 ps. We only applied barostatting on the x and y directions ; the simulation box on z direction was kept constant, resulting in a thin slab structure after quenching. The system was cooled down from 4000 K to 300 K at a rate of 25 K per ps. Such a procedure resulted in a silica slab with dimensions of 72.475 × 72.475 × 15 Å.

4.2.3 Preparation of the Silanol-Capped Surface. The silica slab was then submerged into a 72.475 × 72.475 × 45 Å box where the structure was surrounded by water molecules, as shown in Fig. 4.1. ReaxFF-Si/SiO/SiN [140] was used here which allowed the reactions to happen on the silica surface and to cap those dangling Si and O atoms. An NVT ensemble was used because the difference in compressibility between silica and water could otherwise produce an undesirable structure where silica was surrounded by water in all three directions.

First, a 70 ps simulation was carried out and then the velocities were reassigned with a gaussian distribution at a temperature of 300 K, then the final equilibration lasted for 580 ps. This procedure generated a structure of silanol-capped silica which has the right structural details compared with experiments : the silanol density is 4.72 $\#/\text{nm}^2$ on the surface, which agrees reasonably and acceptably with the experimental value of 4.6 $\#/\text{nm}^2$ [135] [136] ; the distribution of silanol types is 1.26, 2.23, and 1.23 $\#/\text{nm}^2$ for isolated, vicinal, and geminal, respectively, which agrees reasonably well with experimental distribution (1.20, 2.80, 0.60 $\#/\text{nm}^2$, respectively), although a somewhat higher germinal density. After equilibration, all the unreacted water molecules were stripped from the box. This silanol-capped silica structure could then be used in the following steps.

The CWCA force field [138] incorporated the CHARMM water contact angle Lennard-Jones and bond parameters, so it was used throughout the rest of simulation steps. A similar study about the silica surface with a uniform silanol density of $4.62/\text{nm}^2$ was conducted by Benjamin et al. [142] [143]. They also tested the CWCA force field in their MD simulation studies of binary solvent mixtures (methanol, ethanol, acetonitrile) on the silica surface. Leroch et al. [144] tested several available force fields. Among them, the Clay force field and CWCA for the silica interface have a lower silanol density of 3.0/nm^2 and almost all the silanol groups are isolated. The set of force field parameters we used (CWCA) are therefore well tested against many experimental quantities as described in these references. Since the number and composition of atoms deviated slightly from the original CWCA paper, the charges on the silicon atoms attached to silanol groups and silanol oxygen and hydrogen are scaled to set the total charge to zero. In order to maintain the bulk silica structure without collapsing, the bulk atoms were self-tethered to their initial positions by a harmonic force of 500 kcal/mol/Å^2. The parameters are summarized in Table 4.1.

Table 4.1. Parameters used for silanol-capped amorphous silica

Non-bonded interactions	ϵ kcal/mole	σ Å	e q
Si (bulk)	0.300	3.825	0.900
O_b (bulk)	0.150	3.118	-0.4500
Si (silanol)	0.300	3.825	0.9021
O_h (silanol)	0.300	3.118	-0.6579
H_h (silanol)	0.046	0.713	0.4321
Bonds	K_b kcal/mole	R_0 Å	
Si-O_b	885.10	1.61	
Si-O_h	428.00	1.61	
O_h-H_h	554.13	1.00	
Angles	K_a kcal/(mole*rad^2)	r_0 degree	
O_b-Si-O_h	153.26	111.09	
O_h-Si-O_h	89.62	116.26	
Si-O_h-H_h	57.50	106.0	

4.2.4 Coating the ADMPC Polymers on the Amorphous Silica Surface in Vacuum. First, we constructed 20-mer chains which has the same repeatable monomer as the 12-mer model by Yamamoto et al. [95] After equilibrating the 20-mer in the particular solvent system for 100 ns, cluster analysis was carried out using the same approach [116] as described in the previous chapter. From the results of the cluster analysis for the backbone atoms, a single representative structure of ADMPC was generated in each solvent system (heptane/IPA or methanol). We then removed one monomer from both ends and used only the 18-mer structure in the following coating process, for several reasons. The periodic silica base is expanding periodically on x and y dimensions and we need full coverage by ADMPC of the silanol-capped surface. Four 18-mer units would cover the silanol-capped silica slab. Practically, the polymer-coated silica surface has hardly any exposed silanols. Otherwise the enantiomers would form hydrogen-bonds with the silanols, causing severe tailing of the HPLC peaks.

We characterized the chain backbone structure by mapping the population of the torsional angles, Φ : H1-C1-O-C2, Ψ : C1-O-C2-H2 in a Ramachandran-like plot, as in our previous work [133] [132]. Chirality of ADMPC results from the backbone composed of the glucose units, the chirality inherent in the periodic helical grooves in the polymeric backbone. So, another critical point is to maintain polymer structure and helical properties while coating them onto the silanol-capped silica slab using van der Waals forces. In industry, gradual evaporation of the solvent is usually used, thus only polymers would be left on the surface eventually. By this way, structural properties of the polymer are ensured as in the solvent atmosphere. In simulations, introducing the polymer strands to the silica in the presence of solvent would permit the solvent molecules to form strong hydrogen-bonds with the silanols on the silica surface, interactions that are far stronger than the van der Waals interactions of the polymer chains to the silica surface. Thus, in simulations, ADMPC polymers in the presence of solvent would never have the chance to stick onto the surface.

To prevent the problems listed above, we developed a multi-step simulation strategy which is explained in more detail as follow. Our purpose of such strategy is to explore a way that would pack polymers onto the silica slab without leaving unnecessary exposed silanol groups, and without changing its solvent-swollen configurations.

We tried two strategies to avoid these problems. In the first, we placed four chains close to the silica surface without solvent and ran the MD simulation in vacuum. This resulted in 4 polymer strands being van der Waals attached to the silica surface. (Note that in the absence of solvent, the polymer chains in vacuum are shorter compared to the equilibration in solutions. The solvent molecules can form hydrogen-bonds with the CO and NH sites of the polymer, thereby resulting in the dynamic structure of the polymer in solution to be swollen compared to that in vacuum.) We then introduced the solvent into the simulation box and ran NVT MD simulations for four periods of 100 ns. To test whether the polymer chains came to equilibration on the silica after the solvent had been introduced, we checked the Ramachandran-type maps of the (Φ, Ψ) angle distributions between adjacent glucose units for all joints of all four ADMPC strands; maps were plotted from the last 20 ns of a 100 ns MD simulation. We discovered that the swelling process must take a much longer time than 400 ns to reach the correct polymer structures. During the equilibration, the polymer ends are free to move out as they permit the solvent to intercalate in the grooves; this process starts from a free end unit and continues along toward the middle part of the chain. However, the middle units are more restricted in their dynamics, since they have connections on both sides. Therefore, even after 400 ns, while the Ramachandran angle distributions for the end units are in accord with the idealized case, some of the middle units are clearly not. Thus, it is NOT feasible with this procedure to reach the solvent-equilibrated structure of ADMPC polymers on amorphous silica.

We considered a second procedure for arriving more quickly to the equilibrium condition for ADMPC on the silica slab in the presence of solvent. Our packing method consists of several steps. First, four arrangements of solvent swollen polymers are placed on top of the silica slab in vacuum at a distance larger than the cut-off distance. Then, we apply "fix/rigid" [145] [146] at 298 K in LAMMPS to treat the backbone as a rigid system to maintain the solvated inter-monomer spacing. In the implementation of "fix/rigid", the total force and torque on each rigid body is computed as the sum of the forces and torques on its constituent particles. The coordinates, velocities, and orientations of the atoms in each body are then updated so that the body moves and rotates as a single entity. We use the equilibrated solvent-swollen average structure for the 18-mer for each of the 4 chains to be placed with the silica slab for equilibration in vacuum, keeping the backbone rigid, while the side chains are mobile. The edge atoms of the backbone are tethered to each other artificially to keep an inter-strand distance of 18 Å, which can permit the four strands to expand throughout the surface area and form a seamless membrane to cover the silica surface. The spacing condition along with the "fix/rigid" is applied throughout the packing-in-vacuum processes. Nose-Hoover style non-Hamiltonian NVT ensemble at 298 K with a time step of 0.2 fs and a total of 200,000 steps (40 ps) is used. The polymers are allowed to associate with each other in vacuum without touching the silica surface. It is easier to control the inter-strand spacing without involving the silica slab because the polymer motions would be restricted by van der Waals forces when they sit on the silica surface. Then, a 5 kcal/mole-Å ; force towards the silica slab is applied to backbone atoms to force the associated polymers move toward the silica surface. Another 40 ps allows the polymers to associate with the surface (0.2 fs/step, 200,000 steps). At the end, the force toward the silica surface is removed to let the polymer strands adjust their structures (40 ps, 0.2 fs/step, 200,000 steps). In this way, we can preserve the equilibrated solvent-swollen spacing of the backbone groups and permit only the side chain atoms to individually move while equilibrating the polymer strands on the silanol-capped amorphous silica slab in vacuum.

In addition to the chirality of a single polymer strand, there is a supramolecular chirality in the regions between adjacent polymer rods, which was not included in single-polymer-strand models. Since the ADMPC has a handed helical structure (left-handed 4/3 helix), we should consider parallel or antiparallel arrangements of polymer strands, such as those in Fig. 4.2. The equilibration described above was carried out for each of the arrangements shown in Fig. 4.2. After the equilibration in vacuum is done, the solvent molecules are then introduced into the simulation box.

4.2.5 Relaxing the ADMPC on the Amorphous Silica Surface in the Presence of Solvent. Fig. 4.3 shows a sketch of system setup for preparing the solvated ADMPC on amorphous silica. PACKMOL [120] package was used to introduce the solvent molecules into the simulation box. The total number of solvent molecules introduced into the box is determined according to the experimental density and composition. The size of the simulation box is 72.475 × 72.475 × 90 Å. We used a wall with bcc structure on the bottom of the box to prevent solvent molecules from interacting with the bottom surface of the silica when periodic boundary conditions are applied. We then deployed two energy minimization steps. First minimization only included solvent molecules, while the second one included solvent and side chain atoms. Energy minimization iterations were ended by one of the four criteria : the tolerance for energy is 0.0 (unitless) ; the tolerance for force (Kcal/mol-Å ;) is 1.0×10^{-8} ; maximum iteration steps ares 1000 ; maximum number of force/energy evaluations is 100,000. The Polak-Ribiere version of the conjugate gradient algorithm was used for minimization [62]. The "fix/rigid" and spacing conditions are kept to run MD simulation for 500 ps (0.5 fs/step, 1,000,000 steps). Then, the "fix/rigid" was removed and simulations ran for another 500 ps (0.5 fs/step, 1,000,000 steps). At last, the spacing condition was removed for 500 ps (0.5 fs/step, 1,000,000 steps). We stripped the solvent molecules which were clogged in-between the ADMPC and silica surface and put them back into the bulk solvent region. Those solvent molecules would otherwise interact with the silanol groups on the surface, which would eventually increase the distance between ADMPC and silica surface, weaken the VDW forces holding the ADMPC, and result in the polymer chains being lifted up from the silica surface.

The following step is to relax the ADMPC polymers in the solvent atmosphere. In this step, we changed the software package from LAMMPS to AMBER [33], so that AMBER's GPU acceleration feature could largely reduce the time to complete simulations. Then, we carried out three steps of minimization by self-tethering different groups and gradually releasing them. First, the silica, BCC wall and ADMPC polymers were tethered (strength was 1000 kcal/mol) and we ran MD for 100,000 steps (0.1 fs) to equilibrate the solvent only. Second, we ran MD for another 100,000 steps (0.1 fs) with releasing ADMPC's side-chains from the self-tethered group. Third, only the solid part, including silica and the BCC wall, were tethered and the simulation ran for another 100,000 steps (0.1 fs). Then, we increased the energy barriers of the joint glucoside dihedrals from the default GAFF library [11] by a factor of 10 and ran MD simulations for 60 ns with a time step of 2 fs. Finally, the barriers were down to normal and the simulation ran for another 40 ns without any constraints to equilibrate the ADMPC polymers in solvent atmosphere. We had to pay special attention to the methanol solvent and avoid any interactions between the OH and the silanol groups of the underlying silica. Such strong hydrogen-bonding interactions between solvent and silica support should not occur in practice, especially when the silica is entirely covered by the ADMPC. We accomplished this by artificially adjusting the Lennard-Jones parameters for these interactions (increasing the distance parameter by factor of 2 and the well depth by a factor of 2 compared to the default GAFF values.

We prepared several equilibrated systems which include various parallel and antiparallel arrangements of the polymer chains as described in Fig. 4.2. We tested the completeness of equilibration in each case, shown by the uniformity of the Ramachandran angle distribution plots for each monomer-monomer joint, and also by the regularity of the van der Waals surfaces presented by the 4 ADMPC strands on the silanol-capped silica. We carried out those same procedures for two solvent systems individually : methanol and hep/IPA (90/10). The final configurations served as starting points from which the enantiomer molecules would be introduced.

4.2.6 Interacting the Enantiomers With ADMPC on Silica. We started the chiral recognition runs with multiple strands of ADMPC on silica, considering various combinations of parallel and antiparallel arrangements. Each of the arrangements had been pre-equilibrated on the silanol-capped silica surface and with solvent, either methanol or hep/IPA (90/10), without the enantiomers being introduced. We tested four racemates to validate the Model 4 : benzoin (in hep/IPA), valsartan (in hep/IPA), flavanone (in methanol) and thalidomide (in methanol). 5 molecules of each enantiomer were placed in the simulation box and the simulations ran for 200 ns. We do this, rather than only a single enantiomer molecule at a time for efficiency. However, we also monitored and took steps to minimize dimerization of enantiomers. Methods of analyzing hydrogen-bonding lifetimes and the ring-ring interactions between the enantiomers and the ADMPC are still the same as described in the previous chapter [132]. We first analyzed results from each of four arrangements (aaaa), (aabb), (abba), and (abab) individually, to test whether parallel or antiparallel arrangements of the helical polymer strands would provide different results for the hydrogen-bonding statistics and the ring-ring interactions. Then, we combined the results together, resulting in equal contributions from parallel and anti-parallel arrangements, for an overall analysis using the same six MD metrics that we had introduced in previous work [133] [132].

4.2.7 Some Thoughts on the Development of Model 4. Fig. 4.4 shows a summarized process flowchart for Model 4. The following discussion on the development of Model 4 will provide some thoughts and insights of why those steps are meaningful and important.

In the development of the amorphous silica slab, the height of the fresh cut slab must be more than the cut-off distance used throughout the whole MD simulations. This is to ensure that the bottom surface silanol groups will not interfere with the interaction at the interface. Such interference rarely happens because the actual size of a real silica slab is normally larger than simulated size. Although there is no mandate of the width and the length of the slab, the choice should be based on the computational resource. A wider silica slab can support more stationary phase polymers and provides more statistics when sampling the interactions between drug molecule and polymer. But this means a larger simulation system and a more expensive MD simulation. One should also be careful about the number of polymer strands on the silica surface and make sure that the whole surface area is covered with polymers properly. Any exposed silanol group is undesirable since it can hydrogen bond with drug molecules without discriminating their handedness. They can also hydrogen bond with solvent molecules, which may weaken the interactions between polymer and silica surface.

The force field and the software package used to anneal the silica slab need not be limited to the ones in the flow chart. Other options using classical MD or even Ab-Initio MD can be substituted as long as the model is confirmed by experiments and theoretical studies. Another important thing has to be paid attention to is that the dangling atom should be all capped with silanol group. Otherwise, the dangling oxygen or silicon could lead to wrong hydrophilicity of the silica surface and, even worse, an unneutralized system. One can double check this by counting the number of silicon, oxygen and hydrogen atoms, and calculating the oxygen/silicon ratio : H = O - 2*Si ; O/Si > 2/1. The usage of ReaxFF in this study has a main drawback that the types of silanol groups on the surface(isolated, vicinal, and geminal) do not have the exact number/area density when compared with experiments. Although the ReaxFF proved to be accurate compared with theoretical studies including QM/MM and DFT calculations, the original optimization of parameters for ReaxFF should have included the experimental –OH distributions of three –OH types, not just the average.

The polymer strands must be associated above the silica surface before laying down for the reason that, after being laid down, the polymers are reluctant to move due to the attraction provided by the silica surface. The spacing distance has to be chosen carefully because : too short a distance may deform the polymer structure ; too long a distance may not be sufficient to let the side chains associate with each other. The temporary rigidifying on the backbone of ADMPC has been justified and described in the previous section. In summary, the space controlling and backbone rigidifying are the two important conditions that should be maintained throughout the development of Model 4.

If we start with an initial condition where the molecules are packed tightly in the simulation box, the unstable situation will make the componenets lose their structure, including ADMPCs, drugs and silica slab. However, their structures have been equilibrated and developed through multiple-stage thoughtful steps, so the deformation is somehow unwanted. It is almost always wise to self-tether some molecules to its original coordinates at the very beginning of the equilibrating steps. An initial self-tethering condition is also necessary to maintain the chirality of the drug molecules. In the process of sampling interactions between drugs and ADMPCs, the energy barrier on the chiral center will normally prevent the drug molecule inverting its chirality, while unstable situations may lead to the drug molecules overcoming such a barrier. We relax the system and make it come to equilibrium by gradually removing the constraints : first equilibrating the solvent system by self-tethering drugs, ADMPCs and silica ; then keeping the backbone rigid and controlling distance between two ADMPCs while relaxing ADMPC side groups and the solvent system ; then relaxing the backbone but still keeping the distance controlled ; finally removing all constraints.

Fig. 4.3 shows a schematic picture of the arrangement of the simulated system. The BCC wall is applied to prevent the redundant bottom silica side from adsorbing and hydrogen bonding with molecules. An exposed silica surface with silanol groups contacting with solvent system will lead to the adsorption of solvent molecules and drug molecules : the absorption of alcohol molecules will result in an unrealistic solvent stratification ; the absorption of chiral molecules will result in the loss of effective reactants. The choice of the height of the simulation box must satisfy the following requirements : the distance of the BCC wall to the effective ADMPC surface has to be larger than the cut off distance ; the thickness of solvent phase has to be more than two cut off distances. Those requirements will ensure that any undesirable interactions are kept off at a safe distance from the effective ADMPC surface.

4.3 Results and Discussions

4.3.1 Structural Characteristics of ADMPC Polymer Backbone on Amorphous Silica. First, we analyzed the structures of the polymers equilibrated with the respective solvents on the silica. There are several key questions we need to pay attention to.

(a) We investigated the Ramachandran-type maps of dihedral angles of the glycoside bond between adjacent monomers (Φ, Ψ) for each the parallel or antiparallel arrangement. We want to find if the joints between monomers are uniformly similar, irrespective of the arrangements.

(b) We want to find if these Ramachandran-type maps in Model 4 differ from those in Model 1 or Model 2.

(c) Based on (a) and (b), we try to find how restrained are the ADMPCs in Model 4, compared to Models 1 and 2. Is this dependent on the parallel/antiparallel arrangement of the polymer strands on the silanol-capped silica ?

In Fig. 4.5, the Ramachandran maps of dihedral angles shows the property of the glycoside bond between adjacent monomers of the four 18-mers of ADMPC on silanol-capped silica in solvents. We presented separated plots for the various parallel/antiparallel arrangements of polymer on the silanol-capped silica. in Fig. 4.6, we then combined the results for the various arrangements by equally weighting them, to produce the overall combined distributions of backbone structures. In Fig. 4.5, we also compare the backbones of ADMPC in Model 4 with those of Model 1 and Model 2.

By investigating the distribution of (Φ, Ψ) torsion angles through the Ramachandran like plots, we find :

(a) The distributions are confined to the same quadrant in all cases. Despite the dynamic structure of the polymer shown as points scattering around the high probable area, the regularity is found for both solvent systems in Fig. 4.5 for all parallel/antiparallel arrangements. Also, this regularity is similar to what was observed in the single polymer strand in the solvent system. The most probable angles is around (Φ, Ψ) = (-65°, -55°) for the 4 strands on the silica slab in both hep/IPA and in methanol. This is very close to that observed for a single polymer strand in three solvent systems (Φ, Ψ)= (-60°, -65°) [132].

(b) The distributions differ slightly with the parallel-antiparallel arrangements of four ADMPC strands. Larger scattering area is observed in methanol than in hep/IPA (as seen in Fig. 4.5). While the differences occur in the low probability angles, the high probability angles remain the same.

(c) In Fig. 4.6, we shows the overall distribution of angles for Model 4 (averaged over various parallel/antiparallel arrangements) in (a) hep/IPA and (b) methanol solvent systems with no constraints. As observed, the scatters are generally more compact in hep/IPA than in methanol solvent. This differ from the previous Model 1, where the Ramachandran plot showed a more compact distribution in methanol than in hep/IPA [132]. Nevertheless, differences again occur only in the low probability angles, the high probability angles remain the same.

(d) Comparison of the Ramachandran plots for the present Model 4 with Models 1, 2, and 3 in Fig. 4.7 indicates that regularity in backbone structure is observed for all models. The plots also indicate that the distributions are confined to the same quadrant in all cases with differences that occur primarily in the low probability angles. However, Model 1 appeared much more spread out compared to Model 2 or 4, thus presenting, on average, a less regular, less discriminating chiral sites to approaching enantiomers.

4.3.2 Enantiomer Interactions With Multi-Strand ADMPC Polymer Surface Compared to Single ADMPC Strand. For a particular enantiomer, when analyzing particular arrangements separately, we seek answers and clues to the following questions.

(a) Would different antiparallel or parallel arrangements of ADMPC give similar or uniquely different results for hydrogen bonding statistics ?

(b) Would there be any incidences when enantiomers were simultaneously interacting with two adjacent ADMPC strands ?

(c) Would such incidences depend on the parallel/antiparallel arrangements of the polymer on the silica?

For a closer view, in Fig. 4.8, we show the van der Waals surfaces presented by the polymer chains on the silica in the presence of hep/IPA. All the four strands have similar grooves to accommodate solvent or the enantiomers, the symmetry of the chains is similar to, but not identical to the structure in the Model 1. In Fig. 4.8, we picked and compared one particular polymer strand in Model 4 with (a) the perfect Okamoto structure, and (b) the single polymer strand in the solvent (Model 1).

There have been some earlier studies on trying to use polymers-on-silica model to investigate the recognition of chiral separation. Li et al. [107] used a silica model where silanol groups were fully end-capped with aminopropyl silane and a 13-mer ADMPC segment was selected from a 36-mer equilibrated in vacuum by choosing the segment with the greatest number of chiral cavities. They fixed the backbone dihedral angles (Φ, Ψ) at exactly (-68.5°, -42.01°), the same number that had been reported for ADMPC in solution in $CHCl_3$ by Yamamoto [95]. Then, they used rigid enantiomers and rigid ADMPC in vacuum to carry out docking simulations. In contrast, our Model 4 has more advantages over their model for the following reasons : (a) we incorporate the solvent into the system rather than do simulations in vacuum, (b) we include more than one polymer chain, which provides the possibility of chain-chain interactions as well as an enantiomer interacting with 2 (or more) chains simultaneously. Furthermore, in our work, the MD simulations of the interactions of enantiomers with the ADMPC are fully atomistic and fully dynamic, occurring without any restraints of any kind, and equilibrated with solvent.

We observe a number of incidences when an enantiomer of a drug, namely valsartan, is hydrogen-bonded to two ADMPC chains simultaneously. We show some examples demonstrating this phenomenon in Fig. 4.9. Although such incidences do not dominate the overall results, only Model 4 can allow such occurrences to be included ; single strand models of Models 1-3 miss these events entirely. In the examples shown in Fig. 4.9, the close contact with two adjacent strands involves hydrophobic interactions with one strand, simultaneously with hydrogen bonding to the other strand, and such incidences were found in all the arrangements in the figure. In the particular zoom-in snapshot shown in Fig. 4.9, a valsartan ring forms a displaced face-to-face interaction with a phenyl ring of one ADMPC strand, while the C=O3 of the valsartan is close enough to the H-N of the adjacent ADMPC strand to form a hydrogen bond.

Antiparallel or parallel arrangements of polymer chains on the silica do not provide very different results for benzoin or flavanone. Since the enantiomer has long-lived interactions with only one polymer at once, the adjacent parallel or antiparallel ADMPC polymers have very little influence on the hydrogen-bonding events. Only in the case of valsartan do we observe the enantiomer interacting with two polymer strands simultaneously, as seen in the snapshots in Fig. 4.9. It might be explained by the fact that the larger molecular size of valsartan than benzoin or flavanone could permit it to lie across two polymer strands, thus allowing such incidences to happen. However, such incidences as in valsartan would be common for larger drug molecules.

4.3.3 Analysis of Hydrogen Bonding Lifetimes. The distribution of hydrogen bonding lifetimes for benzoin is shown in Fig. 4.10. It is constituted from the combined results for all arrangements of the ADMPC strands. We display for each donor-acceptor pair between the enantiomer and the ADMPC the counts of incidences of various lifetimes (in picoseconds) of a hydrogen bond ; i.e., a time period when the hydrogen bonding structure remains present consecutively in the trajectory. Each donor-acceptor pair is labeled separating, with their lifetimes binned. Different colors are used to distinguish the results for different pairs.

The distributions of lifetimes of hydrogen bonds between various donor-acceptor pairs are notably different for the S and R enantiomers of benzoin. As seen in Fig. 4.10, the S enantiomer has consistently many more incidences of longer lifetimes compared to R, for each donor-acceptor pair. In this distribution display, we are also able to spot the donor-acceptor pair that provides the longest lifetime and largely contributes to the metric, namely "Max of Max LT". Considering the dynamic property of the interaction between the benzoins and the ADMPCs shown by Fig. 4.10, we note that this specific metric alone, especially for benzoin, could not provide a correct prediction. The tall bars which corresponds to lifetimes shorter than "Max LT" would contribute the most to "Avg LT" for each donor-acceptor pair. From the Fig. 4.10, we can already conclude that S-benzoin would elute last, which agrees with experiment (Ref. [132]), even without carrying out the averages metrics. Each of the four individual arrangements of parallel and anti-parallel strands also lead to the same conclusion, as can be seen in Fig. 4.12, despite the small differences of the actual distributions. For each arrangement, comparing individual hydrogen-bonding partners, the lifetime distributions clearly indicate that the lifetimes for the S-benzoin are collectively longer than for the R enantiomer. This seems to indicate that the inter-strand structure is not able to influence the hydrogen-bonding between the enantiomers and the ADMPC side-chains.

From the distributions seen in Fig. 4.11 for flavanone in methanol, we are still able to read from the figure that S should elute later, in agreement with experiment (Ref. [133]), even without carrying out the average for the metric, namely "Overall AvgLT". Although in this particular example, "Max of MaxLT" would give the same conclusion, the latter metric neglects all the dynamic information contained in the entire distribution of hydrogen-bonding lifetimes in Fig. 4.11.

There are significantly larger number of donor-acceptor pairs in the two other drugs. The distributions for thalidomide in methanol and valsartan in hep/IPA are shown in Fig. 4.13 and 4.14 respectively. For thalidomide, the distributions of lifetimes in Fig. 4.13 clearly show that longer lifetimes exist for the R than the S enantiomer, consistently for most of the donor-acceptor pairs. The previous Model 2 entirely missed two leading contributions to hydrogen bonding partners for the R enantiomer, thus it failed to arrive at the correct answer that S thalidomide elutes first in experiments. [125]

For valsartan in hep/IPA, the distribution of lifetimes in Fig. 4.14 clearly shows longer lifetimes for the S relative to the R enantiomer, although some donor-acceptor pairs are dominant for S, others for R. The distribution plots show that choosing "MaxLT" as a leading source of MD metrics is misguided. We observe that the distributions of hydrogen-bonding lifetimes over four (because we did all 4 arrangements independently) 200 ns MD simulation runs tend to be better representations of what is going on at the interface, especially when we consider the dynamic nature of chiral recognition process that occurs between the enantiomers and the polymers on the silica.

In the previous chapter using Model 2, we summarized the hydrogen-bonding lifetime observations in a table listing the dominant hydrogen-bonding interactions for enantiomers with a single slightly restrained ADMPC polymer in solution, naming the individual donor-acceptor pairs and stating whether longer lived for R or for S for each donor-acceptor pair. Clearly, the plots shown in Fig. 4.10 and 4.11, and Fig. 4.13 and 4.14 are superior quantitative versions of this type of information, leading to a prediction of which of R or S eluted first. Now, we are able to compare with Table 4.2 in Ref. [132] for the four drug compounds we studied here to see whether Model 2 gave the same result for each donor-acceptor pair as the more complete Model 4 that has several ADMPC polymers on an amorphous silica slab. The prediction of which enantiomer of benzoin elutes first in hep/IPA solvent in Model 2 is the same as that found here. In both models, the $C{=}O_{drug} - HN_{csp}$ is longer-lived for the S enantiomer, as is the $OH_{drug} - O{=}C_{csp}$, and the R is slightly favored for the $O(H)_{drug} - HN_{csp}$. For flavanone in methanol, the $C{=}O_{drug} - HN_{csp}$ pair is dominant for both models, both giving S as having the longer-lived hydrogen bonds. Thus, for both the benzoin enantiomers in hep/IPA, and the flavanone enantiomers in methanol, Model 2 seems to have done as well as the present model.

However, for thalidomide and valsartan, Model 2 does not perform as well as the present Model. Since they have more donor-accpetor pairs for the same atom type, we use the numbering method shown in Fig 3.8 for the following discussions. In the case of thalidomide, Model 2 identifies $NH_{drug} - O{=}C_{csp}$ and $C{=}O1_{drug} - HN_{csp}$ as two donor-acceptor pairs that are dominantly longer lived for S only (negligible for R), while $C{=}O3_{drug} - HN_{csp}$ is dominant and long-lived for R only, and both R and S participate in $C{=}O4_{drug} - HN_{csp}$, longer-lived for R. On the other hand, Model 4 finds, for S enantiomer the pairs $NH_{drug} - O{=}C_{csp}$, $C{=}O1_{drug} - HN_{csp}$, $C{=}O4_{drug} - HN_{csp}$, (just as in Model 2) having the longest lived hydrogen bonds in decreasing order, with $C{=}O2_{drug} - HN_{csp}$ making some contribution. For the R enantiomer, Model 4 finds the 3 most long-lived hydrogen bonds in the order $NH_{drug} - O{=}C_{csp}$, $C{=}O1_{drug} - HN_{csp}$, (both missed by Model 2), followed by $C{=}O4_{drug} - HN_{csp}$, and $C{=}O3_{drug} - HN_{csp}$ (both also found by Model 2). It is quite clear that, having missed two leading contributions to hydrogen bonding partners for the R enantiomer, it would be difficult for Model 2 to arrive at the correct answer that S thalidomide should elutes first in experiments. In the case of thalidomide, a model that includes multiple polymer strands on the amorphous silica surface appears to be necessary ; Model 2 is insufficient.

The case of valsartan is an interesting one. Model 2 does predict that R elutes

Table 4.2. Comparison of various possible metrics (MD quantities) for Model 4 that may be correlated with experimental ratios of residence times for the enantiomers with ADMPC in the solvent system. S/R ratios, for each metric are given. Values less than 1.00 (corresponding to S elutes first) are in red.

Compounds	Solvent	S/R ratio of various quantities						Expt S/R	Expt elutes first	Predict order ?
		Max-F	Max-MaxLT	Max-AvgLT	Avg-F	Avg-MaxLT	Overall-AvgLT			
benzoin	Hep/IPA	1.64	1.15	1.60	1.13	1.78	2.20	1.25 [a]	R [a]	yes
flavanone	Methanol	3.80	1.26	1.84	3.73	1.62	1.79	2.52 [a]	R [d]	yes
thalidomide	Methanol	2.12	1.02	1.58	2.70	0.50	0.59	0.47 [c], 0.35 [d], 0.77 [e]	R [e]	yes from avg
valsartan	Hep/IPA	4.48	0.52	1.79	1.00	1.16	2.00	1.29 [a]	R [a]	yes

[a] Experimental separation factors and elution orders were previously reported in Ref. [132].

[b] α=2.17 for flavanone in methanol, with the (R)-(+) enantiomer eluted as the first peak, from [124].

[c] Ref [127].

[d] α=1.44 for ambucetamide in acetonitrile, α=1.40 for etozoline in acetonitrile, α=2.89 for thalidomide in methanol, from [128].

[e] α=1.30 for thalidomide in methanol, with the (S)-(-) enantiomer eluted as the first peak, from [125].

first, having found S enantiomers forming many long-lived hydrogen bonds in 5 donor-acceptor pairs ; the incidences of R enantiomers forming hydrogen bonds are far fewer, leading to a ratio of S/R orders of magnitude larger than the experimental separation factor of 1.29 reported by us in Ref. [132]. In the case of valsartan, Model 4 does reveal the large number of donor-acceptor pairs involved in hydrogen bonds between enantiomer and ADMPC that Model 2 has found, as well as several others that have not been found by Model 2. Model 4 provides a more complete sampling for both enantiomers, by a factor :

4 strands × (16/10) mers excluding ends × 5 molecules × 4 arrangements × 200/300 ns $\approx$ 85.3

Furthermore, by providing the possibility of the valsartan molecule interacting with more than one strand at the same time, as seen in the examples shown in Fig. 5 (not available in Model 2), and eliminating approaches from all directions around a polymer strand that are possible in Model 2, Model 4 captures the mode of interaction of valsartan with ADMPC on amorphous silica surface in a more realistic way than was impossible with Model 2. For this molecule, this appears to make a big difference ; and we expect this also to be the case with larger drug molecules.

In Table 4.2, we provide the results using the same MD metrics as defined in Eqn.s 3.1 to 3.10. These results are based on a combination of results from the four parallel/antiparallel arrangements in Fig. 4.2 ; the sum of the 4 different arrangements represents parallel and antiparallel grooves equally. The results are more consistent between metrics than Model 2, possibly because of the 85 times as many opportunities for an enantiomer to interact with the polymer in the Model 4 results. It is still true that different metrics give different results, but, at least in the case of benzoin and flavanone, Model 4 provides better consistency across all metrics as to which enantiomer elutes first. This might be due to the fewer number of possible donor-acceptor pairs compared to thalidomide and valsartan ; we believe that the results for the latter could still be improved by longer MD runs. For thalidomide, only the "Avg of MaxLT" and the "Overall Average LT" provide the correct elution order. On the other hand, using Model 2, these two metrics actually give the wrong elution order. In the case of valsartan, the S/R ratios are more reasonable in the Model 4, no longer the 14-4600 found by Model 2. This is due to better statistics in the present model, whereas with Model 2 the R enantiomer had extremely few hydrogen bonding events. Even more important might be the structure of Model 4 being more realistic, providing multiple strands which we observe to be important for valsartan. Finally, the overall average hydrogen-bonding lifetime appears to be the best MD metric.

4.3.4 The Role of Ring-Ring Interactions. Next, we investigated the interactions between the rings on the benzoin enantiomers with the dimethylphenyl group on the ADMPC for various parallel/antiparallel arrangements in the Model 4. The plots for the individual arrangements (aaaa, aabb, abba, abab) are shown in Fig. 4.16. When comparing the plots, we discover that the interaction of benzoin with ADMPC is independent of the parallel/antiparallel arrangements. The sum over all arrangements weighted equally is shown in Fig. 4.15.

The interactions provided by the amorphous silica restrain the polymer chains and retain their configurations relatively. This can be read from Fig. 4.15, with a high probable (γ, θ) distribution in the vicinity of (10°,30°). This angle distribution was explained in the previous chapter used by the Model 1 & 2. The angles have same definitions as described previously. In this sense, Model 4 shows quite similar behavior to Model 2. In both Models 4 and 2, there is an observed preference for average angles in the vicinity of $\gamma = 10°$, $\theta = 30°$ for both rings in benzoin and the ADMPC rings. Furthermore, Fig. 4.15 shows a difference between the ring-ring interaction maps for the S and the R enantiomers. This indicates that the Model

4, where the restraint of the ADMPC is provided by the silica surface, presents a chiral-selective recognition for S and R enantiomers of benzoin. It appears that the nature of this restraint is approximated to some extent by that which we imposed artificially on a single polymer strand in solution in Model 2. We also note that a completely unrestrained free-floating polymer model (Model 1) shows essentially no discrimination between S and R (see Fig. 4.17). We observe differences between the various combinations of parallel and antiparallel arrangements in Fig. 4.16 in the maps of the angles for the individual arrangements (aaaa), (aabb), (abba) and (abab) ; yet all of them exhibit the same highly populated regions $(\gamma,\ \theta)$ = 10-15°, 30-40° for both rings in benzoin and the ADMPC rings. Differences only show up in the less populated regions from one arrangement to another, and distinct differences between S and R are found in every arrangement. There exists a distinction between R and S angle distributions of the orientation of the benzoin rings with the rings of ADMPC in Fig. 4.15, which is a clear indication that, as we have previously noted, the ring-ring interactions play an important role in the chiral discrimination, although not in the form of attractive face-to-face or displaced parallel configurations as originally proposed in static models. Those canonical forms of planar ring-ring orientations are not found in the distribution of angles that are observed in any of the MD simulations. The present results retain those earlier conclusions.

4.3.5 Future Plans for This Project. In this chapter, we successfully developed an improved model to simulate interactions and analyze hydrogen-bond information between ADMPC and drugs. The future plans of this project could involve the following topics :

(a) By utilizing the present model, other potential drugs which confirmed to be separable by using this type of chiral stationary phase can be simulated. Those future tests can be used to enlarge the simulated database.

(b) So far, we only investigated one polymer, ADMPC (Epitomize^{TM} CSP-1A). Other CSP-1 types, which have different substituents on the phenyl groups on the side chain, and CSP-2 types with cellulose backbones, can be simulated using the same procedure presented in this chapter.

(c) Other interesting topics, such as enantiomers with multiple chiral centers, elution order reversal occurring upon changing solvent composition, the length of alkyl tail on chiral drugs affecting elution order and separation factors, can also be investigated using the current model.

(d) d. Throughout this study, one of the most puzzling questions we seem to answer only partially but not completely is : apart from hydrogen-bonding and ring-ring interactions, what else can contribute to the simulated separation factor or elution order ? Other interactions could include hydrophobic forces in addition to ring-ring interactions, for example involving alkyl tails of various lengths on the drug molecule, dipole-dipole interactions beside hydrogen bonding. Such interactive events usually happen frequently but briefly during a simulation. Unless focusing on a particular behavior and analyzing the trajectory for this specific interaction, we may miss analyzing additional features or indicators that could potentially contribute to the chiral separation mechanism. Also, we do not know how to combine quantitatively the hydrogen bonding lifetimes with ring-ring interactions and these other analyses to obtain an MD quantity that is directly proportional to the retention time of an enantiomer. Machine learning (ML) and even deep learning (DL) technology could provide a new approach to this project in the future.

(e) In summary, we believe that, at the final stages of this project, with the help of ML and DL technologies, we could successfully capture all relevant information from MD simulation trajectories, and a data processing model could be generated from the results of MD simulations and experimental HPLC data, with capacity for continuous refinement. More importantly, after gathering enough simulated and experimental HPLC results, we may develop generally applicable rules from our database for predicting a possible set of optimum experimental conditions for a candidate drug molecule, before running either experimental HPLCs or MD simulations.

4.4 Conclusion

We have prepared a physical model that is closer to the real chiral stationary phase system where ADMPC is coated on amorphous silica and is equilibrated in the solvent system. We took special care in approaching the final model of ADMPC on amorphous silica in the solvent system so as to reach the correct polymer structure in the presence of both the amorphous silica and the solvent. The resulting model is a distinct improvement over Model 2 which was a slightly restrained single polymer strand in solution. The new model provides the possibility of an enantiomer interacting simultaneously with two polymer strands on the surface, occurrences that any model using a single polymer strand of any length cannot provide. We have observed such events for valsartan in hep/IPA due to its molecular size. The results show that different parallel and anti-parallel arrangements of the polymer strands retain the conclusions of the sum of the results over all 4 arrangements. The ring-ring interactions for benzoin interacting with Model 4 ADMPC are very similar to what we observed in Model 2, providing a discrimination between S and R enantiomers. While the simpler cases of benzoin and flavanone (few donor-acceptor pairs between enantiomer and ADMPC) did not reveal the weaknesses of Model 2 with respect to the prediction of elution order, thalidomide and valsartan enantiomers were problematic in our earlier work. The present model gives a more complete accounting of the hydrogen bonding lifetimes in various donor-acceptor pairs for thalidomide, thus leading to an unequivocal prediction that S elutes first, whereas Model 2 gave mixed results with various metrics. The present model also provides a more conclusive result that using an overall average of the hydrogen-bonding lifetimes, rather than maximum values of lifetimes for various donor-acceptor pairs gives more consistent results. The case of valsartan is also resolved, leading to not only the correct elution order (R elutes first, just as predicted using Model 2) but a more reasonable value for the S/R ratio which compares favorably with the experimental separation factor. The procedural protocol we have developed can be used with other combinations of chiral stationary phases and solvent systems.

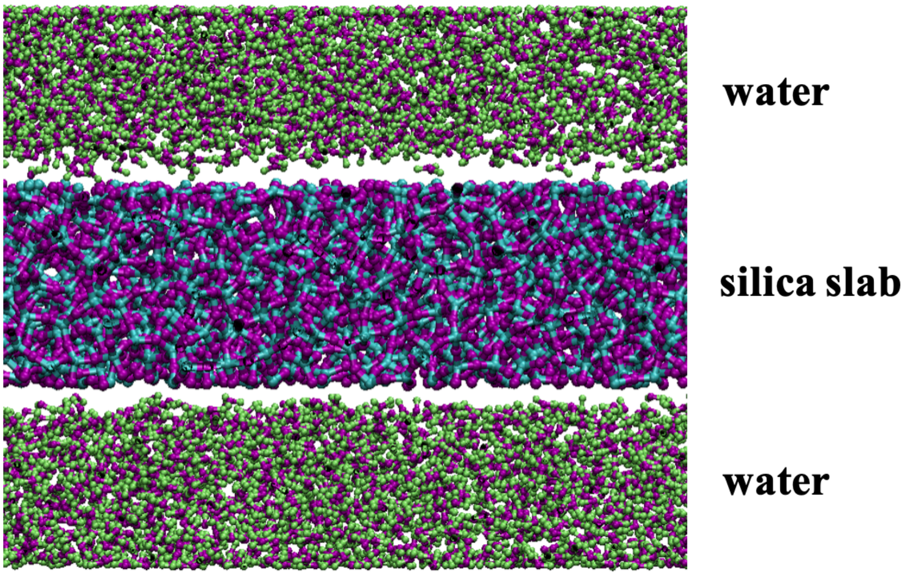

Figure 4.1. System setup for preparation of silanol-capped surface in which the silica slab in the center is exposed to water regions on both sides. Rectangular volumes of water were generated from a pre-equilibrated water box.

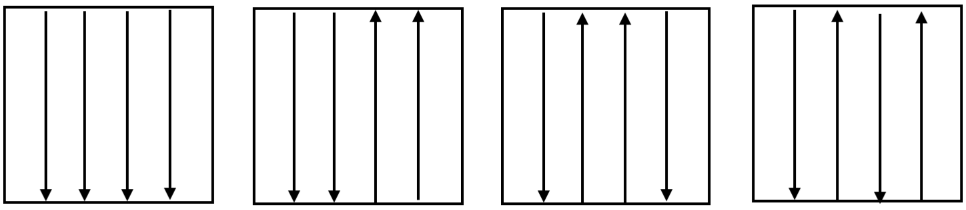

Figure 4.2. Different arrangements of 18-mer ADMPC strands on silica surface : (a) aaaa ; (b) aabb ; (c) abba, (d) abab. Neglecting the edges, each arrangement provides some number of inter-strand grooves arising from parallel and antiparallel strands, respectively (4,0), (2,2), (2,2), (0,4), considering periodic boundary conditions. Taken altogether, they result in an equal number (8) of each.

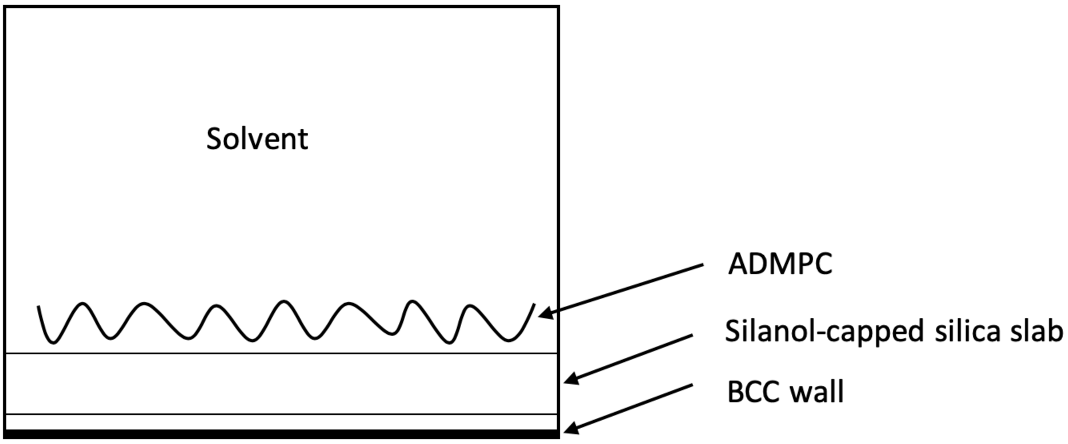

Figure 4.3. System arrangement for equilibrating ADMPCs on the amorphous silica in the solution.

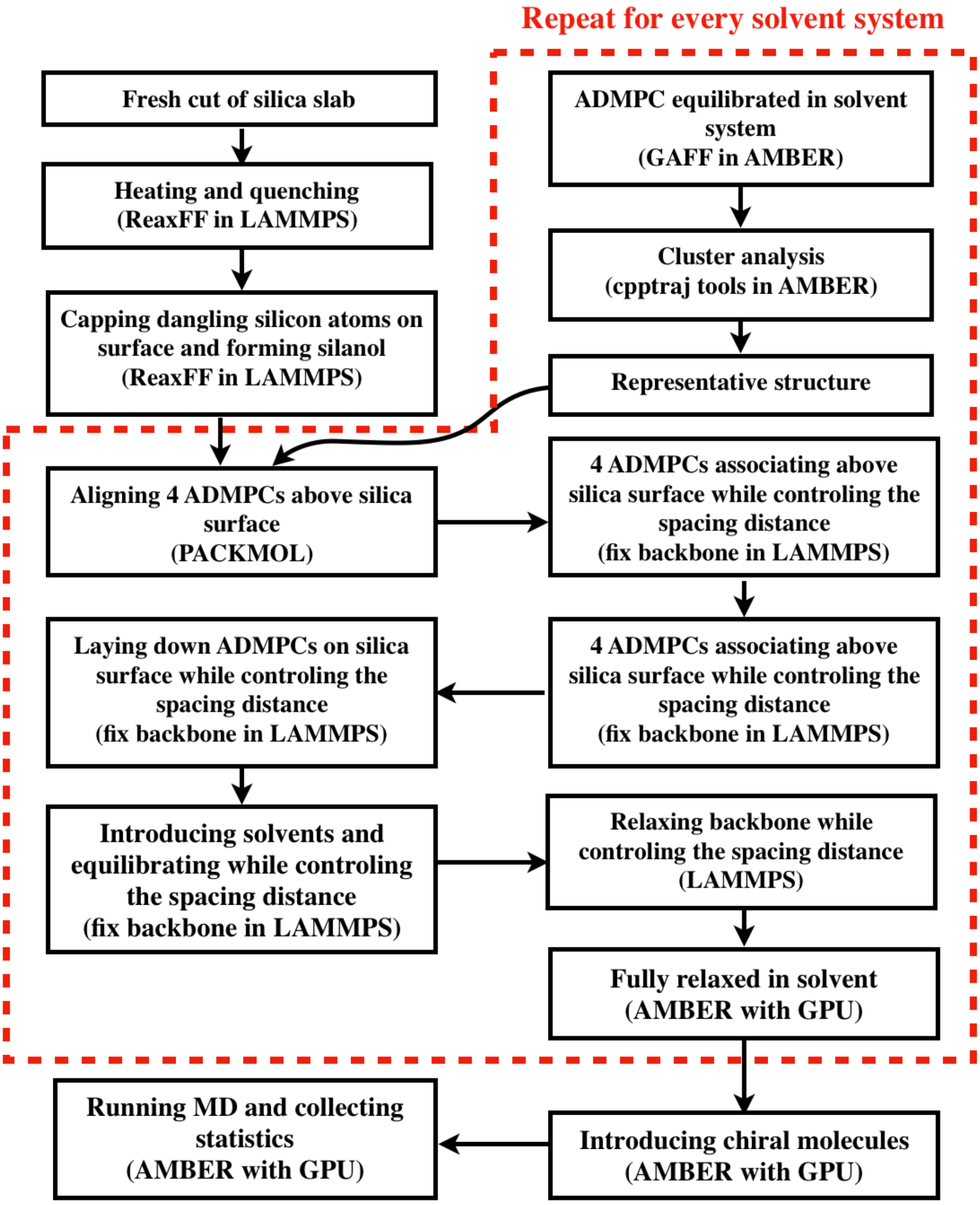

Figure 4.4. Processing flow chart of Model 4 (ADMPCs on silica surface).

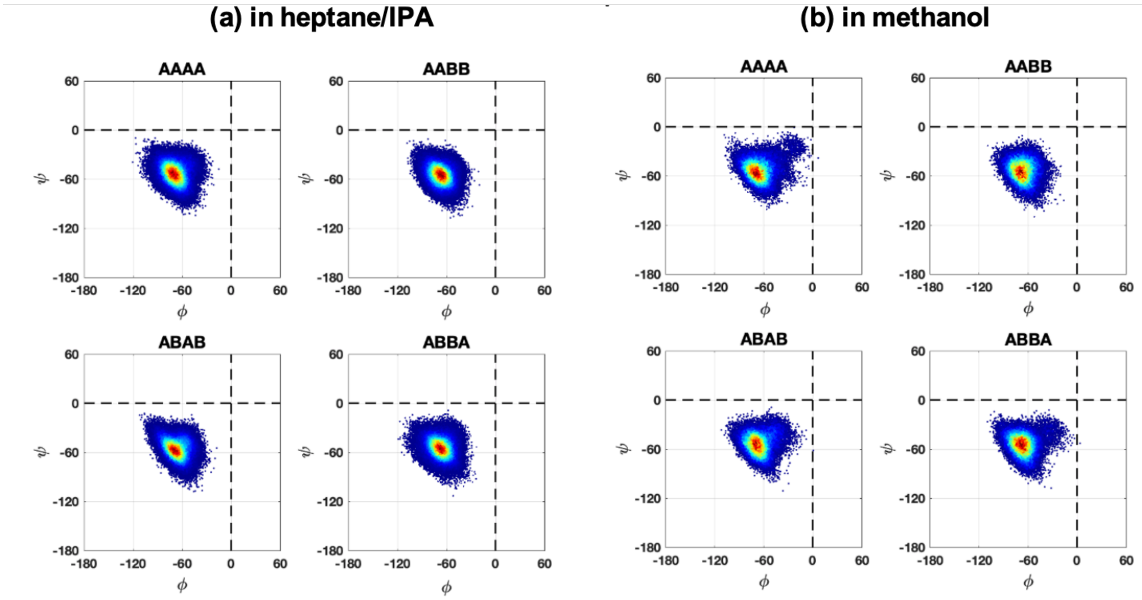

Figure 4.5. Ramachandran maps of dihedral angles of the glycoside bond between adjacent monomers of the four 18-mers of ADMPC on silanol-capped silica (a) in hep/IPA and (b) in methanol, in various parallel/antiparallel arrangements. The colors from blue to red represent the density of the data points going from low to high. Of the four quadrants (Φ, Ψ) = -180° to +180°, we only show the populated quadrant.

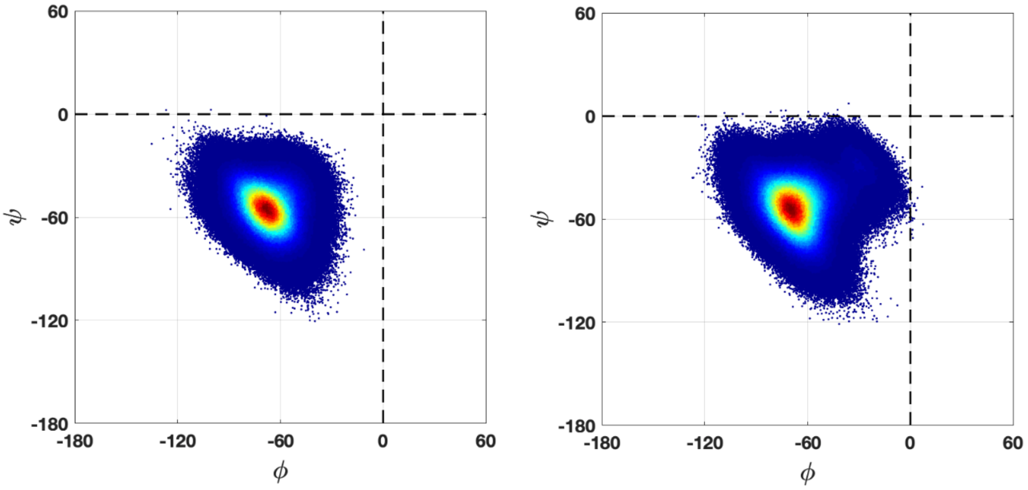

(a) in hep/IPA (90/10)

(b) in methanol

Figure 4.6. Distribution of angles for four strands of ADMPC on silica slab, averaged over various parallel/antiparallel arrangements in (a) hep/IPA and (b) methanol solvent systems after equilibration with no constraints. The colors from blue to red represent the density of the data points going from low to high. Of the four quadrants (Φ, Ψ) = -180° to +180°, we only show the populated quadrant.

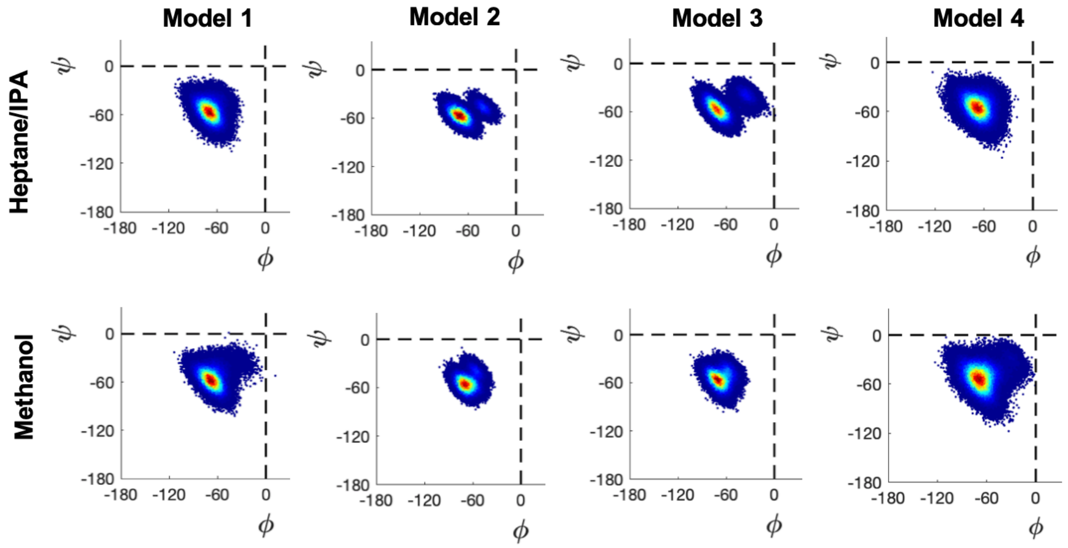

Figure 4.7. Maps of dihedral angles of the glycoside bond between adjacent monomers of the four 18-mers of ADMPC on silanol-capped silica in methanol (or hep/IPA), all arrangements combined, compared with Models 1, 2, and 3. The colors from blue to red represent the density of the data points going from low to high. Of the four quadrants (Φ, Ψ) = -180° to +180°, we only show the populated quadrant.

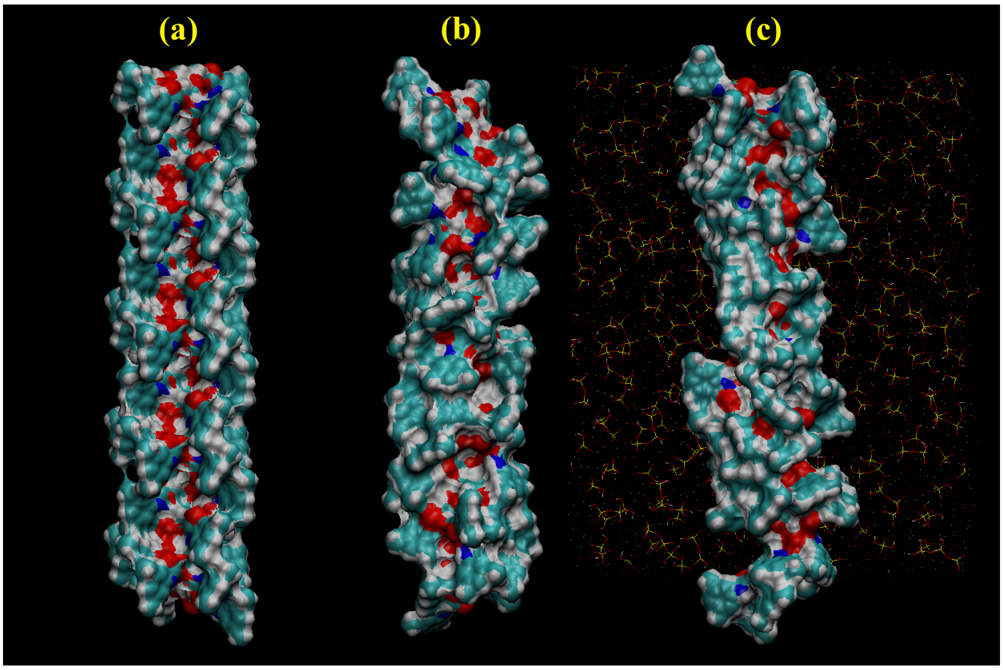

Figure 4.8. The van der Waals surface presented by a polymer chain (a) in the perfect Okamoto structure, (b) for a single snapshot in the polymer chain in solvent hep/IPA, (c) for a single snapshot of one of four chains in parallel (aaaa) arrangement on the silanol-capped silica in the presence of hep/IPA, showing only one chain for clarity.

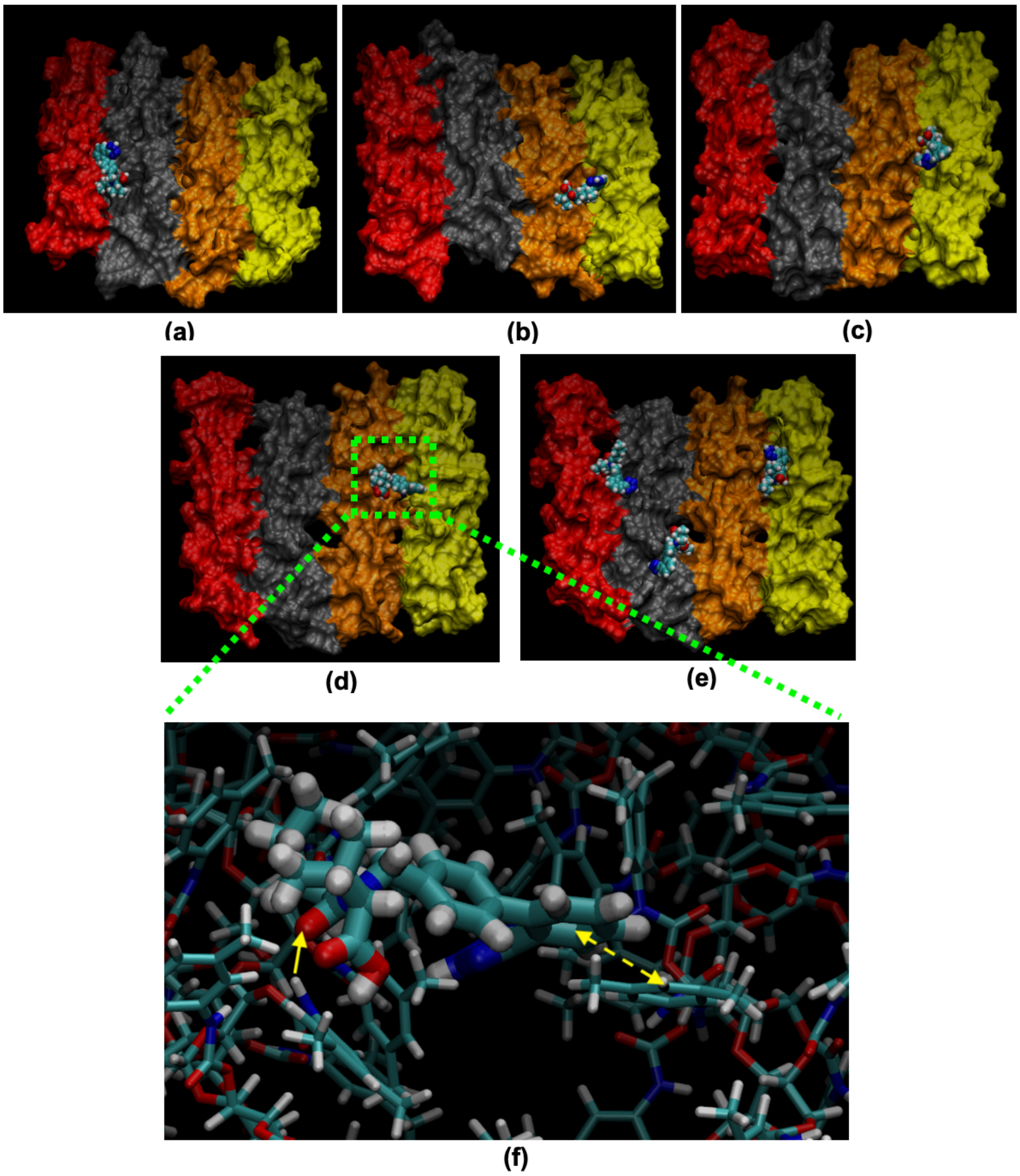

Figure 4.9. Snapshots from MD simulations in which incidences of valsartan interacting with two adjacent polymer strands were observed to persist for several frames. (a) R enantiomer on aaaa arrangement of ADMPC on amorphous silica, (b) S on abab, (c) R on abba, (d) S on aabb, (e) three S enantiomers on aabb, (f) a close-up view of one of the multitude of incidences of valsartan interacting simultaneously with two polymer strands : single-yellow-arrow with solid line identifies a hydrogen bond ; double-yellow-arrow with dashed line indicates a hydrophobic ring-ring interaction.

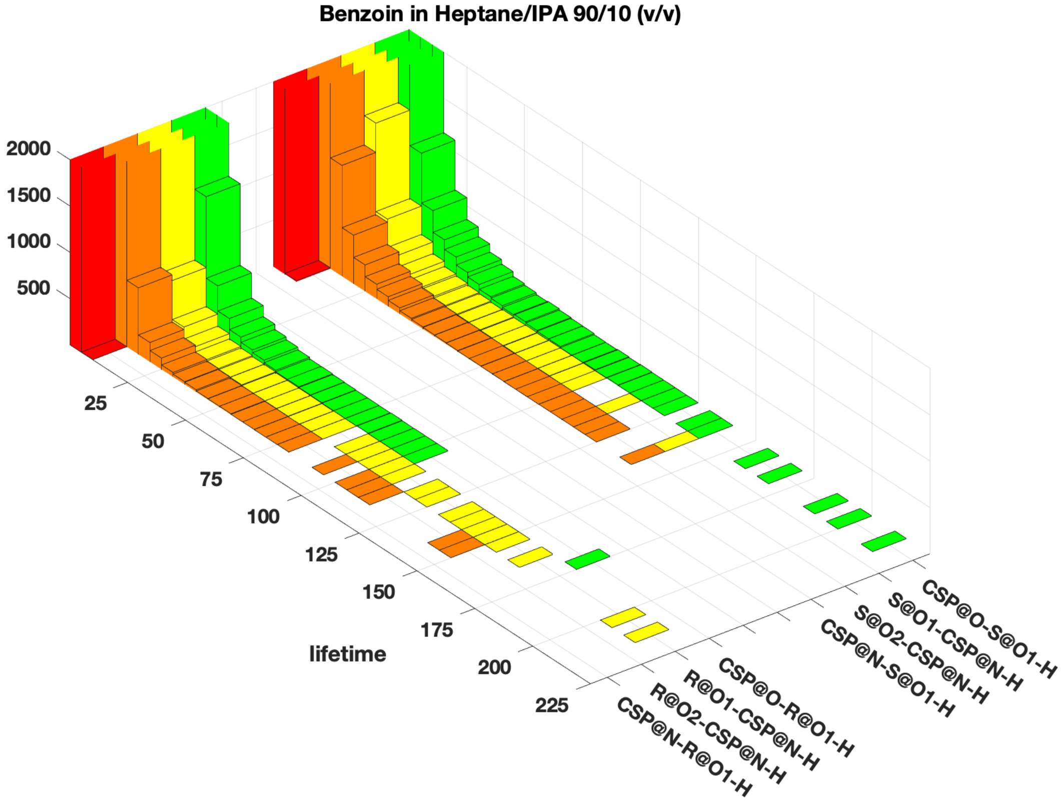

Figure 4.10. Distribution of lifetimes of hydrogen bonds between R or S enantiomers of benzoin and ADMPC on silica in hep/IPA for each of the donor-acceptor pairs : CSP@O and CSP@N denote the acceptor oxygen and nitrogen sites, and CSP@N-H denotes the donor site in the chiral stationary phase ADMPC strands on silica. Likewise, S@O1 and R@O1 denote the acceptor sites while S@O1-H and R@O1-H denote the donor sites on the S and R enantiomers, respectively. These are the sites identified in Fig. 3.8 for benzoin and ADMPC. The y axis counts the number of incidences over the entire trajectory, summed over all four parallel/antiparallel arrangements shown in Fig. 4.2 ; the very high counts for the very short lifetimes are cut off in this display.

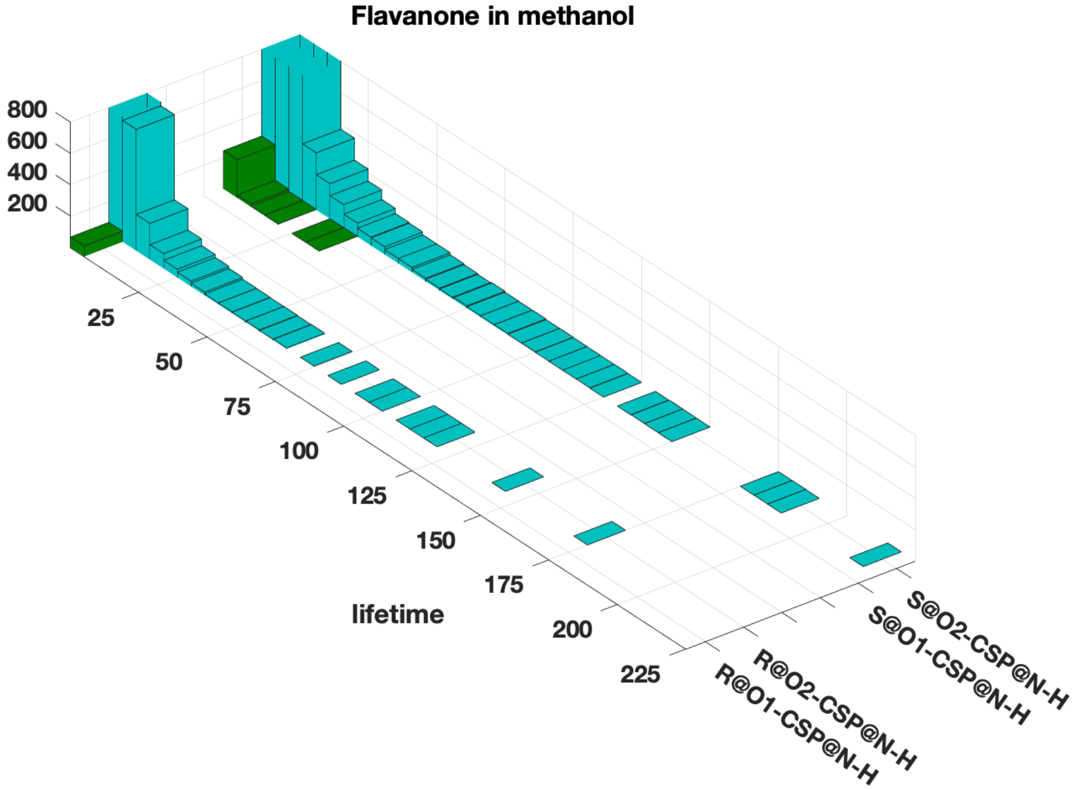

Figure 4.11. Distribution of lifetimes of hydrogen bonds between R or S enantiomers of flavanone and ADMPC on silica in methanol for each of the donor-acceptor pairs : CSP@N-H denotes the donor site in the chiral stationary phase ADMPC strands on silica. S@O1, S@O2 and R@O1, R@O2 denote the acceptor sites on the S and R enantiomers, respectively. These are the sites identified in Fig. 3.8 for flavanone and ADMPC. The y axis counts the number of incidences over the entire trajectory, summed over all four parallel/antiparallel arrangements shown in Fig. 4.2 ; the very high counts for the very short lifetimes are cut off in this display.

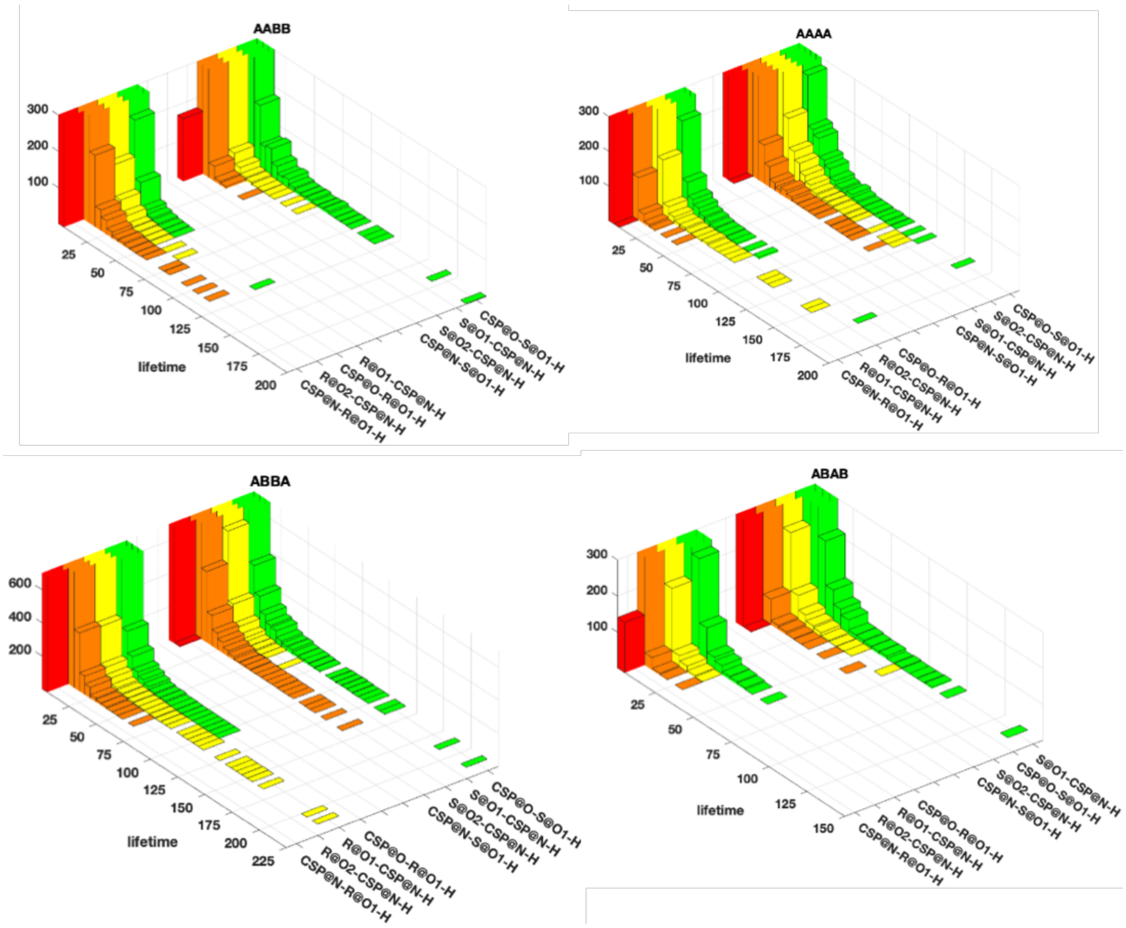

Figure 4.12. Distribution of lifetimes (ps) of hydrogen bonds between S or R enantiomers and ADMPC on silica for) benzoin in hep/IPA for each of the donor-acceptor pairs. CSP@O and CSP@N denote the acceptor oxygen and nitrogen sites, and CSP@N-H denotes the donor site in the chiral stationary phase ADMPC strands on silica. Likewise, S@O1 and R@O1 denote the acceptor sites while S@O1-H and R@O1-H denote the donor sites on the S and R enantiomers, respectively. These are the sites identified in Fig. 3.8 for benzoin and ADMPC. We show the results for various parallel and anti-parallel arrangements of polymer strands on the silica. The y axis counts the number of incidences over the entire trajectory ; the very high counts for the very short lifetimes are cut off in this display.

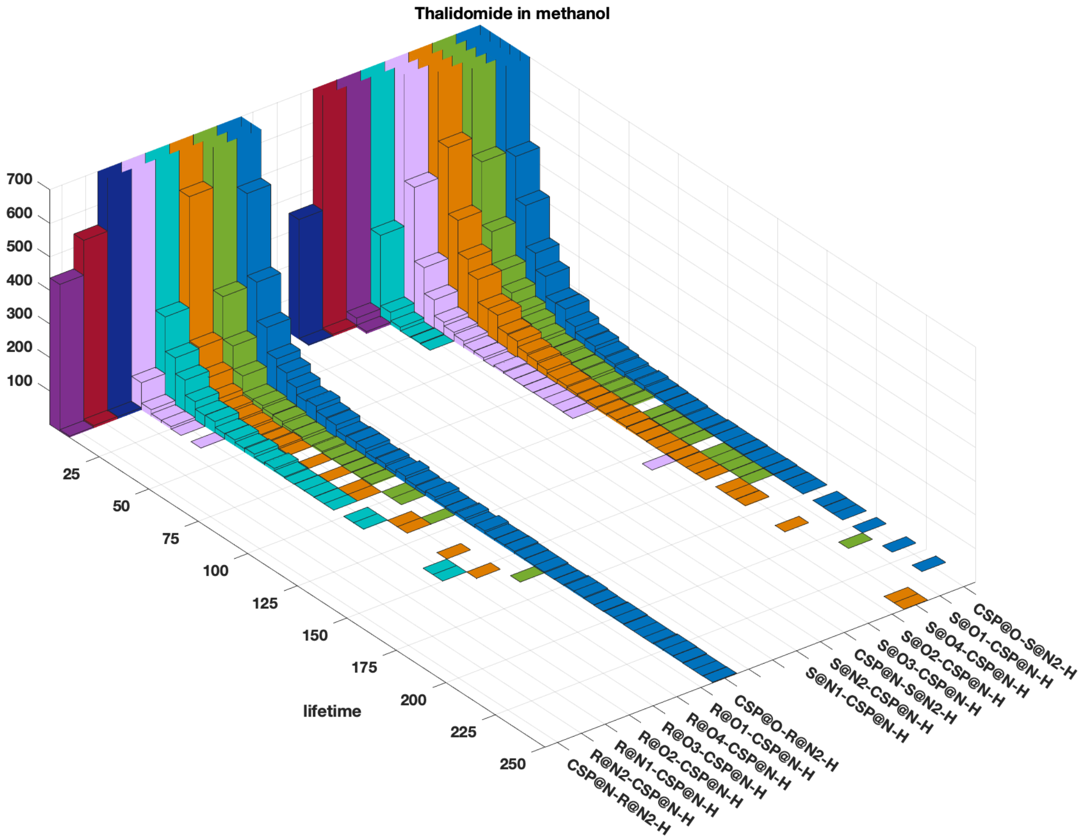

Figure 4.13. Distribution of lifetimes (ps) of hydrogen bonds between S or R enantiomers and ADMPC on silica for thalidomide in methanol. CSP@O and CSP@N denote the acceptor oxygen and nitrogen sites, and CSP@N-H denotes the donor site in the chiral stationary phase ADMPC strands on silica. Likewise, S@O1, S@O2, S@O3, S@O4, S@N1, S@N2, and R@O1, R@O2, R@O3, R@O4, R@N1, R@N2 denote the acceptor sites while S@N2-H and R@N2-H denote the donor sites on the S and R enantiomers, respectively. These are the sites identified in Fig. 3.8 for thalidomide and ADMPC. The y axis counts the number of incidences over the entire trajectory, summed over all four parallel/antiparallel arrangements shown in Fig. 4.2; the very high counts for the very short lifetimes are cut off in this display.

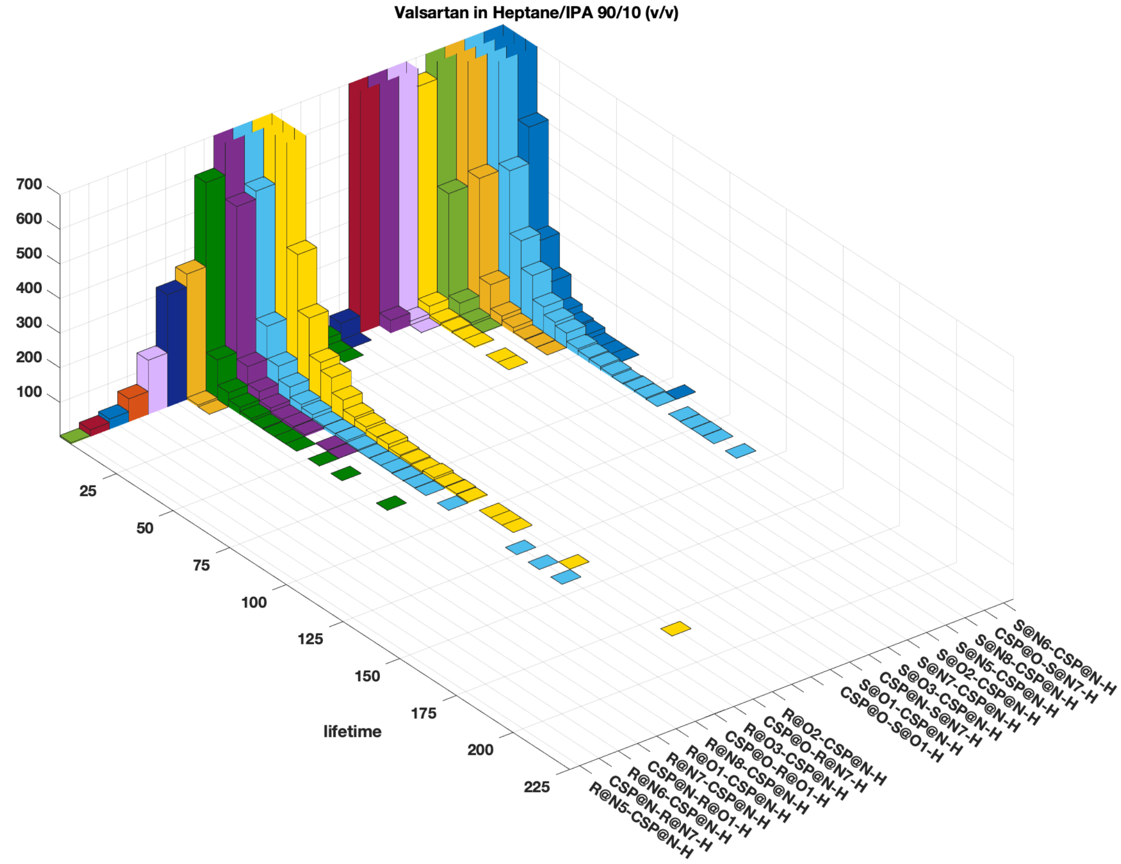
Valsartan in Heptane/IPA 90/10 (v/v)

Figure 4.14. Distribution of lifetimes (ps) of hydrogen bonds between S or R enantiomers and ADMPC on silica for valsartan in hep/IPA. CSP@O and CSP@N denote the acceptor oxygen and nitrogen sites, and CSP@N-H denotes the donor site in the chiral stationary phase ADMPC strands on silica. Likewise, S@O1, S@O2, S@O3, S@N5, S@N6, S@N7, S@N8, and R@O1, R@O2, R@O3, R@N5, R@N6, R@N7, R@N8 denote the acceptor sites while S@O1-H, S@N7-H and R@O1-H, R@N7-H denote the donor sites on the S and R enantiomers, respectively. These are the sites identified in Fig. 3.8 for valsartan and ADMPC. The y axis counts the number of incidences over the entire trajectory, summed over all four parallel/antiparallel arrangements shown in Fig. 4.2 ; the very high counts for the very short lifetimes are cut off in this display.

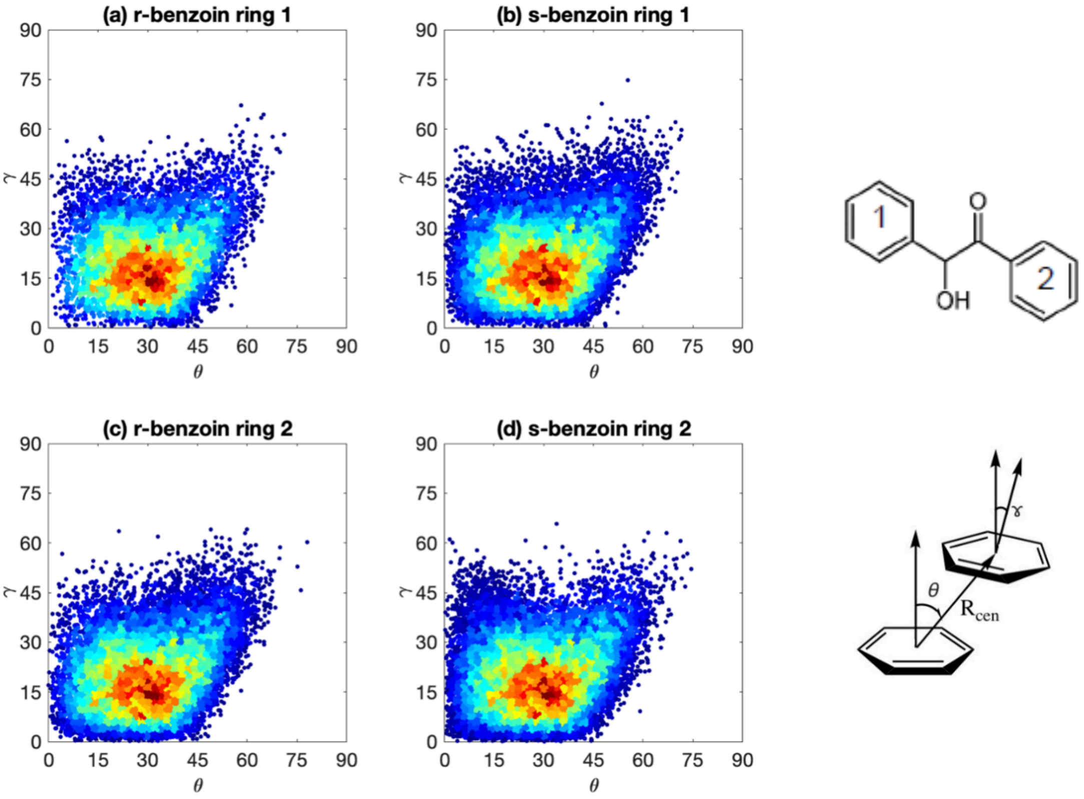

Figure 4.15. Map of the angles describing the distribution of relative orientations of the phenyl rings (γ = vertical axis, θ = horizontal axis), found for distances R_{cen} less than 4.4 Åbetween the center of the phenyl ring#1 and ring#2 of the benzoin molecule and the closest ADMPC phenyl ring, using Model 4 in heptane/isopropanol. The colors from blue to red represent the density of the data points going from low to high. The results are based on snapshots uniformly taken from a 100 ns trajectory, (a) for the R enantiomer (b) for the S enantiomer for ring#1, (c) for the R enantiomer (d) for the S enantiomer for ring#2 for each of the various arrangements.

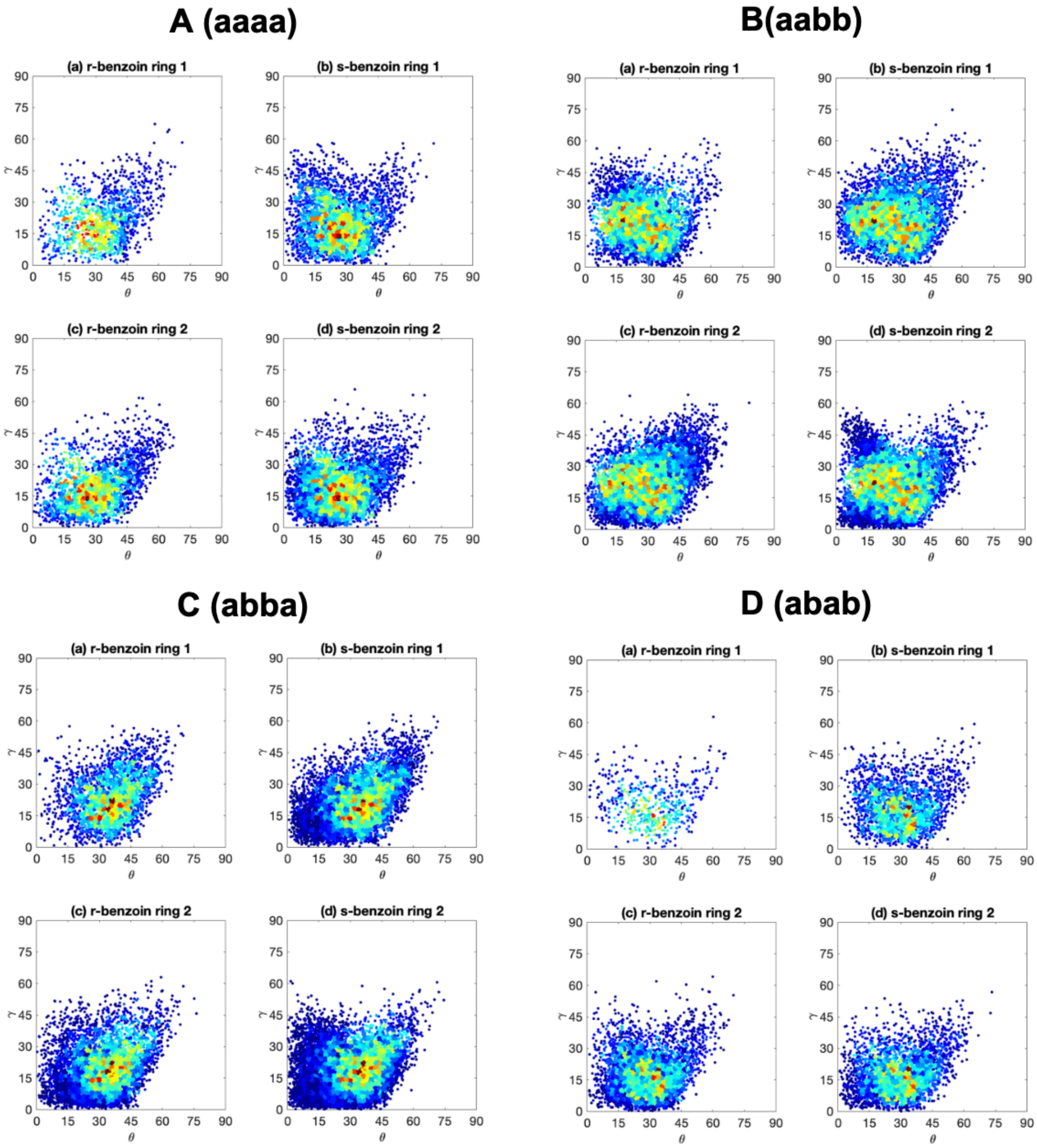

Figure 4.16. Map of the angles describing the distribution of relative orientations of the phenyl rings (γ = vertical axis, θ = horizontal axis), found for distances R_{cen} less than 4.4 Åbetween the center of the phenyl ring#1 and ring#2 of the benzoin molecule and the closest ADMPC phenyl ring, using the present model in hep/IPA. The colors from blue to red represent the density of the data points going from low to high. The results are based on snapshots uniformly taken from a 100 ns trajectory, (a) for the R enantiomer (b) for the S enantiomer for ring#1, (c) for the R enantiomer (d) for the S enantiomer for ring#2. The presentation is the same as for all arrangements shown in Fig. 4.15. Here we show : (A) the (aaaa) arrangement, (B) (aabb) arrangement, (C) the (abba) arrangement, (D) the (abab) arrangement.

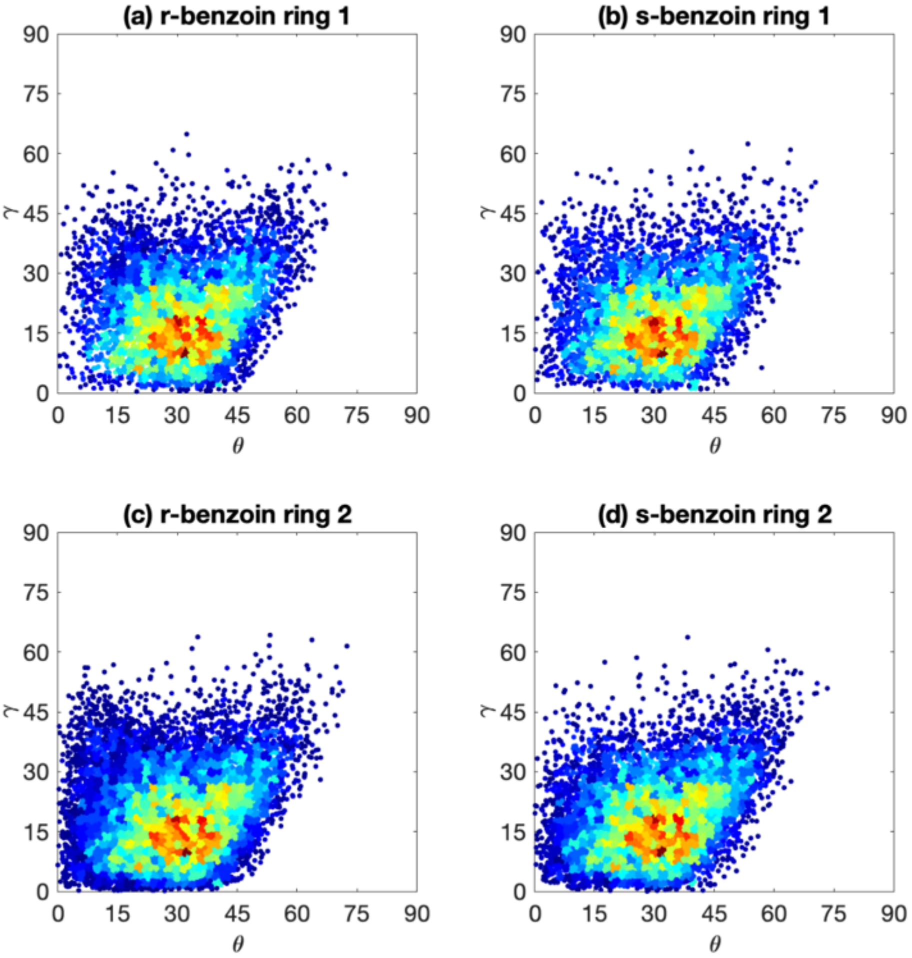

Figure 4.17. Map of the angles describing the distribution of relative orientations of the phenyl rings (γ = vertical axis, θ = horizontal axis), found for distances R_{cen} less than 4.4 Åbetween the center of the phenyl ring#1 and ring#2 of the benzoin molecule and the closest ADMPC phenyl ring, , as in Fig. 4.15, but for a free-floating 12-mer in solution (Model 1). The most probable (γ, θ) angle values are much more spread out than for the ring-ring interactions between benzoin and the ADMPC strands on amorphous silica slab. The plots are almost indistinguishable for the S vs. R enantiomers, an indication of the lower chiral selectivity of the Model 1 ADMPC.

CHAPTER 5

MOLECULAR DYNAMICS SIMULATIONS OF LIQUID-LIQUID PHASE EQUILIBRIUM OF TERNARY METHANOL/ WATER/ HYDROCARBON MIXTURES

5.1 Introduction

Liquid-liquid equilibrium (LLE) plays a vital role in a range of chemical engineering processes, such as liquid-liquid extraction, removal of toxic contaminants from water, and other related separation processes. Extraction is a widely used process in the pharmaceutical industry as an alternate to distillation, since many drugs can lose their potency if subjected to higher temperatures usually encountered in distillation. LLE also has applications in the petroleum industry, where it is used to extract both low molecular weight polar and organic molecules from heavier hydrocarbons. While experimental data is ideally needed for such applications, often because of lack of such data [147], semi-empirical equations of state are used. These methods can sometimes lead to unreliable results. We present in this paper a method to predict such data based on molecular dynamics (MD). Molecular dynamics methods require intermolecular potential models for the constituents of the system. For many molecules, these are now widely available. Another significant advantage of MD [148] is that unless temperature variations are very large, the parameters are largely independent of state conditions. MD methods can therefore be rather useful to predict data for state conditions difficult to study experimentally, especially if the results have been validated at more easily accessible state conditions.

We have investigated a range of ternary systems exhibiting liquid-liquid equilibria. Recently a comprehensive experimental study has been reported on a wide range of such liquid mixtures [149]. To test the validity of our simulation method, we examined three mixtures reported in this study. The three systems investigated have as mixture constituents of water, methanol and a hydrocarbon. The hydrocarbons studied include cyclohexane, n-hexane and 1-heptyne. The studies allowed us to investigate the effect of molecular structure (linear vs. cyclic), while 1-heptyne allowed us to study an asymmetric unsaturated hydrocarbon which is thus polar (the dipole moment of 1-heptyne is 0.86 D).

In our simulations, we have used the parameters in AMBER GAFF library, since those optimized for the types of molecules being investigated in this work, involving mixtures of hydrocarbons, water and methanol. This study is an extension of our previous work on gas solubility [150] [151] [152]. The method developed for gas solubility has not been previously used for LLE, which is the focus of this study. Hydrocarbons are often non-polar or weakly polar molecules. Thus, in general they have low solubility in polar solvents such as water or methanol. In our study, we first wanted to test the applicability of the GAFF force field to LLE simulations by comparing with experimental results. We also then used our simulations to estimate structural and dynamics properties not currently available from experimental studies.

5.2 Simulation System

5.2.1 Computational Details. The simulation system configuration is based on our previous setup used to study gas solubility (liquid-vapor equilibrium). As seen in Fig. 5.1, two impermeable membranes confine the system in the x-direction which effectively makes the simulation system non-periodic in the x-direction. This confinement makes the analysis of the two phases simpler, since otherwise the two liquid phases would drift in the x-direction making it more difficult to determine the compositions of the two liquid phases in a dynamic simulation. The membrane is a single layer FCC wall composed of argon atoms. All the membrane atoms are self-tethered to their initial positions, with inter-atomistic distance, designed to make the wall impermeable to both the solvent and hydrocarbon molecules.

The simulation system has a central organic phase and two aqueous phases around it. We found that equilibrium was achieved more efficiently in such a system (since there are two surfaces available for molecular exchanges between the two phases) compared to a single organic phase in contact with one aqueous phase. The simulation system consisted of 400 membrane atoms (200 per membrane) and 1000 liquid molecules (400 in organic phase and 300 in the two aqueous phases). The system volume was determined by the density of the two phases.

We used the all-atom GAFF force field developed by Wang et al. [11] to represent the potential models as represented by Eq. 1.5. The first three terms refer to the intramolecular energy terms representing forces associated with bonds, bond angles and dihedral angles, while the last two terms are associated with intermolecular energy (dispersion and coulombic).We used the Lennard-Jones (LJ) 12-6 potential model for short-range site-site interactions. A particle-particle particle-mesh solver (PPPM) [153] is used to compute long-range electrostatic forces and energies, which we found computationally more efficient, but equally reliable compared to traditional Ewald technique [57] often used in AMBER or CHARMM. For water we used the TIP3P model [11].

Each simulation was carried out for 30 million femtoseconds (30 ns) and the results were analyzed using three running averaged samples (viz. 15 to 20, 20 to 25 and 25 to 30 million time step) both to ensure that equilibrium had been achieved and to estimate the accuracy of our measurements (error bars).

The open source software package Packmol [120] was used to construct the initial non-overlapping liquid-like random molecular configurations. This significantly assisted the system in reaching its final equilibrium state more efficiently. All simulations used the LAMMPS simulation package [61]. Energy minimization was performed using the Polak-Ribiere [62] conjugate-gradient method and the Verlet algorithm [63] was used to carry out time integrations. A Gaussian thermostat was applied in the NVE ensemble in order to maintain a constant system temperature throughout the simulation. A time step of 1.00 fs was used for runs of 30.0 ns in length. Our simulations had to be carried out in the NVE ensemble because in our methodology we included membranes. If membranes were allowed to move, as they would in the NPT ensemble, then it would make it difficult for us to stabilize the system near the membrane boundaries. In addition, the strategy we used for calculating compositions also required the phase boundaries to be fixed and not variable. The potential models we used in this study were specifically designed for VLE studies so we believe they would provide realistic pressures for such systems. In actual experiments, in general, pressure changes are also accompanied by temperature changes. In our simulations, we kept the temperature constant, so we do not believe any small errors in pressure would result in any measurable changes in phase equilibrium results.

Fig. 5.2 shows a typical density distribution observed in our simulation. For systems that are not homogenous such as ours, estimation of the composition of each phase does present a few challenges. To address this issue, we used the following scheme. For the organic phase, we identified the two valleys in the density profile of the organic phase and then connected them with a straight horizontal line as shown in Fig. 5.2 in red. The region above this line was then, for the purpose of our composition analysis, defined as our organic phase. For the inorganic phase which is contact with two membranes that confine it, we excluded the adsorbed layer adjacent to the two membranes. This was defined to be the first two adsorption peaks in the observed density profile. The region in between these two regions was then defined as the aqueous phase for our composition analysis. The two phases, as defined here, thus vary in size from 135 to 160 Å for the organic phase, and 60-80 Å for the aqueous phase.

When estimating the radial distribution functions, or mean squared displacements (to estimate the diffusion coefficients), for the calculation of compositions, we only sampled molecules while they were in the phases as defined above. This ensured that end/wall effects did not contribute to the reported values, or their movement from one phase to another.

5.2.2 Some Thoughts on Designing the System. As seen in Fig. 5.1, we have a long but thin and narrow simulation box. A regular rectangular box would make the system very large and thus results in expensive computational cost and difficulty to achieve equilibria. Also, such a regular box will increase the contact area between oil and aqueous phases. More molecules in the interfacial region means fewer molecules will remain in the bulk phase. Then, this also means bulk phase composition will not be statistically stable. Although such long and thin box will cause scatter in the bulk density profile, this will be solved by running averages over a longer span of simulation time.

The application of a FCC wall confining the system is also important and necessary in this study. The density profile is the output we sample throughout the simulation, so we want the entire collection of atoms to be static and not drifting because of small random perturbations in MD calculations. Since the two FCC wall atoms are self-tethered to their initial position, they can stop the whole liquid phase from drifting. The introduction of such a FCC wall may induce adsorption layer between the solid wall and the liquid phase, which will lead to fewer molecules remaining in the bulk liquid phase. So the thin and narrow system discussed above is also necessary in this case, since it will reduce the contact area and minimize the adsorption effect at the walls.

5.3 Results and Analysis

5.3.1 Ternary Phase Compositions. Tables 5.1, 5.2, 5.3 [154] [155] [156] show the calculated results using the method discussed above from the molecular dynamics simulations. For each system, we simulated three compositions to ensure the suitability of the method for a range of compositions. For each composition, we obtained the reported results from three running averages. These averages were obtained from the simulations between 15 and 20, 20 to 25 and 25 to 30 million time steps. The three sets of data so obtained were then averaged both to ensure that we have reached equilibrium and to estimate the precision (error bars) of our results. Our results only showed rather small variations between these three sets of results, which led us to believe that 30-ns simulations were long enough to approach equilibrium. In our simulations to overcome the possibility of local equilibrium we periodically did stop the simulation and cleared the current velocities of the individual molecules, and replaced them with a new set of generated Gaussian velocities corresponding to the system temperature. This we believe would overcome local equilibrium issues. In a molecular simulation study of the type reported here, we are simulating a limited number of molecules because of computational constraints (in our case - 1000 molecules). For very low concentrations the number of molecules of that specie becomes rather small, which would lead to large statistical uncertainties. It was therefore not possible for us to study the lowest concentration studied experimentally where the mole-fraction is low.

Fig. 5.3, 5.4, 5.5 also show our simulation results compared to experimental data in ternary phase diagrams. From the tables and the figures, we observe that our models do very well when compared to experimental data in both the organic and aqueous phases.

Our phase equilibrium results indicate that the potential models used by us

Table 5.1. Compositions of coexisting phases c-hexane/methanol/water at T = 303 K

		Aqueous Phase			Organic Phase	
		Methanol	Cyclohexane	Water	Methanol	Cyclohexane
Series 1	Simulation	0.6034	0.0069	0.3517	0.0245	0.9644
	Error Bar	0.0026	0.0025	0.0048	0.0183	0.0019
	Experiment	0.637	0.0095	0.354	0.0261	0.947
Series 2	Simulation	0.7298	0.0313	0.2130	0.0593	0.9392
	Error Bar	0.0114	0.0113	0.0096	0.0088	0.0096
	Experiment	0.758	0.0298	0.213	0.0476	0.951
Series 3	Simulation	0.8157	0.1843	0.000	0.2353	0.7647
	Error Bar	0.0126	0.0126	—	0.0028	0.0028
	Experiment	0.806	0.1944	0.000	0.2359	0.764

to well-represent these mixtures in both phases. We therefore used these models to predict other properties of interest not currently available from experiments. One property of significant interest is the diffusion coefficient which is closely related to the mean squared displacement. Fig. 5.6 shows results from our simulations for the mean squared displacement (MSD) of methanol in the aqueous phase. Our results show that with decreasing water concentrations in the aqueous phase, the methanol molecules moved slower, which resulted in lower diffusion rates. To understand this behavior better we examined how methanol molecules were networked with other molecules in their immediate vicinity, as the composition of the solution changed. One possibility we investigated was whether the methanol cluster size varied significantly with water concentration, since larger clusters would in general result in slower diffusion. However, by examining the coordination numbers, we observed that the cluster sizes did not in fact change significantly at lower water concentrations. We then focused our attention on cyclohexane. Fig. 5.7 shows snapshots for two solutions included in

Table 5.2. Compositions of coexisting phases 1-heptyne/methanol/water at T = 298 K

		Aqueous Phase			Organic Phase	
		Methanol	1-heptyne	Water	Methanol	1-heptyne
Series 1	Simulation	0.6834	0.0737	0.2429	0.2909	0.6817
	Error Bar	0.0023	0.0168	0.0145	0.0091	0.0125
	Experiment	0.674	0.104	0.222	0.280	0.685
Series 2	Simulation	0.631	0.2354	0.1325	0.3609	0.5818
	Error Bar	0.0107	0.0148	0.0255	0.0060	0.0074
	Experiment	0.650	0.210	0.140	0.360	0.585
Series 3	Simulation	0.6300	0.0486	0.3214	0.1801	0.8066
	Error Bar	0.0068	0.0130	0.0062	0.0007	0.0011
	Experiment	0.643	0.039	0.318	0.190	0.790

Fig. 5.6 ($x_{\mathrm{H_2O}} = 0.0$ and $x_{\mathrm{H_2O}} = 0.213$). From the figures, it can be seen that it is in fact cyclohexane that is the main cause of this change. In the case of $x_{\mathrm{H_2O}} = 0.213$, cyclohexane ($x = 0.029$) seems to be fairly dispersed and is not a barrier for methanol mobility, while at $x_{\mathrm{H_2O}} = 0.0$, it is forming a connected network that would reduce the effective mobility of methanol significantly as observed in the MSD plots. It is also instructive to note the self-diffusion coefficient of pure methanol is twice that of pure cyclohexane at 298 K (we believe that this can be attributed to the higher molecular weight of cyclohexane molecules), and our values also seem to drop by roughly a factor of 2 [157]. To further illustrate this point, we calculated the effective coordination number of cyclohexane molecules around a methanol molecule at the three compositions analyzed (Fig. 5.8). The behavior at ($x_{\mathrm{H_2O}} = 0.354$ and$x_{\mathrm{H_2O}} = 0.213$ is quite similar as was the case with the MSD. At$x_{\mathrm{H_2O}} = 0.0$, once again we see a dramatic difference in the coordination number of cyclohexane around methanol; the cyclohexane molecules in the vicinity of methanol molecules greatly reduce their

Table 5.3. Compositions of coexisting phases n-hexane/methanol/water at T = 298 K

		Aqueous Phase			Organic Phase	
		Methanol	Hexane	Water	Methanol	Hexane
Series 1	Simulation	0.8222	0.0295	0.1215	0.0825	0.9079
	Error Bar	0.0052	0.0090	0.0013	0.0055	0.0055
	Experiment	0.8427	0.0368	0.1205	0.0552	0.9321
Series 2	Simulation	0.7230	0.0327	0.1937	0.0401	0.9567
	Error Bar	0.0151	0.0091	0.0064	0.0081	0.0099
	Experiment	0.7727	0.0217	0.2056	0.0612	0.9226
Series 3	Simulation	0.6670	0.0133	0.2820	0.0372	0.9606
	Error Bar	0.0058	0.0070	0.0048	0.0040	0.0048
	Experiment	0.7022	0.0105	0.2873	0.0240	0.9636

mobility.

To further understand the structural behavior of the solutions investigated we examined the two-body distribution functions. Figs. 5.9 and 5.10 present the distribution functions for methanol-methanol and methanol-water in the aqueous phase. In Fig. 5.9, our results show distinct changes in behavior as the composition changes. The distribution functions are most structured when no water is present. This could have been expected since in the absence of water, cyclohexane could dissolve in the methanol-rich phase more readily (it is more soluble in methanol than in water) and methanol is also attracted to other methanol molecules rather than cyclohexane which is non-polar. As water is introduced into the aqueous phase we observe less structure and more dispersed behavior, since water now competes with methanol. In fact, recent studies have shown that methanol has stronger intermolecular interactions with water molecules than with methanol molecules [158] and our investigations on hydrogen bonds (see following discussion) also confirms this trend. Fig. 5.10 shows the pair distribution function for methanol-water in the aqueous phase. We observe more structure in the solution as the water concentration increases. One reason for the increased structure, as evidenced by a significantly higher first peak would be the increased number of water molecules present (per methanol molecule). However, this would result in perhaps a two-fold increase in the peak by a material balance alone. The higher peak of water molecules around methanol can again be attributed to the stronger interaction of methanol with water molecules, compared to that with other methanol molecules.

In Figs. 5.11 and 5.12 we show the two-body distribution functions for cyclohexane/methanol and cyclohexane/water in the aqueous phase. From Fig. 5.11, it appears that when no water is present in the system, methanol is more uniformly dispersed around cyclohexane molecules. This is essentially because methanol which is polar, is not strongly attracted to cyclohexane (we would like to point out that cyclohexane is more soluble in methanol than in water [158]). Once water is introduced, methanol appears to be more structured around cyclohexane. This is mostly due to the fact that now water which is more polar, is pushed away from cyclohexane, and this makes methanol a more attractive alternative for cyclohexane molecules. Fig. 5.12 shows similar behavior for the cyclohexane/water distribution function. There is more structure observed as the water concentration increases. Of course, one reason for this is the increased number of water molecules present per cyclohexane molecule (35 water molecules per cyclohexane at $x_{\mathrm{H_2O}} = 0.354$ as opposed to about 7 at $x_{\mathrm{H_2O}} = 0.213$). In addition, cyclohexane molecules have a preference for methanol molecules, so water is less structured around cyclohexane when there is a greater availability of methanol molecules.

Fig. 5.13 shows the pair distribution functions for methanol-cyclohexane in the organic phase for the various compositions of cyclohexane investigated in our studies. With increased concentrations of cyclohexane, the distribution functions becomes more structured. This is understandable because it leads to more cyclohexane molecules per methanol molecule. At these higher cyclohexane concentrations, methanol concentrations are rather low which results in smaller clusters of methanol being formed which are then surrounded by more cyclohexane molecules, thus resulting in the more structured behavior observed.

Finally, we investigated the number of hydrogen bonds formed in the aqueous phase per methanol molecule. The hydrogen bonds were defined as distances less than the half the LJ sigma of oxygen and hydrogen plus 0.5 Å, which for our parameter set is 2.2 Å ; and angles being larger than 100°.The results for the three compositions of the aqueous phase are shown in Fig 5.14 and 5.15. It can be seen that once again there is a dramatic drop in the number of hydrogen bonds when no water is present. This results from two factors. First the composition of available molecules for hydrogen bonding (water and methanol) varies from 0.806 (when no water is present) to 0.971 (when $x_{\text{methanol}} = 0.758$) and 0.991 (when $x_{\text{methanol}} = 0.637$). if this was the only factor, clearly the number of hydrogen bonds would increase by approximately 25% when water is present. The results indicate an increase of a factor of 2. This is because methanol is more likely to form more hydrogen bonds with water molecules rather than with methanol molecules. Water has three available sites for hydrogen bonds while methanol has only two such sites. This has also been reported in another recent study [159]. This observation is also confirmed if we examine the hydrogen bond energy per methanol molecule shown in Fig. 5.15. The energy is highest for the case with no water, and lowest for the case with most water.

5.4 Conclusion

Our studies have demonstrated that molecular dynamics simulations are an effective tool to study LLE in mixtures involving both polar and non-polar components.

In addition the intermolecular potential parameters developed primarily from VLE data appears to be effective to predict LLE data as well. Our simulations also confirmed previous studies that indicated that methanol has stronger interactions with water molecules compared to other methanol molecules. We found this difference in intermolecular interactions to strongly influence the structural and dynamic behavior of the mixtures we investigated. In addition, while methanol and water are both highly polar, the differences in their polarity appears to have a significant effect on the properties of such mixtures. In general, an increase in water concentration made the solutions more structured (as demonstrated by the pair distribution functions) and also increased the diffusion rate of the dominant mixture component methanol.

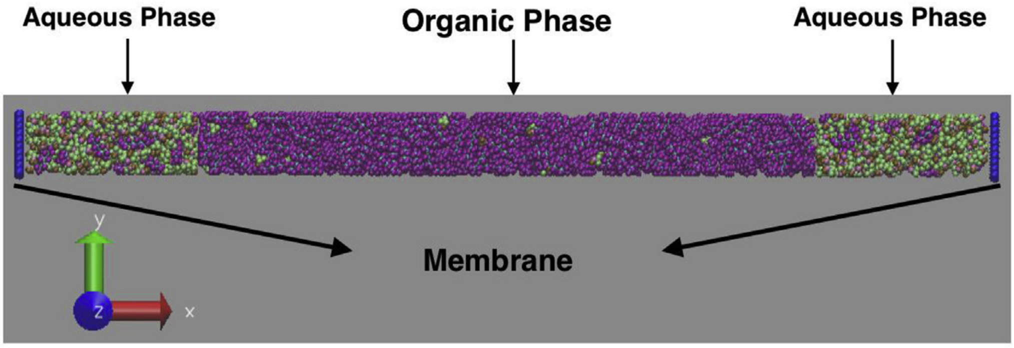

Figure 5.1. System schematic showing aqueous/organic phases.

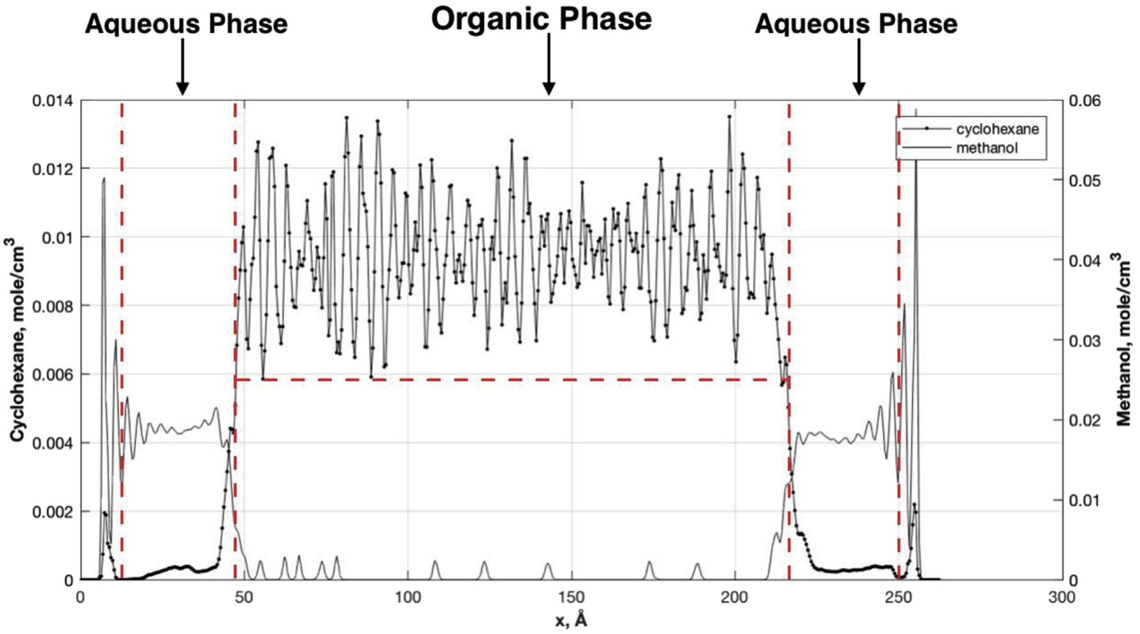

Figure 5.2. A typical density profile used to calculate mole fractions of each component in each phase.

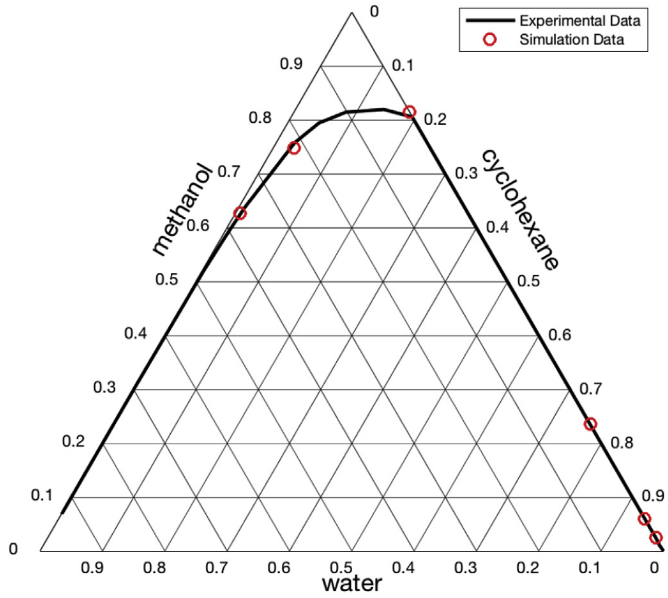

Figure 5.3. Ternary phase diagram of cyclohexane-methanol-water (The experimental data points have been connected to guide the eye.)

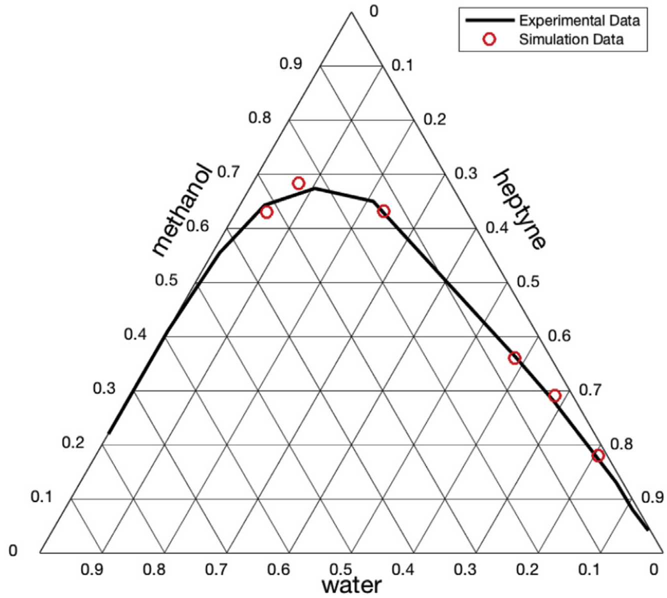

Figure 5.4. Ternary phase diagram of 1-heptyne-methanol-water (The experimental data points have been connected to guide the eye.)

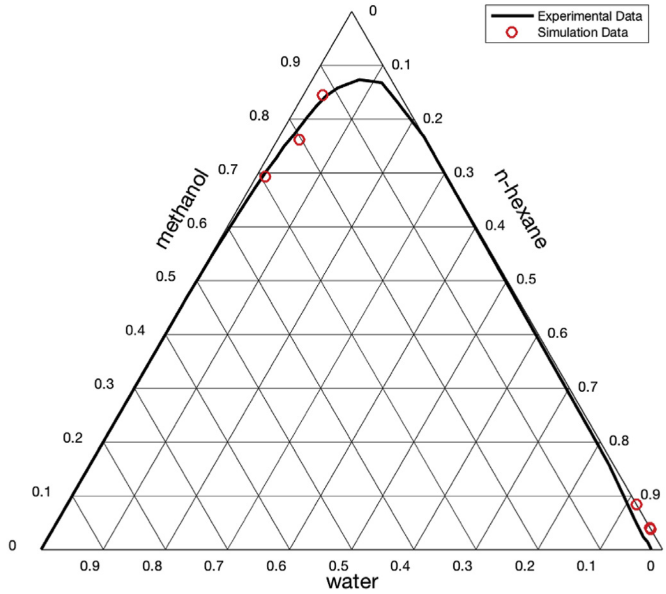

Figure 5.5. Ternary phase diagram of hexane-methanol-water (The experimental data points have been connected to guide the eye.)

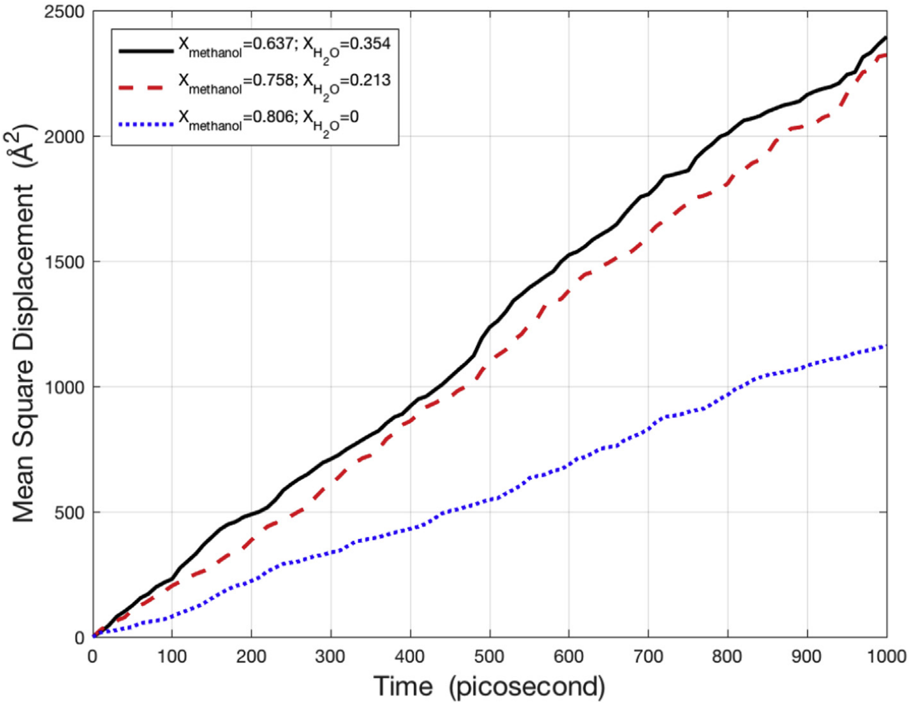

Figure 5.6. MSD of methanol in the aqueous phase for the methanol-cyclohexane-water system

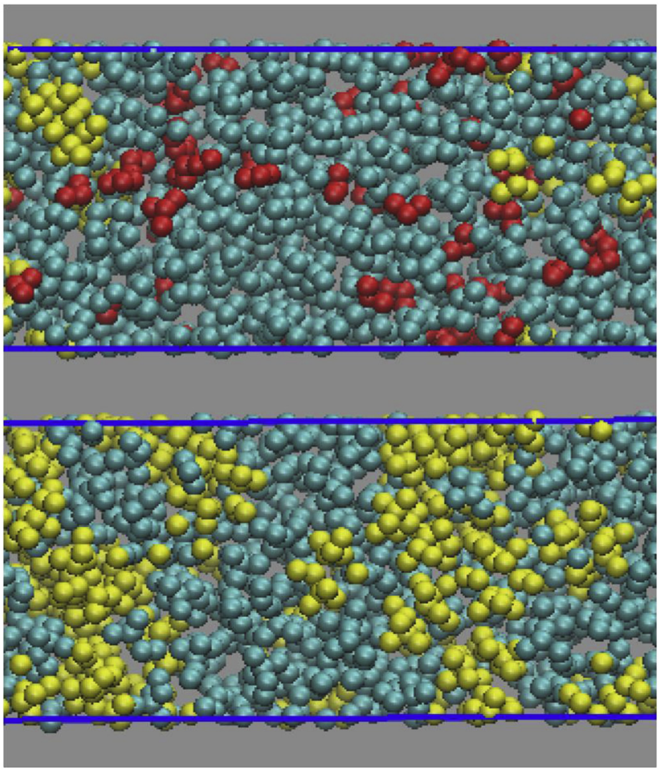

Figure 5.7. Snapshots of Aqueous phases Top : $x_{\mathrm{methanol}} = 0.758$; $x_{\mathrm{cyclohexane}} = 0.029$ Bottom : $x_{\mathrm{methanol}} = 0.806$; $x_{\mathrm{cyclohexane}} = 0.194$ (yellow :cyclohexane, red : water, blue : methanol)

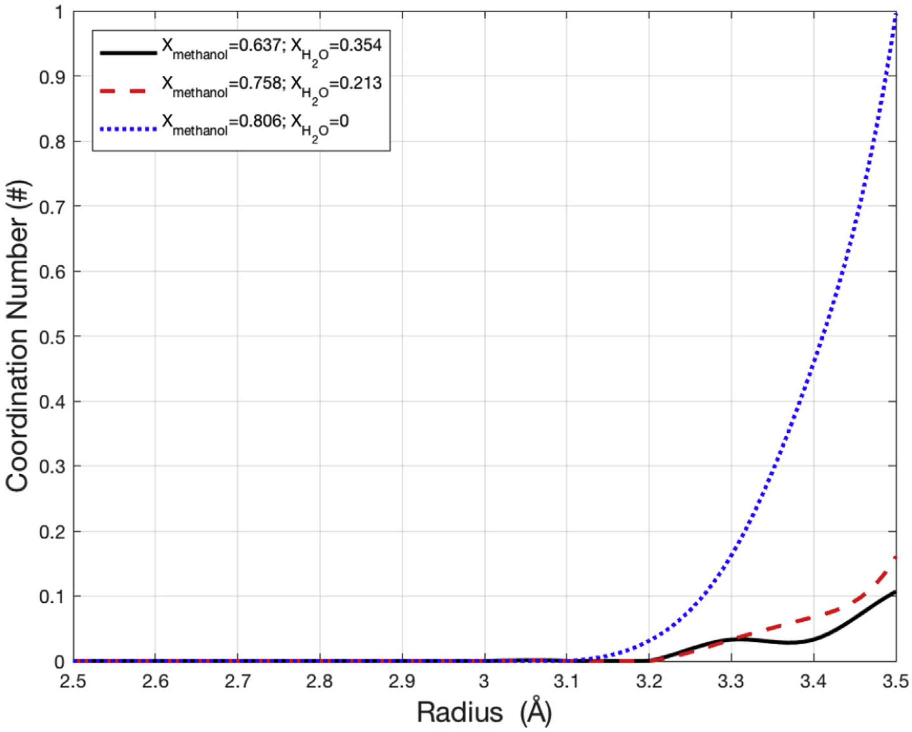

Figure 5.8. Coordination number of methanol-cyclohexane $(CH_2)_6$ clusters for different compositions of the aqueous phase in the methanol-cyclo// hexane-water system.

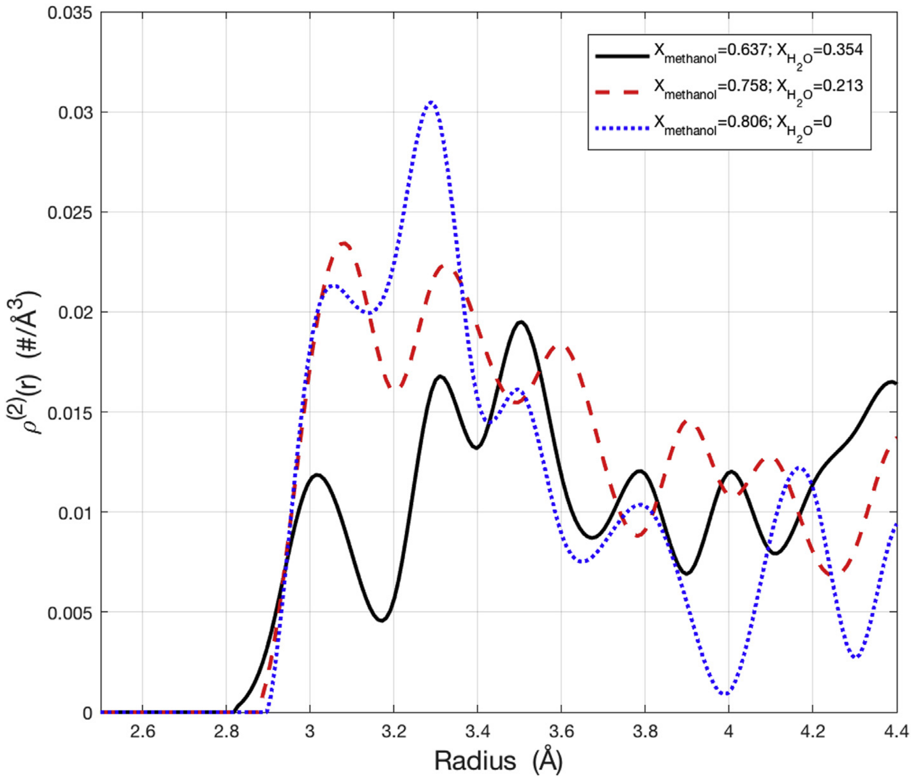

Figure 5.9. Methanol-methanol density distribution function at various composition of the aqueous phase.

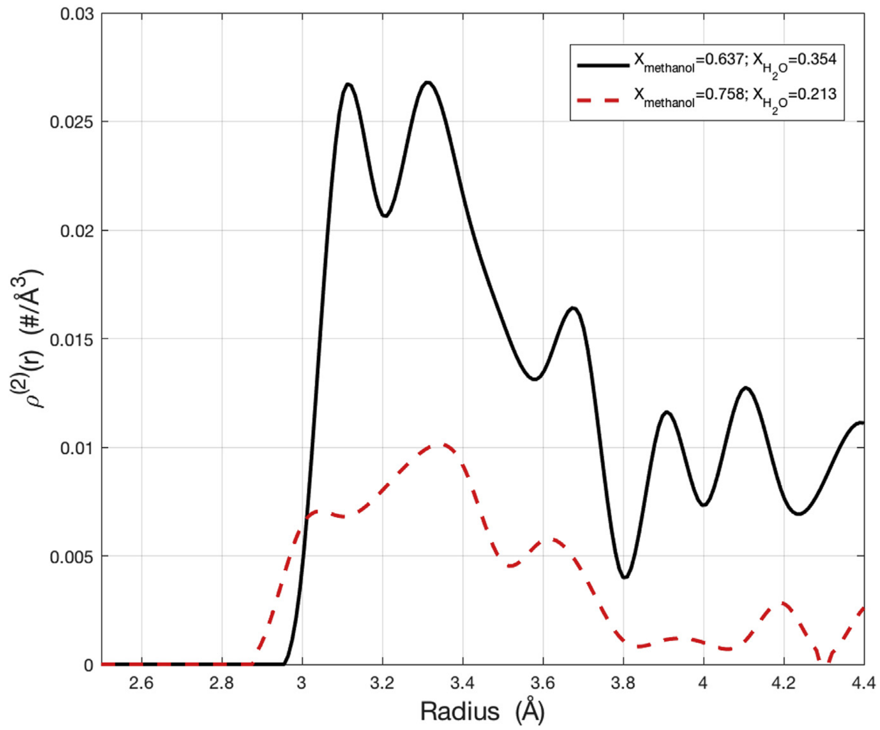

Figure 5.10. Methanol-water density distribution function at various composition of the aqueous phase

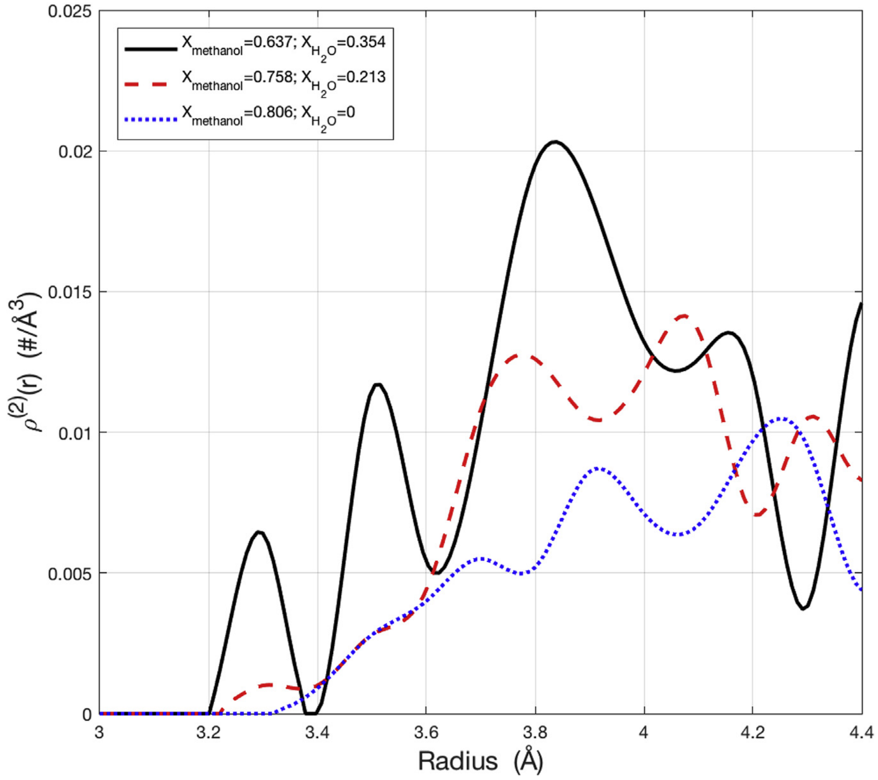

Figure 5.11. Cyclohexane-methanol density distribution function at various composition of the aqueous phase

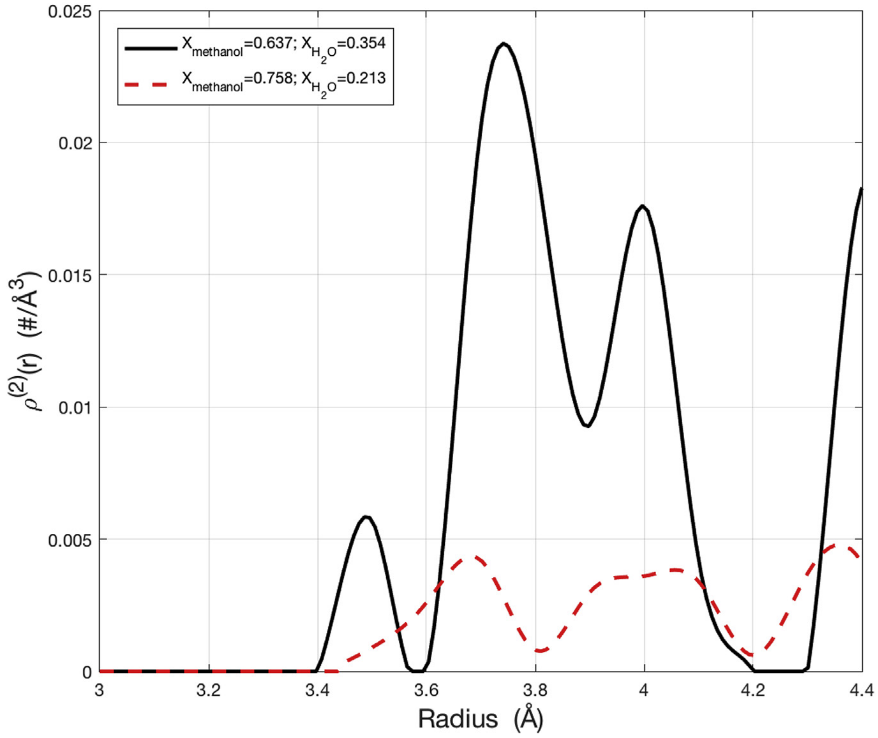

Figure 5.12. Cyclohexane-water density distribution function at various composition of the aqueous phase

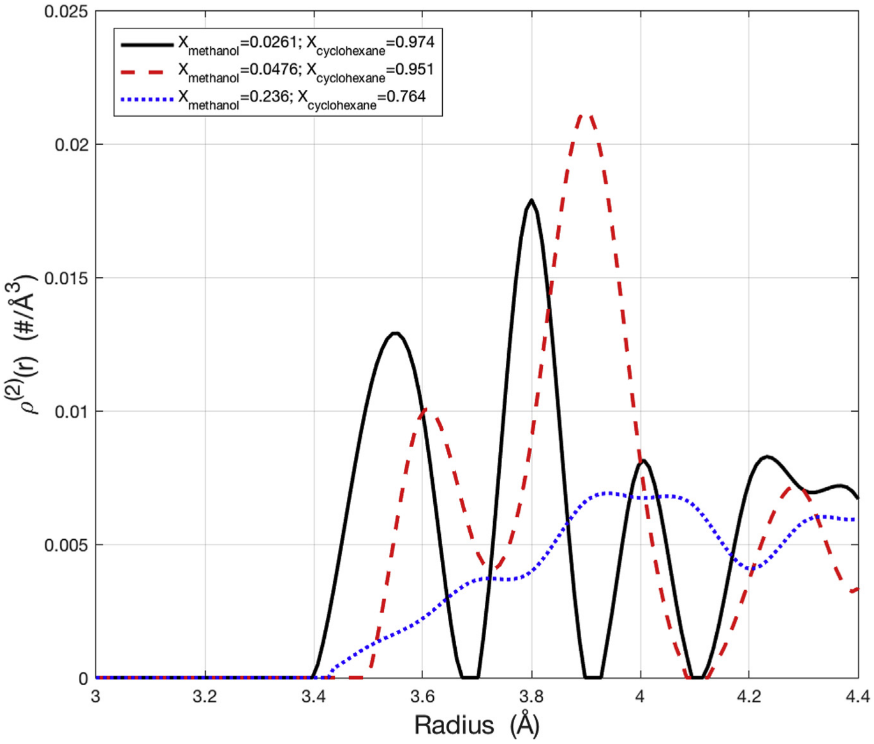

Figure 5.13. Methanol-cyclohexane density distribution function at various composition of the organic phase

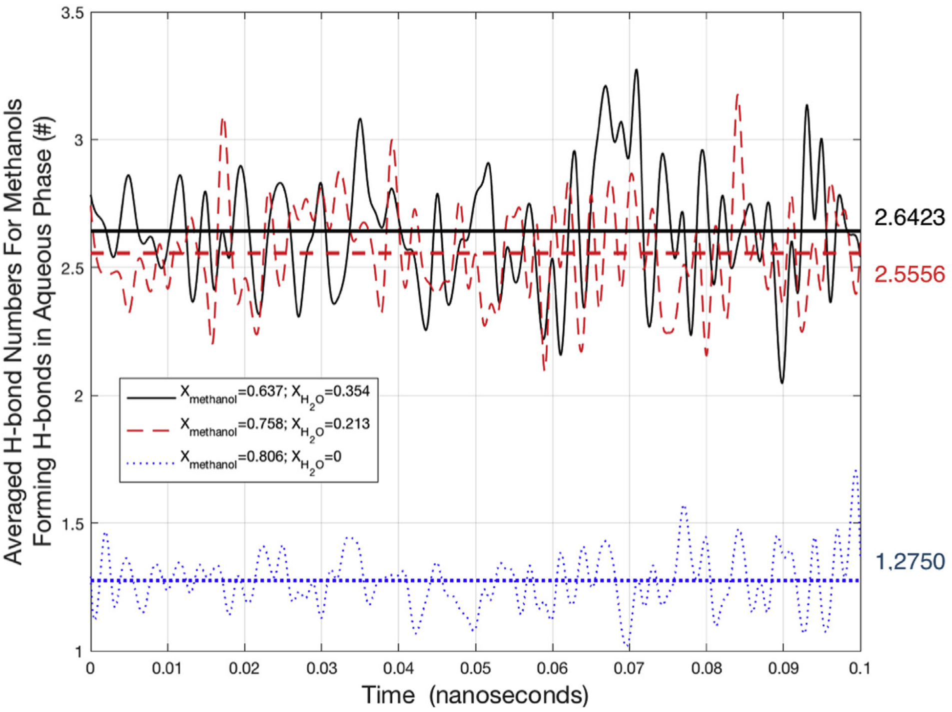

Figure 5.14. Number of hydrogen bonds per methanol molecule in the aqueous phase with different compositions of water

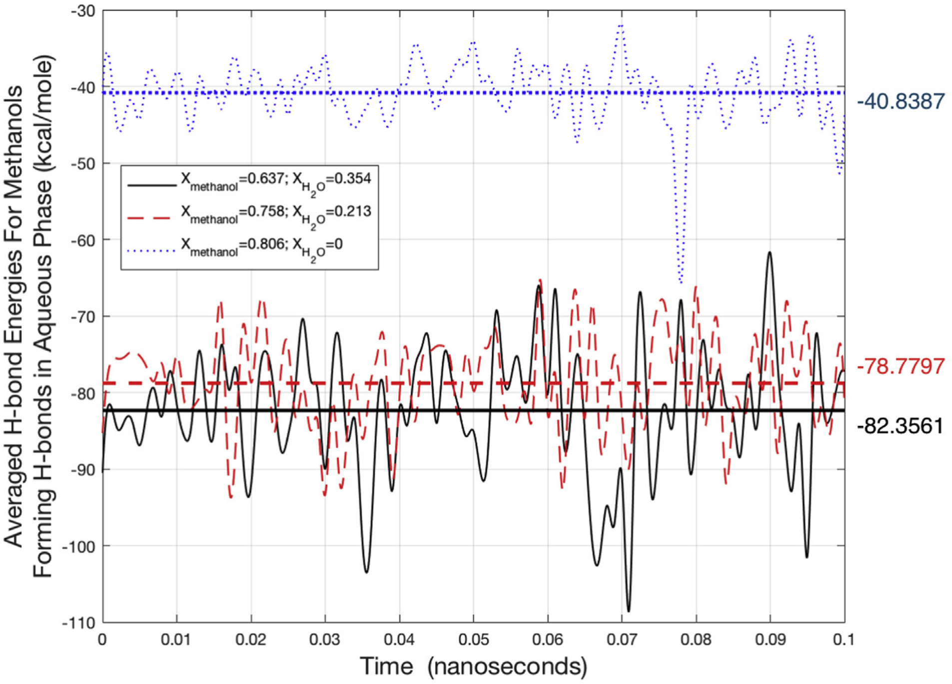

Figure 5.15. Hydrogen bond energy per methanol molecule in the aqueous phase with different compositions of water

BIBLIOGRAPHY

[1] D. S. Sholl and R. P. Lively. Seven Chemical Separations to Change the World : Purifying Mixtures Without Using Heat Would Lower Global Energy Use, Emissions and Pollution–And Open up New Routes to Resources. *Nature*, 532(7600) :435–438, 2016.

[2] R. P. Lively and D. S. Sholl. From Water to Organics in Membrane Separations. *Nature Materials*, 16(3) :276, 2017.

[3] S. Widodo, D. Ariono, I. G. Wenten, et al. Membrane Separation for Non-Aqueous Solution. 285(1) :012008, 2018.

[4] H. Yuan, B. Yu, H. Cong, Q. Peng, R. Yang, S. Yang, Z. Yang, Y. Luo, T. Xu, and H. Zhang. Modification Progress of Polymer Membranes for Gas Separation. *Reviews on Advanced Materials Science*, 44(3), 2016.

[5] A. Soleimany, S. S. Hosseini, and F. Gallucci. Recent Progress in Developments of Membrane Materials and Modification Techniques for High Performance Helium Separation and Recovery : A Review. *Chemical Engineering and Processing : Process Intensification*, 2017.

[6] M. Allen and D. J. Tildesley. *Computer Simulation of Liquids*. Oxford science publications. Clarendon Press, 1987.

[7] S. J. Weiner, P. A. Kollman, D. A. Case, U. C. Singh, C. Ghio, G. Alagona, S. Profeta, and P. Weiner. A New Force Field for Molecular Mechanical Simulation of Nucleic Acids and Proteins. *Journal of the American Chemical Society*, 106(3) :765–784, 1984.

[8] S. J. Weiner, P. A. Kollman, D. T. Nguyen, and D. A. Case. An All Atom Force Field for Simulations of Proteins and Nucleic Acids. *Journal of Computational Chemistry*, 7(2) :230–252, 1986.

[9] W. D. Cornell, P. Cieplak, C. I. Bayly, I. R. Gould, K. M. Merz, D. M. Ferguson, D. C. Spellmeyer, T. Fox, J. W. Caldwell, and P. A. Kollman. A Second Generation Force Field for the Simulation of Proteins, Nucleic Acids, and Organic Molecules. *Journal of the American Chemical Society*, 117(19) :5179–5197, 1995.

[10] L. Yang, C. Tan, M. Hsieh, J. Wang, Y. Duan, P. Cieplak, J. Caldwell, P. A. Kollman, and R. Luo. New-Generation Amber United-Atom Force Field. *The Journal of Physical Chemistry B*, 110(26) :13166–13176, 2006.

[11] J. Wang, R. M. Wolf, J. W. Caldwell, P. A. Kollman, and D. A. Case. Development and Testing of a General Amber Force Field. *Journal of Computational Chemistry*, 25(9) :1157–1174, 2004.

[12] W. L. Jorgensen, J. D. Madura, and C. J. Swenson. Optimized Intermolecular Potential Functions for Liquid Hydrocarbons. *Journal of the American Chemical Society*, 106(22) :6638–6646, 1984.

[13] W. L. Jorgensen and J. D. Madura. Temperature and Size Dependence for Monte Carlo Simulations of TIP4P Water. *Molecular Physics*, 56(6) :1381–1392, 1985.

[14] W. L. Jorgensen and C. J. Swenson. Optimized Intermolecular Potential Functions for Amides and Peptides. Structure and Properties of Liquid Amides. *Journal of the American Chemical Society*, 107(3) :1381–1392, 1985.

[15] W. L. Jorgensen, J. Gao, and C. Ravimohan. Monte Carlo Simulations of Alkanes in Water : Hydration Numbers and the Hydrophobic Effect. *The Journal of Physical Chemistry*, 89(16) :3470–3473, 1985.

[16] W. L. Jorgensen. Optimized Intermolecular Potential Functions for Liquid Alcohols. *Journal of Physical Chemistry*, 90(7) :1276–1284, 1986.

[17] A. D. MacKerell Jr, D. Bashford, M. Bellott, R. L. Dunbrack Jr, J. D. Evanseck, M. J. Field, S. Fischer, J. Gao, H. Guo, and S. Ha. All-Atom Empirical Potential for Molecular Modeling and Dynamics Studies of Proteins. *The Journal of Physical Chemistry B*, 102(18) :3586–3616, 1998.

[18] H. Sun. COMPASS : An Ab Initio Force-Field Optimized for Condensed-Phase Applications Overview With Details on Alkane and Benzene Compounds. *The Journal of Physical Chemistry B*, 102(38) :7338–7364, 1998.

[19] S. L. Mayo, B. D. Olafson, and W. A. Goddard. DREIDING : A Generic Force Field for Molecular Simulations. *Journal of Physical Chemistry*, 94(26) :8897–8909, 1990.

[20] A. Ö. Yazaydın, R. Q. Snurr, T. Park, K. Koh, J. Liu, M. D. LeVan, A. I. Benin, P. Jakubczak, M. Lanuza, D. B. Galloway, et al. Screening of Metal- Organic Frameworks for Carbon Dioxide Capture From Flue Gas Using a Combined Experimental and Modeling Approach. *Journal of the American Chemical Society*, 131(51) :18198–18199, 2009.

[21] S. Keskin and D. S. Sholl. Screening Metal- Organic Framework Materials for Membrane-Based Methane/Carbon Dioxide Separations. *The Journal of Physical Chemistry C*, 111(38) :14055–14059, 2007.

[22] H. Bux, C. Chmelik, R. Krishna, and J. Caro. Ethene/Ethane Separation by the MOf Membrane ZIF-8 : Molecular Correlation of Permeation, Adsorption, Diffusion. *Journal of Membrane Science*, 369(1-2) :284–289, 2011.

[23] K. Hinkle, X. Wang, X. Gu, C. Jameson, and S. Murad. Computational Molecular Modeling of Transport Processes in Nanoporous Membranes. *Processes*, 6(8) :124, 2018.

[24] K. R. Hinkle, C. J. Jameson, and S. Murad. Transport of Vanadium and Oxovanadium Ions Across Zeolite Membranes : A Molecular Dynamics Study. *The Journal of Physical Chemistry C*, 118(41) :23803–23810, 2014.

[25] B. Liu and B. Smit. Comparative Molecular Simulation Study of CO2/N2 and CH4/N2 Separation in Zeolites and Metal-Organic Frameworks. *Langmuir*, 25(10) :5918–5926, 2009.

[26] R. Krishna and J. M. Van Baten. Using Molecular Simulations for Screening of Zeolites for Separation of CO2/CH4 Mixtures. *Chemical Engineering Journal*, 133(1-3) :121–131, 2007.

[27] M. Karplus and J. A. McCammon. Molecular Dynamics Simulations of Biomolecules. *Nature Structural & Molecular Biology*, 9(9) :646, 2002.

[28] J. Ma, P. B. Sigler, Z. Xu, and M. Karplus. A Dynamic Model for the Allosteric Mechanism of GroEL. *Journal of Molecular Biology*, 302(2) :303–313, 2000.

[29] M. A. Young, S. Gonfloni, G. Superti-Furga, B. Roux, and J. Kuriyan. Dynamic Coupling Between the SH2 and SH3 Domains of c-Src and Hck Underlies Their Inactivation by C-Terminal Tyrosine Phosphorylation. *Cell*, 105(1) :115–126, 2001.

[30] K. Tai, T. Shen, U. Börjesson, M. Philippopoulos, and J. A. McCammon. Analysis of a 10-ns Molecular Dynamics Simulation of Mouse Acetylcholinesterase. *Biophysical Journal*, 81(2) :715–724, 2001.

[31] A. Cavalli, P. Ferrara, and A. Caflisch. Weak Temperature Dependence of the Free Energy Surface and Folding Pathways of Structured Peptides. *Proteins : Structure, Function, and Bioinformatics*, 47(3) :305–314, 2002.

[32] J. M. Haile. *Molecular Dynamics Simulation : Elementary Methods.* John Wiley & Sons, Inc., New York, NY, USA, 1st edition, 1992.

[33] D. A. Case, V. Babin, J. Berryman, R. M. Betz, Q. Cai, D. S. Cerutti, T. E. Cheatham Iii, T. A. Darden, R. E. Duke, H. Gohlke, et al. *Amber 14.* 2014.

[34] J. Tersoff. New Empirical Approach for the Structure and Energy of Covalent Systems. *Physical Review B*, 37(12) :6991, 1988.

[35] A. C. T. Van Duin, S. Dasgupta, F. Lorant, and W. A. Goddard. ReaxFF : A Reactive Force Field for Hydrocarbons. *The Journal of Physical Chemistry A*, 105(41) :9396–9409, 2001.

[36] M. Levitt and A. Warshel. Computer Simulation of Protein Folding. *Nature*, 253(5494) :694, 1975.

[37] B. D. Todd and P. J. Daivis. *Nonequilibrium Molecular Dynamics : Theory, Algorithms and Applications.* Cambridge University Press, 2017.

[38] M. S. Green. Markoff Random Processes and the Statistical Mechanics of Time-Dependent Phenomena. II. Irreversible Processes in Fluids. *The Journal of Chemical Physics*, 22(3) :398–413, 1954.

[39] R. Kubo. Statistical-Mechanical Theory of Irreversible Processes. I. General Theory and Simple Applications to Magnetic and Conduction Problems. *Journal of the Physical Society of Japan*, 12(6) :570–586, 1957.

[40] W. T. Ashurst and W. G. Hoover. Dense-Fluid Shear Viscosity via Nonequilibrium Molecular Dynamics. *Physical Review A*, 11(2) :658, 1975.

[41] E. M. Gosling, I. R. McDonald, and K. Singer. On the Calculation by Molecular Dynamics of the Shear Viscosity of a Simple Fluid. *Molecular Physics*, 26(6) :1475–1484, 1973.

[42] Y. Morigami, M. Kondo, J. Abe, H. Kita, and K. Okamoto. The First Large-Scale Pervaporation Plant Using Tubular-Type Module With Zeolite NaAs Membrane. *Separation and Purification Technology*, 25(1) :251 – 260, 2001.

[43] T. Gallego-Lizon, E. Edwards, G. Lobiundo, and L. F. dos Santos. Dehydration of Water/t-Butanol Mixtures by Pervaporation : Comparative Study of Commercially Available Polymeric, Microporous Silica and Zeolite Membranes. *Journal of Membrane Science*, 197(1-2) :309–319, 2002.

[44] H. Richter, I. Voigt, and J. Kühnert. Dewatering of Ethanol by Pervaporation and Vapour Permeation With Industrial Scale NaA-Membranes. *Desalination*, 1(199) :92–93, 2006.

[45] Y. Liu, Z. Yang, C. Yu, X. Gu, and N. Xu. Effect of Seeding Methods on Growth of NaA Zeolite Membranes. *Microporous and Mesoporous Materials*, 143(2-3) :348–356, 2011.

[46] Y. Liu, X. Wang, Y. Zhang, Y. He, and X. Gu. Scale-up of NaA Zeolite Membranes on α-Al2O3 Hollow Fibers by a Secondary Growth Method with Vacuum Seeding. *Chinese Journal of Chemical Engineering*, 23(7) :1114–1122, 2015.

[47] J. J. Jafar and P. M. Budd. Separation of Alcohol/Water Mixtures by Pervaporation Through Zeolite A Membranes. *Microporous Materials*, 12(4-6) :305–311, 1997.

[48] M. Kondo, M. Komori, H. Kita, and K. Okamoto. Tubular-Type Pervaporation Module With Zeolite NaA Membrane. *Journal of Membrane Science*, 133(1) :133–141, 1997.

[49] K. Okamoto, H. Kita, K. Horii, and K. T. Kondo. Zeolite NaA Membrane : Preparation, Single-Gas Permeation, and Pervaporation and Vapor Permeation of Water/Organic Liquid Mixtures. *Industrial & Engineering Chemistry Research*, 40(1) :163–175, 2001.

[50] A. W. C. Van den Berg, L. Gora, J. C. Jansen, M. Makkee, and T. Maschmeyer. Zeolite A Membranes Synthesized on a UV-Irradiated TiO2 Coated Metal Support : The High Pervaporation Performance. *Journal of Membrane Science*, 224(1-2) :29–37, 2003.

[51] S. G. Sorenson, E. A. Payzant, W. T. Gibbons, B. Soydas, H. Kita, R. D. Noble, and J. L. Falconer. Influence of Zeolite Crystal Expansion/Contraction on Naa Zeolite Membrane Separations. *Journal of Membrane Science*, 366(1-2) :413–420, 2011.

[52] A. I. Sarakhov, V. F. Kononyuk, and M. M. Dubinin. Variation in Parameters of Crystalline-Structure of Zeolites During Adsorption. *Advances in Chemistry Series*, (121) :403–413, 1973.

[53] M. Noack, M. Schneider, A. Dittmar, G. Georgi, and J. Caro. The Change of the

Unit Cell Dimension of Different Zeolite Types by Heating and Its Influence on Supported Membrane Layers. *Microporous and Mesoporous Materials*, 117(1-2) :10–21, 2009.

[54] C. H. Baerlocher and L. B. McCusker. Database of Zeolite Structures : http ://www.iza-structure.org/databases/.

[55] S. Murad, W. Jia, and M. Krishnamurthy. Ion-Exchange of Monovalent and Bivalent Cations With NaA Zeolite Membranes : A Molecular Dynamics Study. *Molecular Physics*, 102(19-20) :2103–2112, 2004.

[56] S. Murad, P. Ravi, and J. G. Powles. A Computer Simulation Study of Fluids in Model Slit, Tubular, and Cubic Micropores. *The Journal of Chemical Physics*, 98(12) :9771–9781, 1993.

[57] U. Essmann, L. Perera, M. L. Berkowitz, T. Darden, H. Lee, and L. G. Pedersen. A Smooth Particle Mesh Ewald Method. *The Journal of Chemical Physics*, 103(19) :8577–8593, 1995.

[58] B. Vujic and A. P. Lyubartsev. Transferable Force-Field for Modelling of CO2, N2, O2 and Ar in All Silica and Na+ Exchanged Zeolites. *Modelling and Simulation in Materials Science and Engineering*, 24(4) :045002, 2016.

[59] W. L. Jorgensen, J. Chandrasekhar, J. D. Madura, R. W. Impey, and M. L. Klein. Comparison of Simple Potential Functions for Simulating Liquid Water. *The Journal of Chemical Physics*, 79(2) :926–935, 1983.

[60] S. H. Lee, G. K. Moon, S. G. Choi, and H. S. Kim. Molecular Dynamics Simulation Studies of Zeolite-A. 3. Structure and Dynamics of Na+ Ions and Water Molecules in a Rigid Zeolite-A. *The Journal of Physical Chemistry*, 98(6) :1561–1569, 1994.

[61] S. Plimpton. Fast Parallel Algorithms for Short-Range Molecular Dynamics. *Journal of Computational Physics*, 117(1) :1–19, 1995.

[62] E. Polak and G. Ribiere. Note sur la convergence de méthodes de directions conjuguées. *ESAIM : Mathematical Modelling and Numerical Analysis-Modélisation Mathématique et Analyse Numérique*, 3(1) :35–43, 1969.

[63] L. Verlet. Computer "Experiments" on Classical Fluids. II. Equilibrium Correlation Functions. *Physical Review*, 165(1) :201, 1968.

[64] S. Nosé. A Unified Formulation of the Constant Temperature Molecular Dynamics Methods. *The Journal of Chemical Physics*, 81(1) :511–519, 1984.

[65] W. G. Hoover. Canonical Dynamics : Equilibrium Phase-Space Distributions. *Physical Review A*, 31(3) :1695–1697, 1985.

[66] D. A. Faux, W. Smith, and T. R. Forester. Molecular Dynamics Studies of Hydrated and Dehydrated Na+-Zeolite-4A. *The Journal of Physical Chemistry B*, 101(10) :1762–1768, 1997.

[67] É. Csányi, T. Kristóf, and G. Lendvay. Potential Model Development Using Quantum Chemical Information for Molecular Simulation of Adsorption Equilibria of Water- Methanol (Ethanol) Mixtures in Zeolite NaA-4. *The Journal of Physical Chemistry C*, 113(28) :12225–12235, 2009.

[68] C. R. A. Catlow, C. M. Freeman, B. Vessal, S. M. Tomlinson, and M. Leslie. Molecular Dynamics Studies of Hydrocarbon Diffusion in Zeolites. *J. Chem. Soc., Faraday Trans.*, 87 :1947–1950, 1991.

[69] S. M. Auerbach, N. J. Henson, A. K. Cheetham, and H. I. Metiu. Transport Theory for Cationic Zeolites : Diffusion of Benzene in Na-Y. *The Journal of Physical Chemistry*, 99(26) :10600–10608, 1995.

[70] M. J. Frisch, G. W. Trucks, H. B. Schlegel, G. E. Scuseria, M. A. Robb, J. R. Cheeseman, G. Scalmani, V. Barone, B. Mennucci, G.A. Petersson, et al. Gaussian 09, revision a. 02, gaussian. *Inc., Wallingford, CT*, 200 :28, 2009.

[71] G. Kresse and J. Furthmüller. Efficient Iterative Schemes for Ab Initio Total-Energy Calculations Using a Plane-Wave Basis Set. *Physical Review B*, 54 :11169–11186, Oct 1996.

[72] T. A. Manz and D. S. Sholl. Chemically Meaningful Atomic Charges That Reproduce the Electrostatic Potential in Periodic and Nonperiodic Materials. *Journal of Chemical Theory and Computation*, 6(8) :2455–2468, 2010.

[73] T. Watanabe, T. A. Manz, and D. S. Sholl. Accurate Treatment of Electrostatics During Molecular Adsorption in Nanoporous Crystals Without Assigning Point Charges to Framework Atoms. *The Journal of Physical Chemistry C*, 115(11) :4824–4836, 2011.

[74] C. Campañá, B. Mussard, and T. K. Woo. Electrostatic Potential Derived Atomic Charges for Periodic Systems Using a Modified Error Functional. *Journal of Chemical Theory and Computation*, 5(10) :2866–2878, 2009.

[75] C. R. A. Catlow, R. G. Bell, J. D. Gale, and D. W. Lewis. *Modelling of structure and reactivity in zeolites*, volume 97, pages 87–100. Elsevier, 1995.

[76] M. Mabilia, R. A. Pearlstein, and A. J. Hopfinger. Molecular Modeling of Zeolite Structure. 1. Properties of the Sodalite Cage. *Journal of the American Chemical Society*, 109(26) :7960–7968, 1987.

[77] J. B. Nicholas, A. J. Hopfinger, F. R. Trouw, and L. E. Iton. Molecular Modeling of Zeolite Structure. 2. Structure and Dynamics of Silica Sodalite and Silicate Force Field. *Journal of the American Chemical Society*, 113(13) :4792–4800, 1991.

[78] D. Dubbeldam, S. Calero, T. J. H. Vlugt, R. Krishna, T. L. M. Maesen, E. Beerdsen, and B. Smit. Force Field Parametrization Through Fitting on Inflection Points in Isotherms. *Physical Review Letters*, 93 :088302, Aug 2004.

[79] A. Garcia-Sanchez, C. O. Ania, J. B. Parra, D. Dubbeldam, T. J. H. Vlugt, R. Krishna, and S. Calero. Transferable Force Field for Carbon Dioxide Ad-

sorption in Zeolites. *The Journal of Physical Chemistry C*, 113(20) :8814–8820, 2009.

[80] S. Murad, P. Ravi, and J. G. Powles. A Computer Simulation Study of Fluids in Model Slit, Tubular, and Cubic Micropores. *The Journal of Chemical Physics*, 98(12) :9771–9781, 1993.

[81] F. Qu, R. Shi, L. Peng, Y. Zhang, X. Gu, X. Wang, and S. Murad. Understanding the Effect of Zeolite Crystal Expansion/Contraction on Separation Performance of NaA Zeolite Membrane : A Combined Experimental and Molecular Simulation Study. *Journal of Membrane Science*, 539 :14–23, 2017.

[82] G. Maurin, R. G. Bell, S. Devautour, F. Henn, and J. C. Giuntini. Modeling the Effect of Hydration in Zeolite Na+- Mordenite. *The Journal of Physical Chemistry B*, 108(12) :3739–3745, 2004.

[83] R. S. Cahn, C. Ingold, and V. Prelog. Specification of Molecular Chirality. *Angewandte Chemie International Edition*, 5(4) :385–415, 1966.

[84] F. Arnesano, A. Pannunzio, M. Coluccia, and G. Natile. Effect of Chirality in Platinum Drugs. *Coordination Chemistry Reviews*, 284 :286–297, 2015.

[85] D. Iacopetta, A. Carocci, M. S. Sinicropi, A. Catalano, G. Lentini, J. Ceramella, R. Curcio, and M. C. Caroleo. Old Drug Scaffold, New Activity : Thalidomide-Correlated Compounds Exert Different Effects on Breast Cancer Cell Growth and Progression. *ChemMedChem*, 12(5) :381–389, 2017.

[86] W. H. Pirkle, J. M. Finn, J. L. Schreiner, and B. C. Hamper. A Widely Useful Chiral Stationary Phase for the High-Performance Liquid Chromatography Separation of Enantiomers. *Journal of the American Chemical Society*, 103(13) :3964–3966, 1981.

[87] A. M. Blum, K. G. Lynam, and E. C. Nicolas. Use of a New Pirkle-Type Chiral Stationary Phase in Analytical and Preparative Subcritical Fluid Chromatography of Pharmaceutical Compounds. *Chirality*, 6(4) :302–313, 1994.

[88] T. Suzuki, S. Timofei, B. E. Iuoras, G. Uray, P. Verdino, and W. M. Fabian. Quantitative Structure–Enantioselective Retention Relationships for Chromatographic Separation of Arylalkylcarbinols on Pirkle Type Chiral Stationary Phases. *Journal of Chromatography A*, 922(1-2) :13–23, 2001.

[89] K. Addadi, K. Sekkoum, N. Belboukhari, A. Cheriti, and H. Y. Aboul-Enein. Screening Approach for Chiral Separation of β-Aminoketones by HPLC on Various Polysaccharide-Based Chiral Stationary Phases. *Chirality*, 27(5) :332–338, 2015.

[90] B. Chankvetadze. Recent Developments on Polysaccharide-Based Chiral Stationary Phases for Liquid-Phase Separation of Enantiomers. *Journal of Chromatography A*, 1269 :26–51, 2012.

[91] J. J. Ha, H. J. Han, H. E. Kim, J. S. Jin, E. D. Jeong, and M. H. Hyun. Development of an Improved Ligand Exchange Chiral Stationary Phase Based on

Leucinol for the Resolution of Proton Pump Inhibitors. *Journal of Pharmaceutical and Biomedical Analysis*, 100 :88–93, 2014.

[92] D. H. Ma, J. S. Jin, E. D. Jeong, and M. H. Hyun. Effect of the Residual Silanol Group Protection on the Liquid Chromatographic Resolution of α-Amino Acids and Proton Pump Inhibitors on a Ligand Exchange Chiral Stationary Phase. *Journal of Separation Science*, 36(8) :1349–1355, 2013.

[93] R. B. Kasat, E. I. Franses, and N. L. Wang. Experimental and Computational Studies of Enantioseparation of Structurally Similar Chiral Compounds on Amylose Tris(3,5- Dimethylphenylcarbamate). *Chirality*, 22(6) :565–579, 2010.

[94] T. Ikai and Y. Okamoto. Structure Control of Polysaccharide Derivatives for Efficient Separation of Enantiomers by Chromatography. *Chemical Reviews*, 109(11) :6077–6101, 2009.

[95] C. Yamamoto, E. Yashima, and Y. Okamoto. Structural Analysis of Amylose Tris(3,5- Dimethylphenylcarbamate) by NMR Relevant to Its Chiral Recognition Mechanism in HPLC. *Journal of the American Chemical Society*, 124(42) :12583–12589, 2002.

[96] S. Ma, S. Shen, H. Lee, M. Eriksson, X. Zeng, J. Xu, K. Fandrick, N. Yee, C. Senanayake, and N. Grinberg. Mechanistic Studies on the Chiral Recognition of Polysaccharide-Based Chiral Stationary Phases Using Liquid Chromatography and Vibrational Circular Dichroism : Reversal of Elution Order of N-Substituted alpha-Methyl Phenylalanine Esters. *Journal of Chromatography A*, 1216(18) :3784–3793, 2009.

[97] R. B. Kasat, N. L. Wang, and E. I. Franses. Effects of Backbone and Side Chain on the Molecular Environments of Chiral Cavities in Polysaccharide-Based Biopolymers. *Biomacromolecules*, 8(5) :1676–1685, 2007.

[98] L. H. Easson and E. Stedman. Studies on the Relationship Between Chemical Constitution and Physiological Action : Molecular Dissymmetry and Physiological Activity. *The Biochemical Journal*, 27(4) :1257–1266, 1933.

[99] Y. Okamoto and Y. Kaida. Resolution by High-Performance Liquid Chromatography Using Polysaccharide Carbamates and Benzoates as Chiral Stationary Phases. *Journal of Chromatography A*, 666(1-2) :403–419, 1994.

[100] Y. Tang. Significance of Mobile Phase Composition in Enantioseparation of Chiral Drugs by HPLC on a Cellulose-Based Chiral Stationary Phase. *Chirality*, 8(1) :136–142, 1996.

[101] J. Lin, T. Nakagama, K. Uchiyama, and T. Hobo. Temperature Effect on Chiral Recognition of Some Amino Acids With Molecularly Imprinted Polymer Filled Capillary Electrochromatography. *Biomedical Chromatography*, 11(5) :298–302, 1997.

[102] S. Jönsson, A. Schön, R. Isaksson, C. Pettersson, and G. Pettersson. An Unexpected Temperature Effect Obtained on Enantiomer Separation Using CBH I-Silica as a Chiral Stationary Phase : Increase in Retention and Enantioselec-

tivity at Elevated Column Temperature : A Chromatographic and Microcalorimetric Study. *Chirality*, 4(8) :505, 1992.

[103] J. Haginaka, J. Wakai, K. Takahashi, H. Yasuda, and T. Katagi. Chiral Separation of Propranolol and Its Ester Derivatives on an Ovomucoid-Bonded Silica : Influence of pH, Ionic Strength and Organic Modifier on Retention, Enantioselectivity and Enantiomeric Elution Order. *Chromatographia*, 29(11-12) :587–592, 1990.

[104] Y. Guo and S. Gaiki. Retention and Selectivity of Stationary Phases for Hydrophilic Interaction Chromatography. *Journal of Chromatography A*, 1218(35) :5920–5938, 2011.

[105] Y. K. Ye, S. Bai, S. Vyas, and M. J. Wirth. NMR and Computational Studies of Chiral Discrimination by Amylose Tris(3,5- Dimethylphenylcarbamate). *The Journal of Physical Chemistry B*, 111(5) :1189–1198, 2007.

[106] F. Godschalk, S. Genheden, P. Söderhjelm, and U. Ryde. Comparison of MM/GBSA Calculations Based on Explicit and Implicit Solvent Simulations. *Physical Chemistry Chemical Physics*, 15(20) :7731–7739, 2013.

[107] Y. Li, D. Liu, P. Wang, and Z. Zhou. Computational Study of Enantioseparation by Amylose Tris (3, 5-Dimethylphenylcarbamate)-Based Chiral Stationary Phase. *Journal of Separation Science*, 33(20) :3245–3255, 2010.

[108] H. Tsui, N. L. Wang, and E. I. Franses. Chiral Recognition Mechanism of Acyloin-Containing Chiral Solutes by Amylose Tris [(S)-α-Methylbenzylcarbamate]. *The Journal of Physical Chemistry B*, 117(31) :9203–9216, 2013.

[109] A. D. Becke. Density-Functional Exchange-Energy Approximation With Correct Asymptotic Behavior. *Physical Review A*, 38(6) :3098, 1988.

[110] C. Lee, W. Yang, and R. G. Parr. Development of the Colle-Salvetti Correlation-Energy Formula Into a Functional of the Electron Density. *Physical Review B*, 37(2) :785, 1988.

[111] P. Hohenberg and W. Kohn. Inhomogeneous electron gas. *Physical review*, 136(3B) :B864, 1964.

[112] C. I. Bayly, P. Cieplak, W. Cornell, and P. A. Kollman. A Well-Behaved Electrostatic Potential Based Method Using Charge Restraints for Deriving Atomic Charges : The RESP Model. *The Journal of Physical Chemistry*, 97(40) :10269–10280, 1993.

[113] A. D. Bochevarov, E. Harder, T. F. Hughes, J. R. Greenwood, D. A. Braden, D. M. Philipp, D. Rinaldo, M. D. Halls, J. Zhang, and R. A. Friesner. Jaguar : A High-Performance Quantum Chemistry Software Program With Strengths in Life and Materials Sciences. *International Journal of Quantum Chemistry*, 113(18) :2110–2142, 2013.

[114] M. W. Schmidt, K. K. Baldridge, J. A. Boatz, S. T. Elbert, M. S. Gordon, J. H. Jensen, S. Koseki, N. Matsunaga, K. A. Nguyen, S. Su, T. L. Windus,

M. Dupuis, and J. A. Montgomery Jr. General Atomic and Molecular Electronic Structure System. *Journal of Computational Chemistry*, 14(11) :1347–1363, 1993.

[115] A. A. Granovsky. Extended Multi-Configuration Quasi-Degenerate Perturbation Theory : The New Approach to Multi-State Multi-Reference Perturbation Theory. *The Journal of Chemical Physics*, 134(21) :214113, 2011.

[116] P. S. Shenkin and D. Q. McDonald. Cluster Analysis of Molecular Conformations. *Journal of Computational Chemistry*, 15(8) :899–916, 1994.

[117] H. J. Berendsen, J. Postma, W. F. van Gunsteren, A. DiNola, and J. R. Haak. Molecular Dynamics With Coupling to an External Bath. *The Journal of Chemical Physics*, 81(8) :3684–3690, 1984.

[118] J. Ryckaert, G. Ciccotti, and H. J. C. Berendsen. Numerical Integration of the Cartesian Equations of Motion of a System With Constraints : Molecular Dynamics of n-Alkanes. *Journal of Computational Physics*, 23(3) :327–341, 1977.

[119] W. Humphrey, A. Dalke, and K. Schulten. VMD : Visual Molecular Dynamics. *Journal of Molecular Graphics*, 14 :33–38, 1996.

[120] L. Martínez, R. Andrade, E. G. Birgin, and J. M. Martínez. PACKMOL : A Package for Building Initial Configurations for Molecular Dynamics Simulations. *Journal of Computational Chemistry*, 30(13) :2157–2164, 2009.

[121] G. N. Ramachandran. Stereochemistry of Polypeptide Chain Configurations. *Journal of Molecular Biology*, 7(1) :95–99, 1963.

[122] Y. Okamoto, R. Aburatani, T. Fukumoto, and K. Hatada. Useful chiral stationary phases for hplc. amylose tris (3, 5-dimethylphenylcarbamate) and tris (3, 5-dichlorophenylcarbamate) supported on silica gel. *Chemistry Letters*, 16(9) :1857–1860, 1987.

[123] J. P. Castillo-Gonzalez, N. I. Gonzalez-Pena, and M. A. Munoz. Absolute Configuration Assignment in Racemic trans-Stilbene Oxide Using Chiral Liquid Chromatography With Combined Chiroptical Detection and Time-Dependent Density Functional Theory Calculations. *Journal of the Chilean Chemical Society*, 61(1) :2777–2779, 2016.

[124] R. Cirilli, R. Ferretti, E. De Santis, B. Gallinella, L. Zanitti, and F. La Torre. High-Performance Liquid Chromatography Separation of Enantiomers of Flavanone and 2'-Hydroxychalcone Under Reversed-Phase Conditions. *Journal of Chromatography A*, 1190(1) :95–101, 2008.

[125] K. Sembongi, M. Tanaka, K. Sakurada, M. Kobayashi, S. Itagaki, T. Hirano, and K. Iseki. A New Method for Determination of Both Thalidomide Enantiomers Using HPLC Systems. *Biological and Pharmaceutical Bulletin*, 31(3) :497–500, 2008.

[126] R. Gaggeri, D. Rossi, S. Collina, B. Mannucci, M. Baierl, and M. Juza. Quick

Development of an Analytical Enantioselective High Performance Liquid Chromatography Separation and Preparative Scale-Up for the Flavonoid Naringenin. *Journal of Chromatography A*, 1218(32) :5414–5422, 2011.

[127] J. Kang and G. Hempel. Effects of Diethylamine on Capillary Chromatographic Enantioseparation of Some Chiral Analytes Using Polysaccharide Stationary Phases With Pure Polar Solvents as Mobile Phases. *Bulletin of the Korean Chemical Society*, 28(6) :1035–1038, 2007.

[128] B. Chankvetadze, I. Kartozia, C. Yamamoto, and Y. Okamoto. Comparative Enantioseparation of Selected Chiral Drugs on Four Different Polysaccharide-Type Chiral Stationary Phases Using Polar Organic Mobile Phases. *Journal of Pharmaceutical and Biomedical Analysis*, 27(3) :467–478, 2002.

[129] S. Tsuzuki, K. Honda, T. Uchimaru, M. Mikami, and K. Tanabe. Origin of Attraction and Directionality of the π/π Interaction : Model Chemistry Calculations of Benzene Dimer Interaction. *Journal of the American Chemical Society*, 124(1) :104–112, 2002.

[130] S. Tsuzuki, T. Uchimaru, and M. Mikami. Intermolecular Interaction between Hexafluorobenzene and Benzene : Ab Initio Calculations Including CCSD(T) Level Electron Correlation Correction. *The Journal of Physical Chemistry A*, 110(5) :2027–2033, 2006.

[131] W. H. Pirkle and Y. Liu. On the Relevance of Face-To-Edge π-π Interactions to Chiral Recognition. *Journal of Chromatography A*, 749(1) :19–24, 1996.

[132] X. Wang, D. W. House, P. A. Oroskar, A. Oroskar, A. Oroskar, C. J. Jameson, and S. Murad. Molecular Dynamics Simulations of the Chiral Recognition Mechanism for a Polysaccharide Chiral Stationary Phase in Enantiomeric Chromatographic Separations. *Molecular Physics*, 117 :3569–3588, 2019.

[133] B. Zhao, P. A. Oroskar, X. Wang, D. House, A. Oroskar, A. Oroskar, C. Jameson, and S. Murad. The Composition of the Mobile Phase Affects the Dynamic Chiral Recognition of Drug Molecules by the Chiral Stationary Phase. *Langmuir*, 33(42) :11246–11256, 2017.

[134] C. D. Lorenz, P. S. Crozier, J. A. Anderson, and A. Travesset. Molecular Dynamics of Ionic Transport and Electrokinetic Effects in Realistic Silica Channels. *The Journal of Physical Chemistry C*, 112(27) :10222–10232, 2008.

[135] L. T. Zhuravlev. The Surface Chemistry of Amorphous Silica. Zhuravlev Model. *Colloids and Surfaces A : Physicochemical and Engineering Aspects*, 173(1-3) :1–38, 2000.

[136] R. K. Iler. The Chemistry of Silica : Solubility, Polymerization, Colloid and Surface and Surface Properties, and Biochemistry. 1979.

[137] Accelrys Inc. Cerius2 Modeling Environment, Release 4.0. 1999.

[138] E. R. Cruz-Chu, A. Aksimentiev, and K. Schulten. Water- Silica Force Field for Simulating Nanodevices. *The Journal of Physical Chemistry B*, 110(43) :21497–21508, 2006.

[139] E. Demiralp, T. Çağin, and W. A. Goddard III. Morse Stretch Potential Charge Equilibrium Force Field for Ceramics : Application to the Quartz-Stishovite Phase Transition and to Silica Glass. *Physical Review Letters*, 82(8) :1708, 1999.

[140] J. C. Fogarty, H. M. Aktulga, A. Y. Grama, A. C. T. Van Duin, and S. A. Pandit. A Reactive Molecular Dynamics Simulation of the Silica-Water Interface. *The Journal of Chemical Physics*, 132(17) :174704, 2010.

[141] A. C. T. Van Duin, A. Strachan, S. Stewman, Q. Zhang, X. Xu, and W. A. Goddard. ReaxFFSiO Reactive Force Field for Silicon and Silicon Oxide Systems. *The Journal of Physical Chemistry A*, 107(19) :3803–3811, 2003.

[142] J. J. Karnes and I. Benjamin. Mechanism and Dynamics of Molecular Exchange at the Silica/Binary Solvent Mixtures Interface. *The Journal of Physical Chemistry A*, 119(50) :12073–12081, 2015.

[143] J. J. Karnes and I. Benjamin. Mechanism and Dynamics of Molecular Exchange at the Silica/Binary Solvent Mixtures Interface. *The Journal of Physical Chemistry A*, 119(50) :12073–12081, 2015.

[144] S. Leroch and M. Wendland. Simulation of Forces Between Humid Amorphous Silica Surfaces : A Comparison of Empirical Atomistic Force Fields. *The Journal of Physical Chemistry C*, 116(50) :26247–26261, 2012.

[145] G. J. Martyna, M. L. Klein, and M. Tuckerman. Nosé–Hoover Chains : The Canonical Ensemble via Continuous Dynamics. *The Journal of Chemical Physics*, 97(4) :2635–2643, 1992.

[146] G. J. Martyna, M. E. Tuckerman, D. J. Tobias, and M. L. Klein. Explicit Reversible Integration Algorithms for Extended Systems. *Mol. Phys*, 87 :1117–1157, 1996.

[147] R. C. Reid, J. M. Prausnitz, and B. E. Poling. *The Properties of Gases and Liquids.* McGraw Hill Book Co., New York, NY, 1987.

[148] A. Nasehzadeh, M. Mohseni, and K. Azizi. The Effect of Temperature on the Lennard-Jones (6-12) Pair Potential Function. *Journal of Molecular Structure : THEOCHEM*, 589-590(Supplement C) :329–335, 2002.

[149] P. Oracz, M. Góral, B. Wiśniewska-Gocłowska, D. G. Shaw, and A. Mączyński. IUPAC-NIST Solubility Data Series. 101. Alcohols + Hydrocarbons + Water. Part 2. C1-C3 Alcohols + Aliphatic Hydrocarbons. *Journal of Physical and Chemical Reference Data*, page 033102, 2016.

[150] H. Yuan, S. Murad, C. J. Jameson, and J. D. Olson. Molecular Dynamics Simulations of Xe Chemical Shifts and Solubility in n-Alkanes. *The Journal of Physical Chemistry C*, 111(43) :15771–15783, 2007.

[151] H. Yuan, C. J. Jameson, S. K. Gupta, J. D. Olson, and S. Murad. Prediction of Henry's Constants of Xenon in cyclo-Alkanes from Molecular Dynamics Simulations. *Fluid Phase Equilibria*, 269(1) :73–79, 2008.

[152] H. Yuan, C. Gosling, P. Kokayeff, and S. Murad. Prediction of Hydrogen Solubility in Heavy Hydrocarbons Over a Range of Temperatures and Pressures Using Molecular Dynamics Simulations. *Fluid Phase Equilibria*, 299(1) :94–101, 2010.

[153] R. W. Hockney and J. W. Eastwood. *Computer Simulation Using Particles.* crc Press, 1988.

[154] T. M. Letcher, B. C. Bricknell, and J. D. Sewry. Phase Equilibria for (An Alkanol+ Hept-1-yne+ Water) at the Temperature 298.15 K. *The Journal of Chemical Thermodynamics*, 25(10) :1183–1187, 1993.

[155] M. B. G. de Doz, C. M. Bonatti, and H. N. Sólimo. (Liquid+ Liquid) Equilibria of Ternary and Quaternary Systems With Two Hydrocarbons, an Alcohol, and Water at 303.15 K. Systems Containing Cyclohexane, Benzene, Ethanol, and Water. *Journal of Chemical Thermodynamics*, 35(12) :2055–2065, 2003.

[156] J. Liu, Z. Qin, G. Wang, X. Hou, and J. Wang. Critical Properties of Binary and Ternary Mixtures of Hexane+ Methanol, Hexane+ Carbon Dioxide, Methanol+ Carbon Dioxide, and Hexane+ Carbon Dioxide+ Methanol. *Journal of Chemical Engineering Data*, 48(6) :1610–1613, 2003.

[157] M. A. McCool and L. A. Woolf. Self-Diffusion Measurements Under Pressure With a Diaphragm Cell. Theory of the Method and Experimental Results for Cyclohexane. *High Temp-High Press*, 4 :85–95, 1972.

[158] A. Skrzecza, D. Shaw, A. Maczynski, and A. Skrzecz. IUPAC-NIST Solubility Data Series 69. Ternary Alcohol-Hydrocarbon-Water Systems. *Journal of Physical and Chemical Reference Data*, 28(4) :983, 1999.

[159] N. Zhang, Z. Shen, C. Chen, G. He, and C. Hao. Effect of Hydrogen Bonding on Self-Diffusion in Methanol/Water Liquid Mixtures : A Molecular Dynamics Simulation Study. *Journal of Molecular Liquids*, 203 :90–97, 2015.